
SIEMPRE AUTONOMA
POR MI PATRIA EDUCARE
UNIVERSIDAD AUTÓNOMA DE SAN LUIS POTOSÍ

Interferometry using magnetic sensitive states

Saeed Hamzeloui

April 2016

Contents

1 Introduction **1**

2 Magneto Optical Trap **4**
2.1 Introduction 4
2.2 Interaction between photons and atoms 4
2.3 MOT 5
2.4 MOT components 5
2.4.1 Laser sources 5
2.4.2 Saturation spectroscopy 7
2.4.3 Sats-spec modifications for the dual interferometer 8
2.4.4 Magnetic field environment 9
2.4.5 Vacuum chamber 11
2.5 Control system 11
2.6 Imaging system 11
2.7 Trapping results 13
2.8 Optical Molasses 13
2.9 Conclusion 13

3 Double MOT **15**
3.1 Introduction 15
3.2 Experimental setup 16
3.3 RF world 20
3.4 Optical modulation 26
3.5 Results of DIMOT 32

4 Preparations for atom interferometry **35**
4.1 Introduction 35
4.2 Rabi oscillations 35
4.3 Microwave setup 36
4.4 Results 37
4.4.1 Demonstration of π polarizations. 38
4.4.2 Zeeman pumping to a dark state 38
4.4.3 Demonstration of Rabi oscillations 40
4.5 Zeroing B 41
4.6 Improvement of fluorescence detection 43
4.7 Results of Ramsey method for the clock transition 45
4.8 Conclusion 47

5 Two Photon Transition **49**
5.1 Introduction 49
5.2 Preparation of two photon transition 49
5.2.1 RF antenna 49
5.2.2 Demonstration of the $|F = 1, m = 0\rangle \rightarrow |F = 2, m = 2\rangle$ transition 52
5.3 Coupling magnetic sensitive states $|F = 1, m = -1\rangle \rightarrow |m\rangle$ to $|F = 2, m = 1\rangle \rightarrow |p\rangle$ (desired transition) at low field 54
5.3.1 Two photon transition at high field 60
5.4 Conclusion 65

6 Dual Interferometer **66**
6.1 Introduction 66
6.2 Overview 66
6.3 Principles of Dual Interferometer 68
6.4 Experimental setup 70
6.5 Rabi oscillations in the transitions of interest 72
6.6 Dual interferometer 74
6.7 Conclusion 78

7 Conclusion and Outlook **79**
7.1 Conclusion 79
7.2 Outlook 79
7.2.1 Alternative method for the dual interferometer 79

APPENDICES **83**

A Articles **83**

B Derivation of Eqs (3.6) to (3.9) **84**

C Notations for the energy of levels in the rubidium atom **86**

List of Figures

1.1 Zeeman shifts for the ground state of ^{87}Rb in the presence of low magnetic field. The blue arrow (clock transition) is based on the magnetic insensitive states. The red lines show magnetically sensitive states are use in the interferometer. 3
1.2 The $|F = 1, m = -1\rangle$ to $|F = 2, m = +1\rangle$ transition at a field of B=3.228917(3)G, the system has minimum sensitivity to magnetic field fluctuations. Inset shows the zero slope (Figure is taken from [2]). 3

2.1 a) Schematic of MOT configuration. b) Energy levels and required transitions for the ^{87}Rb MOT. 6
2.2 The simplest model to explain the trapping in a MOT using two levels with $F = 0$ and $F = 1$. The Zeeman shifts of the sublevels in the B field gradient are shown, a dashed line denotes the laser frequency that is red detuned from the resonance. The atoms feels a net force that pushes them to the $Z = 0$. 6
2.3 Schematic for the sats-specs that are used for both lasers in the dual interferometer experiment (see the explanation in Section 2.4.2). 9
2.4 IGBT measured delay time for the complete turn-off. 10
2.5 The fluorescence of the atoms in the MOT taken by CCD camera and shown in LabView program. 14
2.6 Expansion of the atoms in the MOT in the $\hat{x}$ direction before (Green higher data points) and after applying the molasses (Red lower data points). The blue solid line is a linear fit. 14

3.1 Four lasers and required transitions in the traditional way to trap two isotopes ^{85}Rb and ^{87}Rb. 16
3.2 Experimental setup. The Solid red lines are the optical paths and the dashed blue lines are the RF parts [28]. 17

3.3 Spectrum of rubidium. The upper trace (dashed black line) shows the Doppler broadened spectrum of rubidium. The middle trace (solid black line) shows the excited state hyperfine transitions with the zero frequency corresponding to the leftmost transition. The lower trace (solid red line) shows the spectrum of laser light out of the fiber modulator. The tallest peak is the carrier and the rest are sidebands. The three left sidebands are tuned to the required transitions for the DIMOT. The laser is locked at the carrier position. The energy levels for the two isotopes are shown on the right [28]. 18
3.4 The second (red lines) and third order (blue lines) non-linearities made by RF_1, RF_2 and RF_3 signals (see Table 3.1). The taller red and blue lines are the closest (368 MHz) non-linearities to the resonances shown with the black lines. 1, 2 and 3 stands for RF_1, RF_2 and RF_3. 20
3.5 Oscillators. a)PLL synthesizer, model: EVALADF4350-EB2Z , b) VCO's from Minicircuits, models: ZX95-3360-S+, ZX95-5776-S+ and ZX95-6840C-S+ are connected to a voltage stabilizer circuit at the left hand of the picture. 22
3.6 Output frequencies of three available VCOs versus applied V_{tune} voltage. 22
3.7 The diagram of voltage stabilizer circuit for the VCOs. 23
3.8 Fast turn-off of the sidebands using RF switch. (a) Experimental setup to measure the turn-off time. (b) The result of the output signal of the mixer. 24
3.9 The diagram of the circuit used for amplifying the output current of the PI controller (TCM1000T) to stabilize temperature of VCOs. 25
3.10 Fiber modulator. a) schematic of fiber modulator, b) output intensity of modulator versus DC voltage, the red point shows the locking point of the intensity. 28
3.11 Fiber modulator characterization. It shows the first order sideband amplitude (red squares), second order sideband amplitude (green triangles), and visibility of the DC locking signal (blue diamonds). The solid lines correspond to the theoretical values. The fit is done to the first order sideband to obtain the three curves as indicated in the text. The second order sideband signal is buried in the noise for RF powers below 13 dBm [28]. 29
3.12 Optical spectrum after the tapered amplifier measured in a Fabry–Perot cavity. The tallest peaks indicate the carrier and free spectral range of the cavity (1.5 GHz). The peaks with ν_1=6589 MHz and ν_2= 5458 MHz correspond to the trapping frequencies, and the peak with ν_3=2545 MHz is the repumper frequency. The non-linearity and blue detuned sidebands are also visible [28]. . . 31
3.13 Atom number in the DIMOT. The sequence is ^{87}Rb only - ^{87}Rb and ^{85}Rb - ^{87}Rb only, with each stage lasting for 10 s; we turn the traps off at the end [28]. 33

4.1 A block diagram shows the microwave system used for microwave spectroscopy. 37
4.2 Microwave linear and circular polarization. 38

4.3 Microwave spectroscopy, the peaks correspond to the different transition. 39
4.4 Demonstration of π polarizations, the blue line shows spectroscopy with 9 transitions and the inverted red one only π polarized transitions. 39
4.5 π polarized light for Zeeman pumping. Here part of ^{87}Rb D_2 transition hyperfine structure is shown. An extra laser is used to send the atoms into the dark state. The $F = 1 \rightarrow F' = 1$ laser must be π polarized (red). 40
4.6 Demonstration of Zeeman pumping into the $|F = 1, m = 0\rangle$ dark state. The red (blue) trace is the result with (without) the pi polarized Zeeman pumping beam. 41
4.7 Demonstration of the Rabi oscillations for the clock transition. Blue points are experimental data and the red line correspond to the fit. 42
4.8 Monitoring box used for each coil to read the voltage (current) that goes directly in the $\hat{x}$, $\hat{y}$ and $\hat{z}$ coils. 42
4.9 The particular transition used to zero the field in each coordinate. 43
4.10 Results of the magnetometry using the atoms. Experimental data (red points) determines the zero for the B_x (a), B_y (b) and B_z (c). A blue solid line is a fit as explained in the text. 44
4.11 Microwave spectrum with a) only the trap fluorescence and b) with background suppression and correct normalization. 46
4.12 Demonstration of Ramsey interferometry for the clock transition, (a) with a $\pi/2$ pulse of duration τ=75 μs and a time between pulses of T =750 μs, (b) shows a zoom on the central part of the fringes to show the oscillations with τ=20 μs and T =9.96 ms. . 47

5.1 Two photon transition of $|F = 1, m = 0\rangle$ to $|F = 2, m = 2\rangle$ in ^{87}Rb. In presence of 385 mG the degeneracy is lifted. A MW and RF signals are used to drive the two photon transition. $\Delta = 50kHz$ is the detuning. 50
5.2 An image of the RF antenna. 51
5.3 Rabi oscillations of Zeeman sublevels in $F = 1$ using an RF antenna. The data points are joined by a black dashed line and the red solid curve is a fit. The fit gives 12 kHz Rabi frequency and the duration for a π pulse is 41 us. 52
5.4 Rabi oscillations for two photon transition of $|F = 1, m = 0\rangle$ to $|F = 2, m = +2\rangle$ with (a) Δ=24 kHz, (b) Δ=50 kHz and (c) Δ=100 kHz, the black points are experimental data and solid red curves are the fits which give the Rabi frequencies of $\Omega_{(a)}$=1920$\pm$70 Hz, $\Omega_{(b)}$=990$\pm$10 Hz and $\Omega_{(c)}$=420$\pm$25 Hz. 53
5.5 Two photon transition of magnetic sensitive states $|p\rangle$ to $|m\rangle$ in ^{87}Rb. In presence of 385 mG the degeneracy is lifted. Starting all atoms in $|l\rangle$, a π pulse sends all atoms to $|p\rangle$. The Ω_{MW} and Ω_{RF} drive the two photon. Δ is detuning. 54
5.6 A block diagram of MW and RF setup for coupling $|m\rangle \rightarrow |p\rangle$ transition. 55

5.7 Single and two photon transitions for a fixed RF frequency and modulating MW. The thick black line in the center shows the desired two photon $|m\rangle \longrightarrow |p\rangle$ transition. The center blue lines show the single photon transitions. The other groups are the two photon transitions $\nu_a = \nu_m + \nu_{RF}$ (red lines with $\Delta m = 1$) and $\nu_a = \nu_m - \nu_{RF}$ (green lines with $\Delta m = 1$). In these transitions, the difference for the m quantum number can be 2 which is shown by thin black lines. The plot has a zoom in the red square zone (inset) at the field of 2.95 G. 57
5.8 Spectrum taken with only the two photon fields on, $|p\rangle \longrightarrow |m\rangle$ transition (higher red trace) and $|l\rangle \longrightarrow |u\rangle$ transition (lower blue trace). The small peak in the lower blue trace comes from the residual population in the $|F = 1, m = -1\rangle$ level after optical pumping. 58
5.9 Frequencies of two photon transitions vs magnetic field. The black data points shows the measured frequency corresponding to the two photon $|p\rangle \longrightarrow |m\rangle$ transition in particular magnetic field. The red solid curve is the theory in Eq 5.2 for the desired two photon transition. The green and black dashed curves belong to the theory for the two photon of clock excitation and $|F = 1, m = 1\rangle \longrightarrow |F = 2, m = -1\rangle$ transition in Eqs 5.3 and 5.4 respectively. 59
5.10 Spectroscopy of two photon transitions around 3.2 G. Each color belongs to a particular magnetic field that are shown in the plot. ν_0 is the resonant frequency at 3.2 G. 59
5.11 Rabi oscillations of (a) the desired two photon transition and (b) the undesired two photon excitation of the clock transition due to presence of atoms in $|l\rangle$ level. The black points are experimental data and solid red curves are fits. The fits give the Rabi frequencies of 900±5 Hz and 785±5 Hz for (a) and (b) respectively. 61
5.12 (a) Image of the IGBT circuit. (b) Schematic of the circuit to rapidly switch between the low and high bias magnetic fields. Paths with high (low) TTL are in blue (red). 62
5.13 Bias magnetic field as a function of time measured with MW spectroscopy on the $|l\rangle$ to $|p\rangle$ transition. In red is an exponential fit to the asymptotic value. 63
5.14 MW spectroscopy for two photon transition $|F = 2, m = +1\rangle$ to $|F = 1, m = -1\rangle$ at 3.2 G. 63
5.15 Rabi oscillations for the two photon transition at 3.2 G field. Black Points are the experiment and red solid curve is a fit to Eq 4.3. 64
5.16 Interference fringes for the two photon transition at 3.2 G field. Black Points are the experiment and red solid curve is a fit to a sinusoidal function. 64

6.1 Microwave pulse sequence and microwave system. 71
6.2 (a) Rabi oscillation for clock transition. We get $\Omega_c/2\pi = 4.5$ kHz with a coherence time of 0.5 ms. (b) interference fringes for the clock transition at 3.2 G field. Experimental data points are shown in black and red curve is a fit of a sinusoidal function. . . 73

6.3 Part of the written program in LabView front panel for the dual interferometer project. The red rectangular box shows Ramsey $\pi/2$-Time Evolution-$\pi/2$ sequences. 74
6.4 Signal variation versus the normalized duration of preparation pulse (t/t_π) at 2.5 G. The solid red line is an absolute fit to the data. 75
6.5 Signal variation with magnetic field (ΔS) as a function of the fraction of atoms in the two photon transition (P) at 2.5 G. The solid red line is a fit to the data and the red dashed line gives the theoretical signal (Eq 6.7) for ΔB=1.2 mG. 75
6.6 Signal variation with magnetic field (ΔS) measured at $P = 1$ at different values of the magnetic field. 76
6.7 Fraction of atoms in each interferometer (P) required to have minimum sensitivity at a particular magnetic field (B_{min}). The red solid (blue dashed) line corresponds to Eq 6.11 with $V_r = 1(2)$. 77

7.1 Ramsey sequence for two photon transition using alternative method. (a) All the atoms are initialized at $|l\rangle$ sublevel. (b) A $\pi/2$ pulse resonant with $|l\rangle \leftrightarrow |u\rangle$ splits atomic cloud into a 50-50 % superposition. (c) The bursts of π pulses resonant with $|l\rangle \longrightarrow |p\rangle$ and $|u\rangle \longrightarrow |m\rangle$ starts the first $\pi/2$ in Ramsey sequence. 80
7.2 Block diagram for the microwave generating system of alternative method for doing interferometry on the two photon transition. . 81
7.3 Ramsey fringes of $|p\rangle$ to $|m\rangle$ using an alternative method. The width of the peaks is 60 Hz that corresponds to the time between pulses. The experiment is repeated twice shown with the black and gray curves. 82

List of Tables

2.1 Background contribution of each beam. 12

3.1 Undesired frequencies due to the non-linearities of EOM made by RF_1, RF_2 and RF_3 signals. 19

5.1 Resonant frequencies of RF antenna number 3. 50

Acknowledgements

Foremost, I would like to express my sincere gratitude to my adviser Prof. Eduardo Gomez for the continuous support of my research, for his patience, motivation, enthusiasm, and his knowledge in Physics. His guidance helped me in all the time of research and academic life. I will consider myself his permanent student and I know that I could always ask him for his advice and opinions on lab related issues.
I will forever be thankful to my wife Vahideh which was also my lab-mate during my PhD for her helps and accompanying me in all these four years.
All promised projects in this thesis fulfilled by a collaborative efforts and an environment based on the team work. My sincere thanks goes to my ex lab-mates Dr. Lorenzo Hernández and Dr. Víctor Valenzuela. I have learned a lot from them during their presence in the lab. Daniel Martínez had a great contribution in my thesis. During his master we spent a lot of times for ongoing project. He was more than a lab-mate and I am grateful to have his friendship. I also thank the friends in particular Nieves Arias, Eslava Del Rio, Francisco Salces, Monica Gutiérrez, Maricarmen Ruiz and Eduardo Uruñuela for their supportive roles.
I acknowledge the Ministry of Science and Technology (CONACyT) in Mexico to support my PhD work.
Last but not the least, I would like to thank my parents, my sister and brother for their spiritual support throughout my life.

Abstract

Atomic interferometry is a very sensitive technique in precision measurements. In this PhD work we explore ways to improve certain aspects of atomic interferometry. We show that there are some advantages on using magnetic sensitive states. We introduce the required infrastructures to implement Ramsey type interferometry on particular transitions. Using a Magneto Optical Trap (MOT) which is the main prerequisite, the atoms are trapped and cooled. The trapping procedure with the MOT requires ingredients such as lasers, the homogeneous and inhomogeneous magnetic fields, the chamber containing the sample, the vacuum system and the detection part (see Chapter 2). At the beginning of my PhD, this facility for trapping the rubidium atoms was available. Later on we upgraded the vacuum system. During this PhD work we could further cool down the trapped sample thanks to the optical molasses technique. We maintain the atoms at temperatures typically below some tenths of micro Kelvin. The coherent manipulation of the atoms is the significant part of this thesis since we aim to do atomic interferometry. Using radiations in microwave domain, it is feasible to couple any two states and do the Rabi oscillations between the hyperfine and Zeeman levels.

My first work as a PhD student was to contribute in the Dual Isotope MOT (DIMOT) experiment (see Chapter 3). The idea was to trap both isotopes of rubidium simultaneously by using only single laser and an Electro-Optical Modulator (EOM). This work introduces huge simplifications on the optical part and is extendable to trap more isotopes at the same time. The experiment has the optical and RF parts and my contribution was to complete the RF part.

Starting all the atoms at the particular initial point for the interferometry takes us some considerable time to be sure that we correctly transfer the atomic population into the desired state (see the discussion in Chapter 4). From that point we focused on two transitions to use the Ramsey type interferometer. Each of these two transitions have an optimum operating point in order to be far from the magnetic field fluctuations since the interferometers are quite sensitive to the field perturbations sensed from the environment. At the end we aim to combine these two transitions of interest to make a dual interferometer (see Chapter 6). The idea is to obtain the minimum magnetic sensitivity at a tunable magnetic field by changing the fraction of atoms in each interferometer. The dual interferometer may be useful in applications where low magnetic sensitivity is required at a particular magnetic field.

Chapter 1

Introduction

The long term goal in the Cold Atoms Laboratory located at San Luis Potosí, Mexico is to measure the gravitational acceleration with high precision. Atomic interferometers are ideal tools since they are very sensitive and have applications for instance in metrology [1]. Thanks to the laser cooling techniques, atomic interferometers have been improved and neutral alkali atoms can be cooled to a few micro-Kelvin in a Magneto Optical Trap (MOT). The reason to have such a cold gas is to have a precise control on the position and the velocity of the sample. In these interferometers, the atoms are split by the resonant laser pulses and move along separated paths. The atomic sample are then recombined to form an interference pattern. The atoms acquire a phase difference during the time between the splitting and recombination process. This phase is sensitive to the quantity of the interest g. The discussed atomic interferometers have some analogues in optics (Mach-Zehnder Interferometer). The transition used for these interferometers is called Raman transition which is not related to this PhD work. In this work Ramsey type interferometry has been realized using microwave pulses. Due to their large wavelength, they do not have enough momentum kick to do gravimetry. In general, the interferometers need to deal with the magnetic fields and their fluctuations. These fields may be problematic since most of the transitions are sensitive to the field fluctuations. Therefore the goal in this thesis is to study the response of the atoms to magnetic fluctuations in our developed interferometer.

In Chapter 2 we discuss about the requirements for capturing the atoms in a MOT. We give the details about the lasers, vacuum, control and imaging systems. For interferometers, extra cooling might be necessary. The last section in that chapter describes the method for further cooling the atoms using Optical Molasses (OM). The last technological and instrumental upgrades during this PhD work are inserted in each section. Chapter 3 has a discussion on a simultaneous trap for two rubidium isotopes. The idea was to capture both isotopes of rubidium (^{85}Rb and ^{87}Rb) simultaneously in the MOT. Traditionally one needs four laser system in order to have the trap and repumper transitions for trapping two isotopes. This chapter demonstrates a considerable simplification in the experimental setup by using an Electro-Optical Modulator (EOM). This reduces the number of laser to one and the other three required frequencies are obtained with the modulator by feeding in the correct RF frequencies. Once the atoms are captured in the MOT and OM is applied to them, they

go through different steps such as optical and Zeeman pumping to be initialized in particular Zeeman sublevel. We review the needed infrastructures for these initialization steps in Chapter 4. Also we show our last updates on our detection system which enhance the quality of the signal for the Ramsey type interferometers. Now we are able to study the magnetic field and its fluctuation effects on our interferometry. Figure 1.1 shows an schematic representation of the energy shifts in ^{87}Rb in the presence of low magnetic field. To have minimum magnetic sensitivity, the two levels involved in the transition must have the same magnetic response (the blue lines in Fig 1.1). This is the case for the hyperfine clock transition between $|F = 1, m = 0\rangle$ and $|F = 2, m = 0\rangle$ at zero field. Bosonic alkali atoms have another magnetic insensitive transition at low magnetic field between $|F = 1, m = -1\rangle$ and $|F = 2, m = 1\rangle$. The linear Zeeman shift is the same for both levels and cancels, leaving only the quadratic Zeeman effect around a particular magnetic field value (the red lines in Fig 1.1). The minimum sensitivity for this two photon transitions is achieved at 3.2 Gauss for the case of rubidium [2]. This transition has been used by many groups for different reasons [3, 4, 5, 6, 7, 8]. The two states of this transition have essentially identical magnetic moments and hence feel identical confining potentials. In chapter 5 we discuss about two photon transition coupling since it is not possible to drive this transition with a single photon transition due to the selection rule.
People know the operating points for the magnetic field in order to have minimum magnetic sensitivity (e. g. inset in Fig 1.2) in their interferometry. We mix two interferometers based on clock and the above two photon transitions. Chapter 6 demonstrates a dual interferometer that has minimum magnetic sensitivity at a tunable point between 0 and 3.2 Gauss. The point of minimum sensitivity depends on the fraction of atoms in each interferometer. Chapter 7 shows the conclusions and introduce an alternative method as a prospective goal in the lab for doing interferometry in the two photon transition. This strategy uses only single photon transitions.

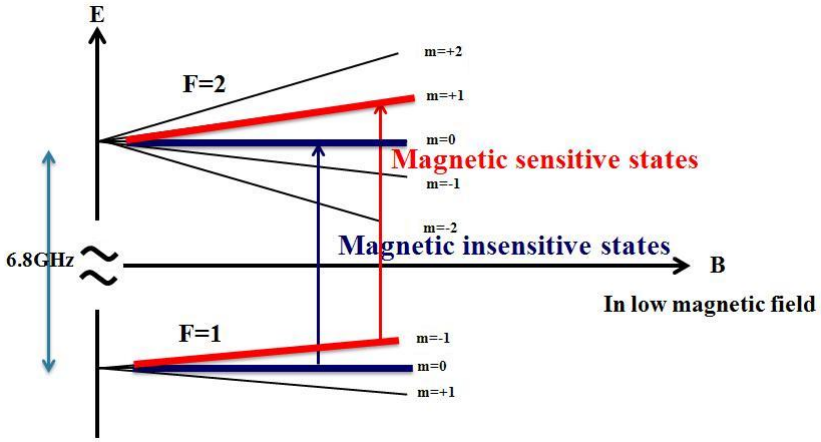

Figure 1.1: Zeeman shifts for the ground state of ^{87}Rb in the presence of low magnetic field. The blue arrow (clock transition) is based on the magnetic insensitive states. The red lines show magnetically sensitive states are use in the interferometer.

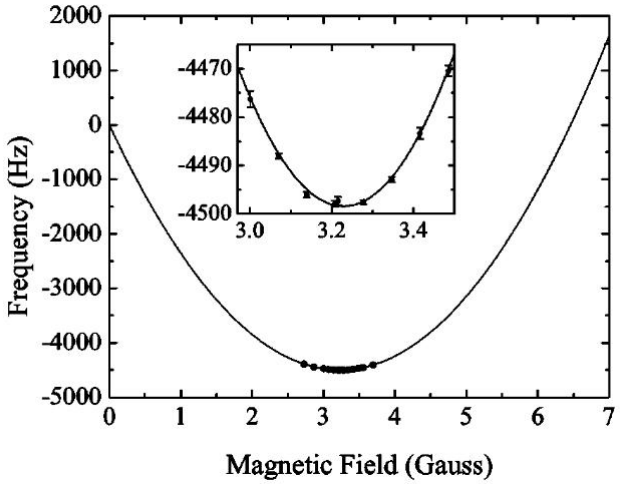

Figure 1.2: The $|F = 1, m = -1\rangle$ to $|F = 2, m = +1\rangle$ transition at a field of B=3.228917(3)G, the system has minimum sensitivity to magnetic field fluctuations. Inset shows the zero slope (Figure is taken from [2]).

Chapter 2

Magneto Optical Trap

2.1 Introduction

In this chapter, we describe the configuration of the Magneto Optical Trap (MOT) in our cold atoms laboratory. In the beginning of the lab, two previous doctoral students Lorenzo Hernández (2011) and Víctor Valenzuela (2012) developed the first MOT in our laboratory [9, 10]. A MOT requires resonant laser beams plus a gradient of magnetic field where all of the experimental sequence is directed by the control system. Imaging system for the detection of atoms works either with a CCD camera or a photo-diode connected to a NI USB-6289 card. We use the LabView software for all the programs. A MOT uses laser cooling in order to achieve the cold, trapped, neutral samples with temperatures as low as several micro-Kelvin. Such a cold sample allows for low kinetic energies, long interaction times and reasonable density which are useful for the precise experiments in the field of, for example, quantum optics, frequency standards, cold collisions or atom optics [11].

2.2 Interaction between photons and atoms

In our case we are interested to trap ^{87}Rb atoms. The reason why people choose rubidium for the cooling and trapping is that they do not need expensive lasers due to the required 780 nm wavelength used for its atomic structure [12, 13]. When a photon hits an atom, due to the momentum conservation, the atom absorbs the momentum of the photon. The recoil due to the velocity change of the atom is given by $\mathrm{v}_{rec} = \hbar\mathrm{k}/\mathrm{M}$. Then the excited atom in a higher energy level decays through the spontaneous emission. The decay time $\tau = 1/\gamma$ is the inverse of the natural linewidth of the excited state. Since the spontaneous emissions have the recoils of the atoms in random directions, there is no net momentum transfer on average. The force of a laser, $\vec{F}$ depends on the scattering or excitation rate of photons Γ_{SC} [14]:

$$\vec{F} = \hbar\vec{k}\Gamma_{SC}, \tag{2.1}$$

with

$$\Gamma_{SC} = \frac{\gamma S/2}{1 + S + [2(\delta + \omega_D)]^2}, \tag{2.2}$$

where S = I/I_S the saturation parameter, I the light intensity, I_S= πhc$\gamma/3\lambda^3$ the saturation intensity of the transition; ω_D=-$\vec{k}$ $\vec{v}$ the Doppler shift and δ=(ω_L-ω_0) the detuning.

2.3 MOT

It is necessary to understand the hyperfine structure of the sample we want to trap. Figure 2.1a displays the counterpropagating laser beams in three dimensions with the circular polarizations σ^+ and σ^-. For the retro-reflected beams we used dielectric mirrors of 5.cm diameter plus 6 quarter wave plates ($\lambda/4$) to generate the circular polarizations. Figure 2.1b shows lasers which keep the atoms inside the cyclic transition. ^{87}Rb, for example, has a cyclic transition between the $5S_{1/2}$F=2 state and the $5P_{3/2}$F=3 state. When the atom is in the excited state, it cannot decay to any of the $5P_{1/2}$ states because of the parity conservation selection rule, and is also forbidden from decaying to the $5S_{1/2}$F=1 state because of the angular momentum change is -2. The trap laser excites the cycling transition and there should be another laser to repump the atoms that decay to the lower ground state, that's why it's called the repumper laser. A gradient of the magnetic field is required to trap the atoms. Figure 2.2 shows how the trapping of atoms work. Atoms feel a net force which is dependent on their position. For instance, when the atoms moves toward the right side of the figure, the force applied by the σ^- light is much stronger than the force of σ^+ due to its low detuning. This makes the force restorative to the center of trap $Z = 0$. In the trap, a dissipative force makes the cooling process worked. To conserve the energy of the photon scattered by detuned lasers, the kinetic energy of atoms pays the price and therefore a damping force which depends on the velocity of the atoms pushes them to slow down and does the cooling part.

2.4 MOT components

2.4.1 Laser sources

The lasers for a MOT must be stable and capable of giving high intensity (requiring no more than the saturation intensity). The linewidth must be smaller than the natural linewidth. Because of their low cost, compact size and ease of use, diode lasers are the choice for many of the MOT species. The linewidth and stability of these lasers is controlled using servo systems. We stabilize the lasers to an atomic reference. In our case we use a diode laser (Sharp GH0781JA2C) for the cooling (trap) and repumping beams. The diode is connected to a temperature controlled mount from Thorlabs (model: LDM21) that allows to control its temperature. The mount is connected to a TEC (Thermal Electric Cooler TCM1000T) to control the temperature and set the wavelength around 780 nm with the TEC and the current in the source. A homemade low noise current source is used to provide the current into the diode. We put an optical isolator (CONOPTICS, model: 716) in front of each laser to prevent any probable damage to the diode via fluky reflections. Furthermore, our laser system in contrast

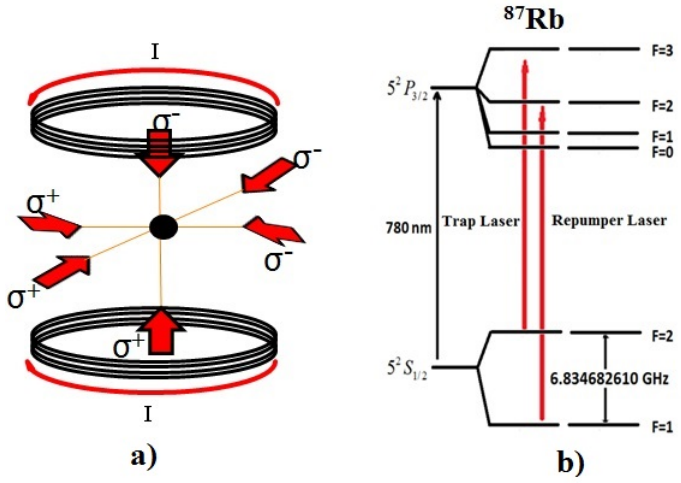

Figure 2.1: a) Schematic of MOT configuration. b) Energy levels and required transitions for the ^{87}Rb MOT.

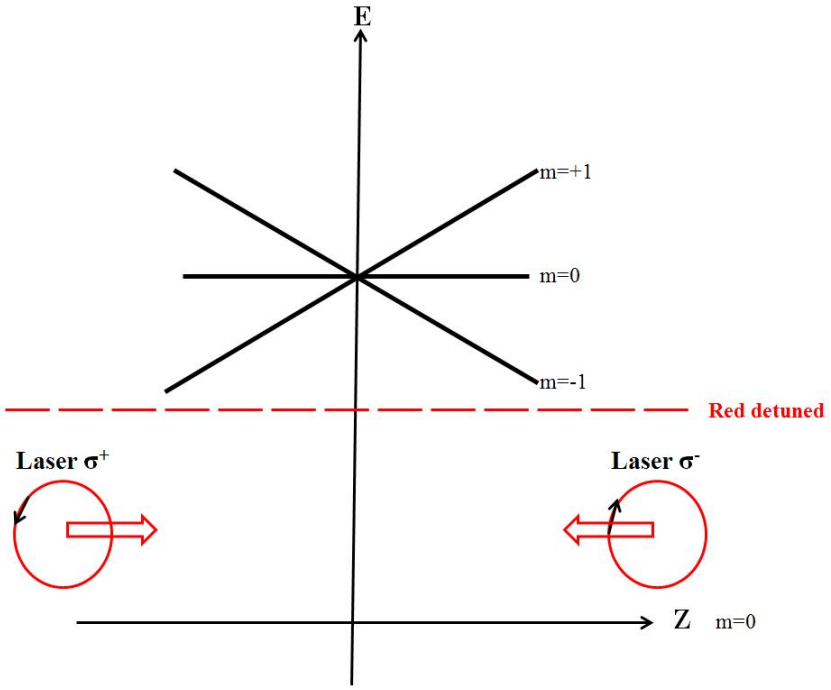

Figure 2.2: The simplest model to explain the trapping in a MOT using two levels with $F = 0$ and $F = 1$. The Zeeman shifts of the sublevels in the B field gradient are shown, a dashed line denotes the laser frequency that is red detuned from the resonance. The atoms feels a net force that pushes them to the $Z = 0$.

to the commercial ones (for instance, Sacher Lasertechnik Group, Model: TEC 120 which we already used it for the repumper path) is much less sensitive to the vibrations because it does not have grating. The maximum power at the output of the diode is 120 mW with 1.3 MHz linewidth. The daily experience proved us that the temperature controller of the repumper laser is much happier than the trap one provided that the air conditioning must be on all the times to stabilize the diode temperature. The frequency of both lasers must be adjusted around 12816.5 cm^{-1} reading in the wave-meter by changing the temperature (T_{set} screw) in the TEC and the diode current. Once I turn on the laser source, first I crank the current up to 95 mA reading with a multimeter while the screen of TEC already is set to be 17. The procedure is to increase T_{set} by the steps of maximum 0.3 and compensate the seen jumping hops to reach 12814-15cm^{-1}. When we read those mentioned range, we must change T_{set} by the steps of 0.1 patiently and follow the same process to reach the desired value with the fluctuations less than 0.1cm^{-1}. We ought to be careful do not pass 130 mA for the lasers. We observed that the frequency stabilization procedure is in ideal form when we achieve the maximum current (130 mA) and temperature screen displays 20±2. The easy part of the stabilization for the repumper laser is that we only see one jumping hop during the process while in the trapping laser might see couples of them.

2.4.2 Saturation spectroscopy

Saturation spectroscopy is a technique to resolve the excited state hyperfine structure and it is used to lock lasers to a narrow reference [15]. A tunable laser beam is absorbed in the atomic vapor when it is on resonance. If one shines a beam into a Rb cell and monitors the transmitted light as a function of frequency, a Doppler broadened absorption spectrum will be observed which has a width of around 500 MHz. Adding a saturating beam in the opposite direction, one observes Doppler free absorption because only atoms with zero velocity can interact with both beams simultaneously, the atoms with some velocity will have a Doppler shift that is opposite for both beams. In addition to the main peaks we are able to see extra peaks correspond to the crossovers. This happens when the laser frequency is in the middle of two main peaks and only the atoms with particular velocities are resonant.

We lock the trap laser using Hyperfine Dichroic Atomic Vapor Laser Lock (HDAVLL) technique [16]. Part of the linearly polarized light goes through a Rb cell by reflecting from a double glazing glass at the entrance of the cell (Model: GC25075-RB, Thorlabs). We block one of the reflected beams by an iris. The linearly polarized light can be considered as the sum of a σ^+ and σ^- polarizations. The Zeeman effect shifts σ^+ a little bit to the right and the σ^- to the left. This light passes through a quarter wave plate with the proper angle and a beam splitter cube to convert into two horizontal and vertical linear polarized lights. Two detectors receive signals with different linear polarizations and subtract electronically the two. The consequence is generation of the error signal. We use only couples of hundred μWatts for locking.
We were using a commercial laser source for the repumper laser before (Sacher Lasertechnik Group, Model: TEC 120). We found that the laser had line noise due to a ground loop. We replaced that laser with a home made laser similar to the trap one. In the new method for locking the repumper laser, we use the

sat-spec technique. The light reflects from a similar double glazing glass into the cell. In contrast to the hyperfine DAVLL technique used for the trap laser, we let both beams enter the cell. One of them directly is sent to the detector, the other beam is overlapped with the transmitted part (from the glass) counter-propagates through the cell and is sent to the second detector (see Fig 2.3). Since we had a lock-in amplifier (410 Single Phase Lock-in Amplifier, Scitec Instruments Ltd) around, we decided to use it. The signal coming out from lock-in amplifier improved a lot. The reason why we use it for the repumper and not trap is that requiring 50 kHz dithering which is not ideal for the trap laser. Additionally, we use a commercial photo-receiver (New Focus, Model: 2307) instead of homemade one for the repumper. The important advantage of this detector that is capable to work with the battery and this is good to be far from the line noise. Having said that, the locking systems for the trap and repumper works reasonably acceptable. For instance, we do not need to change the Gain or P-I controller knobs in the feedback systems. The trap survives at least for 30 minutes.

We lock the trap laser to the crossover of F'=2 and F'=3. Then we send the beam through an acoustic optical modulator (AOM Isomet, model: 1206C) which the first order diffraction in double pass takes us to the blue detuned from F'=3 (104 MHz). This signal is sent to a fiber which ends to the input of a tapered optical amplifier (Eagleyard EYP-TPA-07800-01000). The input power to the amplifier must not exceed 1.5 mW. A feed-forward circuit is designed to generate a signal dependent on the FM frequency in the AOM. In this circuit, we can adjust four parameters (a, b, c, V_0, V_1) using potentiometers to maintain constant signal at the output of diffracted path of AOM. This circuit must be readjust at least each two months. Optimally we ramp the current into the amplifier first in single pass and we check the power of the light in 1, 2 and finally 3Amps. The maximum current in the amplifier is 3 Amps corresponds to maximum 5 V for the temperature controller of that. The amplified light has a lobe shape which we decided to block it and thus we have 500 mW immediately after the double pass in the amplifier. This light is focused and sent to a single pass AOM (Isomet, model: 1206C) and we use its -1 diffraction order to be red detuned in the trap laser by 18 MHz. Since the second AOM is placed after the amplifier, it enables us to switch the trap laser on and off without any threat to the amplifier.

2.4.3 Sats-spec modifications for the dual interferometer

In the previous Section that was the sats-spec description for the DIMOT experiment (Chapter 3), we do not need to lock the repumper laser but for the future dual interferometer experiment; we pursue to have the locking system for both trap and repumper lasers. Therefore we decided to use the sats-spec using Lock-in amplifier method [17] for both lasers in the dual interferometer experiment. This experiment will be discussed in Chapter 6. We found that the sats-spec method with the Lock-in amplifier has more stability compared to the HDVALL technique. The Lock-in amplifiers that we used for the trap and repumper lasers are 410 Single Phase Lock-in Amplifier, Scitec Instruments Ltd and 5204 Lock-in Analyzer, Princeton Applied Research respectively. Figure 2.3 shows the schematic for the sats-specs that are used for both lasers in the dual interferometer experiment.

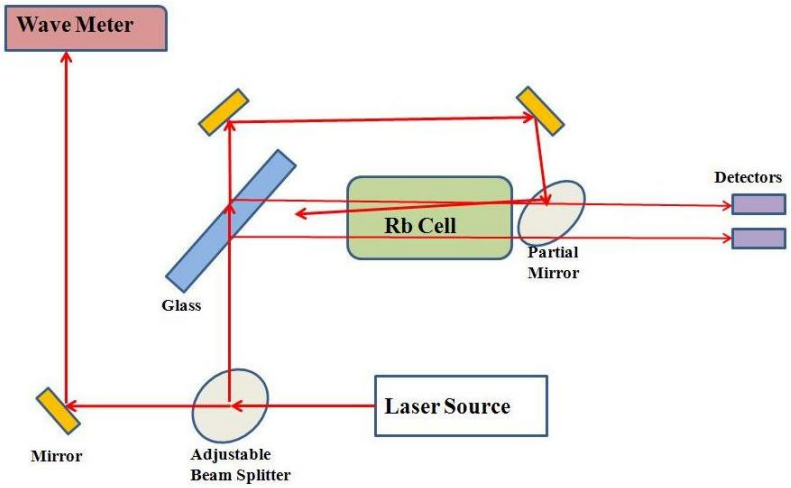

Figure 2.3: Schematic for the sats-specs that are used for both lasers in the dual interferometer experiment (see the explanation in Section 2.4.2).

For the dual interferometer experiment we introduced the $|F = 1\rangle$ to $|F' = 1\rangle$ transition for repumping. First we lock the repumper laser to the crossover of $F' = 1$ and $F' = 2$. Then we send the beam through an acoustic optical modulator (AOM Isomet, model: 205C-1) which the minus first order diffraction in single pass takes us to $F' = 1$ (80 MHz). We installed a mechanical shutter on this path to kill the scattering light made by this laser. We also needed to have the repumper locking scheme based on mentioned transition because we wanted to use an extra laser on the same transition with π polarization for the Zeeman pumping (see Section 4.4.2).

2.4.4 Magnetic field environment

In order to produce the MOT, we need a gradient of magnetic field as described in Section 2.3. We use two small coils with anti Helmholtz configurations and 25 turns to produce the magnetic field gradient in the center of the cell [18]. Each of them has a 2.77 cm radius and a separation of 4.8 cm. The gradient is capable to be varied from 5 G/cm to 15 G/cm. The atoms are trapped at the zero of the magnetic field gradient. Under the influence of the magnetic field the degeneracy is shifted (Zeeman effect) and each hyperfine state F splits in 2F + 1 sublevels. The Zeeman shift of the sublevels is proportional to its magnetic quantum number m_F and to the B field:

$$\Delta E_{m_F} = g_F \mu_B B m_F, (m_F = 0, \pm 1, ..., \pm F), \tag{2.3}$$

where: g_F=1/2 is Landé factor for the ^{87}Rb, μ_B is Bohr magneton and B is magnitude of the magnetic field.
At some point for example, during cooling the atoms, we need to turn off the magnetic field gradient abruptly. An insulated-gate bipolar transistor (IGBT) circuit is designed for that purpose. It has a switching between the current flows into the inductors (coils) and a dummy load. The resistor in the dummy

load must be the same as the inductance of the coils to make no difference in switching for the power supply. The microwave spectroscopy for a particular transition has done once we change the delay time of IGBT turn-off (for further information about microwave spectroscopy see Section 4.5). In different time delays, the position of the peak shifts in the spectrum which translates to a magnetic field. Figure 2.3 shows the result, at least 1ms time delay is needed for the complete turn-off.

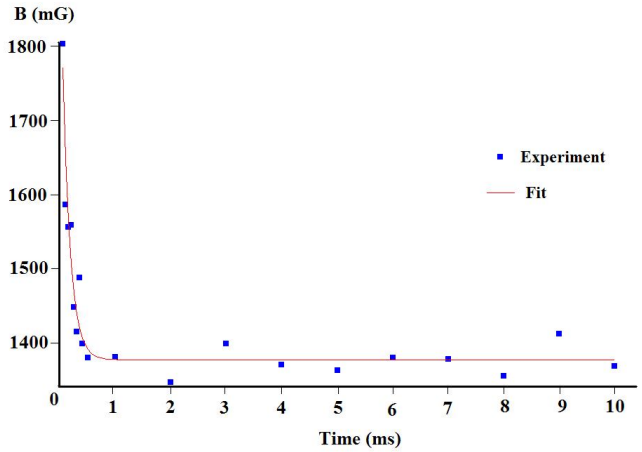

Figure 2.4: IGBT measured delay time for the complete turn-off.

We also use extra pairs of coils in the $\hat{x}$, $\hat{y}$ and $\hat{z}$ dimensions with a square shape to displace zero of the magnetic field and to add any desired constant field. Each coil has N=50 turns with the side of 30 cm which form a cube with the same side. (For more details see Section 4.5). We want to be far from the magnetic field noise as much as possible, in that direction we found a big fraction of the noises are due to of the power supplies nearby. We verified that the noise decays as $1/r^2$ as we move away from the supply. We sent all the supplies 6m away from the experiment side where they give contributions below 10 μG.
We also cleaned the optical table from any magnetic or steel materials. All the posts with the magnetic bases replaced by the non-magnetic ones.

Rubidium cell in the sat-spec of trap laser (HDAVLL) is wrapped with the wires to inject the current. We never turn off the power supply (DRP303C) to have stable current. The supply reads 0.8 A and with this amount of current, sat-spec signal looks good.

We aim to interpolate the magnetic field in the distances close to the center of the cell where we trap the atoms. Using the magneto resistance sensor (Honeywell HMC1002), a measurement has done to get the gradient of the field at the center of the cell. The cell was evacuated from its position but it was still close to the measurement area. We observed a gradient of 12 mG/cm, 30 mG/cm and 19 mG/cm in X, Y and Z directions respectively.

2.4.5 Vacuum chamber

The MOT is loaded from a background of thermal vapor and forms in a ultra-high vacuum chamber to have the atoms with long enough lifetimes. We already replaced the trapping cell from a stainless steel chamber to a Pyrex one to avoid eddy currents that existed in the former one, due to the copper ring gaskets. We did that also because of the measurements with the microwaves and the Raman beams since it gives a better optical access. To construct the new cell, a complete new vacuum system was considered [18]. The proper type of a pump depends on the quality of the required vacuum. In our case, a pressure of about 10^{-10} Torr is needed. We changed the old pump with the new one. The new pump is NEXTorr (D100-5) from SAES Getters. It consists of a Non Evaporable Getter (NEG) and an ion pump which combines a 100 l/s getter pump and a 5 l/s ion pump. This pump gives a high pumping speed and it is vibration free with a compact size. According to the datasheet of the company, the pump introduces magnetic field gradients smaller than 20 mG/cm at the position of the atoms. The NEG one acts as the main pump for the active gases and the ion pump removes the noble gases and methane which are not pumped by the NEG [19].

2.5 Control system

All the experimental apparatus is controlled by a laboratory control system. The control system consists of a set of digital outputs (DiO card) and analog (DAC card) that are synchronized by a 32 digital 2 MHz outputs card (NI PCI-6533, National Instruments) [20]. The 32 digital outputs of NI PCI6533 use 16 outputs for data, 8 outputs for steering and 1 output for strobe. All outputs are sent to a card called buffer which is in charge of restoring signals to prevent a voltage drop on the way to DiO and DAC and also to generate a suitable strobe pulse. The strobe pulse is responsible for updating data and address on both cards (DiO and DAC). The hardware is controlled by a LabVIEW software. We increased number of analogue channels to 16 as same as digital ones. In contrast to analogue, digital channels can be varied simultaneously.

2.6 Imaging system

Generally, to observe the atoms in real time in the MOT by a CCD camera there are two main techniques to detect them. When a laser near the atomic resonance propagates through confined atoms in the MOT, it will be absorbed and re-emitted. By detecting the scattered photons, one can image the cloud (fluorescence imaging). The other technique is to shine a resonant light to the sample and make an image of the shadow created by the atomic absorption with a CCD camera (absorption imaging). In both optical arrangement it is required to collect the light, collimate and focus on a CCD camera. The camera converts photons into photo electrons, and generates number of counts for each pixel of the chip that are proportional to the photons received and then also to the number of trapped atoms.

In the new designed imaging system [18], the fluorescence travels into a double relay configuration ($f-2f-f$) which all required optics are placed in a

Description of each beam	**Percentage**
Retro-reflected horizontal beam	9.36 %
Incident horizontal beam	5.9 %
Diagonal retro-reflected beam (toward the CCD)	58.14 %
Diagonal incident beam (toward the CCD)	0.66 %
Diagonal retro-reflected beam	22.38 %
Diagonal incident beam	3.56 %
Sum	100 %

Table 2.1: Background contribution of each beam.

tube (Thorlab cage system with 3 cm side). At the first relay, two biconvex lens (Model: LBF254-040-B, Thorlabs) with the Best Form type (to minimize the lens aberrations) are embedded to collimate and focus the light into the iris. The focal lengths and the diameters are f=40 mm and d=1 inch respectively. The iris is moveable and helps on the reduction of the background light. The second relay is placed after the iris and a 50-50 non-polarized beam splitter sits in the collimated part of the second relay, 8 cm separation was considered between these input and output lenses. It sends half of the fluorescence into a photo diode (PDA36A Thorlabs). That's an alternative to read the atom number. The photo diode has adjustable gain and we send the reading voltage to the National Instruments card (NI-USB 6289). This card has 32 inputs (analogue and digital) and 18 bits to save data. A LabVIEW code is used to process the signal of the camera and the photodiode. Furthermore, a small 0.5 inch metallic mirror is inserted at the entrance of the glass cell which is in the line of CCD camera and allows us to obtain absorption images in the future. The important parameters for the new imaging system are the following: the resolution is R=1.5 μm, the collection efficiency CE=0.0234 % and the amplification factor A=1.007±0.008. We could see an improvement compared with the old imaging system [10]. The resolution improved more than a factor of two, the collection efficiency is increased by a factor greater than 5 and the amplification factor is the same as before.

We have measured the background contributions for each beam (the trap and repumper lasers) into the camera by watching the intensity of a particular pixel monitoring in the Igor software. We found the noisiest path belongs to a retro-reflection of the diagonal beam (trap laser) which travels toward the imaging system with 58 % contribution and the minimum noise goes to the other input diagonal beam (trap laser) with 0.66 % contribution in the noise. Table 2.1 shows the contribution of each beam producing the background.

On the image analysis side, we improve the Igor Pro 2D fit program once the image data is sent from the LabView to it. It can measure the width expansion of the cloud only for two directions using a following 2D fit written in the program

$$f(x,y) = A \exp \frac{-1}{2(1-cor^2)}[\frac{(x-x_0)^2}{(\delta_x)^2} + \frac{(y-y_0)^2}{(\delta_y)^2}] - \frac{2cor(x-x_0)(y-y_0)}{\delta_x \delta_y}, \tag{2.4}$$

where A is the amplitude and the cor ($-1 \prec cor \prec +1$) is a coefficient determines cross correlation term between x and y, δ_x and δ_y are widths for the x and y directions.

2.7 Trapping results

We capture a big number of ^{87}Rb atoms N=5×10^9±5×10^8, with a size of 1.4 mm with a lifetime of τ=6±3 s and a density of n=10^{10} atoms/cm^3. The temperature of the thermal cloud is measured before and after the optical molasses. We get 38±5 μK and 2.73±0.22 μK respectively.

2.8 Optical Molasses

The Optical Molasses (OM) is a technique that can cool down the atoms to the temperatures colder than a MOT. First Steven Chu [61] reported it in 1985. There is a comparison of the OM versus the MOT:

- Both use 3 pairs of the circularly polarized counterpropagating laser beams.
- In a MOT, there should be the magnetic field that acts on the atoms but there is no magnetic field in an OM.
- The OM breaks the theoretical limit on the lowest possible temperature known as the Doppler limit $T_d = \hbar\Gamma/2K_B$, where Γ is the natural linewidth of the atomic transition, $\hbar$ is Planck's constant and K$_B$ is the Boltzmann's constant. The Doppler limit for the rubidium is 143 μK.

Usually an atomic interferometer needs the OM. We need to cool down the atoms otherwise the cloud may expand too much and it will not fit in our imaging system. In absence of the OM, an estimation for the 30 ms expansion of the atoms in the free fall gives 5 mm and once we apply the molasses we reduce the expansion to 1.3 mm. To do OM, we eliminate the gradient of the $\vec{B}$ by turning the IGBT off in the control system, then increasing the detuning of the trap laser by 66 MHz and finally decreasing the intensities of the trap and repumper lasers 5 and 1.5 times less respectively. All these steps are done in 6 ms. Figure 2.5 shows the fluorescence of the atoms in the MOT. To verify the temperature of the atoms, we let them expand with the time (time of the flight). We change the duration of the expansion from 0.5-20 ms and take an image in the trigger mode of the CCD camera. It is straightforward to measure the temperature which is $T = \frac{mV_{rms}^2}{K_B}$. The CCD camera sends the image data to the LabView program which is interfaced to the Igor Pro. It can measure the expansion of the widths for the cloud only for x and y directions using a mentioned 2D fit in the Section 2.6. Figure 2.6 shows the width of the cloud in the x direction versus the expansion time. A linear fit helps us to measure the slope which is the root mean square speed. We report the temperatures of the atomic cloud before 38±5 μK and after 2.7±0.2 μK the molasses respectively.

2.9 Conclusion

In this chapter we described the procedure for trapping the atoms using MOT. It is the main infrastructure for the prospective experiments in our laboratory. The required components such as lasers, magnetic fields, vacuum, controlling and imaging systems are discussed. Finally our trapping results are demonstrated. Last section explains the method for the further cooling of atoms using the optical molasses.

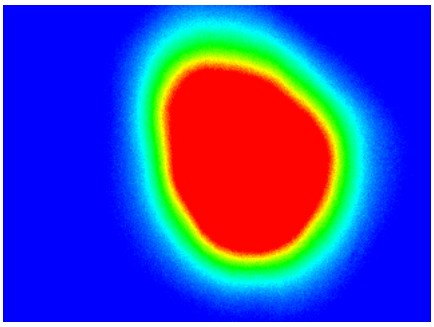

Figure 2.5: The fluorescence of the atoms in the MOT taken by CCD camera and shown in LabView program.

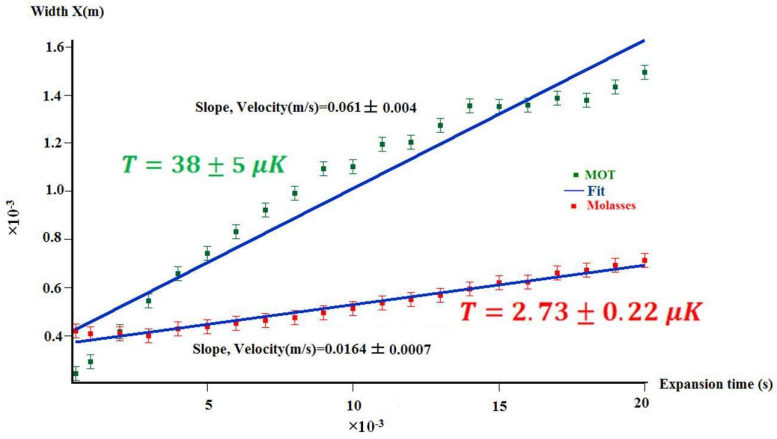

Figure 2.6: Expansion of the atoms in the MOT in the $\hat{x}$ direction before (Green higher data points) and after applying the molasses (Red lower data points). The blue solid line is a linear fit.

Chapter 3

Double MOT

3.1 Introduction

Simultaneous trapping of different isotopes or even species is useful for study of the quantum behavior of mixtures of bosons and fermions [21, 22] multiple-species photo association [23, 24], Feshbach resonances between different atoms [25], or sympathetic cooling [26], or in comparing properties of different atoms [27]. In our case we are interested to trap both isotopes of rubidium ^{85}Rb and ^{87}Rb simultaneously. Traditionally, we need to have four lasers to trap two isotopes (see Fig 3.1), for an instance the ones from rubidium. It requires many optics on the table and individual saturation spectroscopy for each laser, aligning different optical paths and acousto-optical modulators on each path to control the amplitude and frequency, etc.

This chapter is based on a published work [28]. We present a system capable of producing a multiple isotope MOT using a single diode laser. The system uses a fiber intensity modulator to generate sidebands at the required optical frequencies. We also used a tapered amplifier to boost the power. The system may also be useful in situations where multiple beams are necessary, e.g., for trapping atoms with electronic structure more complicated than alkali atoms [29], for laser cooling of molecules [30], and for the generation of many frequencies for white-light cooling [31].

Dual isotope MOTs (DIMOTs) have been demonstrated for Rb [22, 24, 26, 27, 31, 32, 33, 34, 35], K [36, 37], Yb [38], He [39], Li [40, 41], Sr [42, 43], and Cr [44]. For some elements, the isotope shift is small enough that the frequency difference can be covered with acousto-optic modulators (AOMs) [21, 36, 37, 38, 42]. As mentioned above, for atoms with a larger isotope shift, four independent lasers are often used, two for trapping and two for repumping [21, 41]. Each laser beam needs to be frequency locked and requires its own AOM to control the frequency and power. A trick to reduce the number of lasers is to add light modulation to produce sidebands and use them for the extra optical frequencies needed. One implementation uses current modulation in a slave laser to derive both the trap and the repumper out of it [45]. The sideband plays the role of the repumper due to the low power available. Electro-Optical Modulators (EOMs) are another common implementation [34, 35, 46]. The EOMs are simpler to use than the current modulation, and they give good modulation efficiency at high

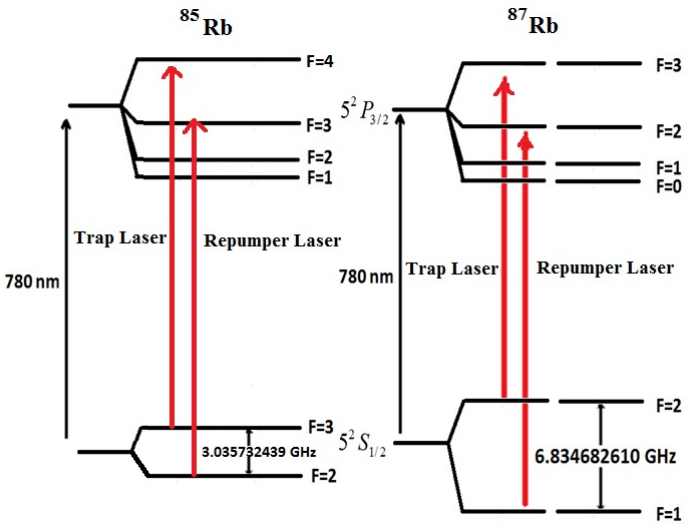

Figure 3.1: Four lasers and required transitions in the traditional way to trap two isotopes ^{85}Rb and ^{87}Rb.

RF frequencies, but they are usually resonant devices that only work around certain frequency. Fiber modulators have all the benefits of an EOM and a very large bandwidth (10 GHz). Their only problem is that they can only handle low optical power and an optical amplifier is needed to boost the power. Now we have a phase modulator (ADVR, model: WPM-P78P78AL0) that handles much more power (250 mW).

The system we present combines the very large bandwidth of a fiber modulator with the high optical power of a tapered amplifier. The use of a double-pass configuration for the tapered amplifier was essential in going from 0.5 mW out of the fiber modulator to 1 W. The power is high enough that the sideband can now be used as the trapping beam and not only as the repumper as before. Due to the large bandwidth, we include different RF frequencies using the same device to obtain the DIMOT. The tuning range for any beam is two orders of magnitude larger than what can be achieved using AOMs, and it is big enough (for a 40 GHz modulator) to cover even the He isotopic shift [39]. The independent control of all the beams is now on the RF side. There is no need to add extra AOMs to control the frequency and power of each beam except the repumper of ^{87}Rb. The reason is that we use it as the carrier and the rests are the sidebands. All the beams propagate in the same direction, and it is not necessary to spatially overlap them as would be the case when using AOMs. A similar idea has been used to obtain the repumper light in a single isotope trap [47].

3.2 Experimental setup

The experimental setup is shown in Fig 3.2. A Diode laser is the only light source which is locked to a saturation spectroscopy reference using the hyperfine

DAVLL technique as described in the Section 2.4.2. Then we send the laser light into a fiber intensity modulator (EOSPACE AZ-0K5-10-PFU-SFU-780) that generates multiple sidebands at the optical frequencies needed for trapping. The modulator handles only low optical power (below 10mW), and we amplify the output light using a double-pass tapered amplifier (Eagleyard EYP-TPA-07800-01000) [48, 49]. The amplifier saturates at 0.5 mW of input light to get 1 W out. The input saturation power is lower than reported before [48], probably because of better mode matching to the tapered amplifier from the output fiber of the modulator. To inject the current into the amplifier, a daily consideration is first to check the power of the light in the single pass and finally after the double pass to maximize it using the corresponding mirrors. There is an issue with the spatial shape of the beam after the double pass, the beam has two lobes that interfere in the far field. Because of that we block one of the lobes using an iris. By blocking that, we end with less power (260 mW) sent to the trap but with a reasonable transverse shape.

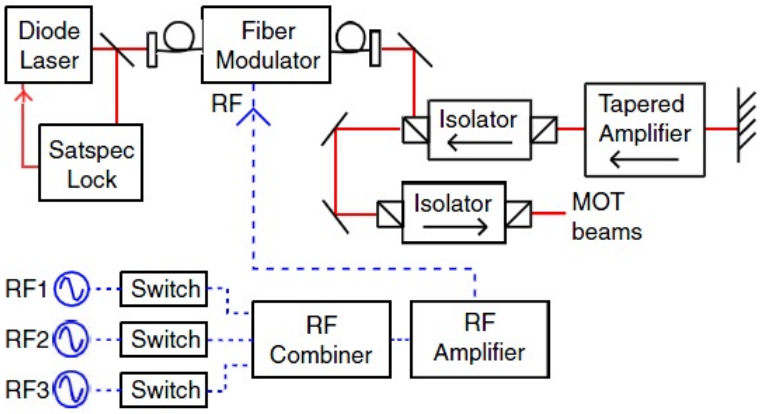

Figure 3.2: Experimental setup. The Solid red lines are the optical paths and the dashed blue lines are the RF parts [28].

The light then goes into the three retro-reflected MOT beams. No other beam is needed at this point, since the positions of the sidebands match the required optical frequencies for trapping both isotopes. Traps with three different isotopes [21] could be easily implemented using this system. Since we lock the laser to one of the repumping transitions, we need to add only three different RF frequencies to the modulator to get a DIMOT. Upper trace of Fig 3.3 shows the Doppler broadened spectrum of rubidium. The two outer peaks correspond to the ground hyperfine splitting of ^{87}Rb and the two inner ones to ^{85}Rb. Each Doppler broadened peak contains three excited state hyperfine transitions indicated by black vertical lines (middle trace). We lock the laser to the $5S_{1/2}$ $F = 1$ to $5P_{3/2}$ $F = 2$ transition of ^{87}Rb that corresponds to the repumping transition. The position of this (carrier) laser is indicated by the tallest line in the lowest trace of the Fig 3.3. We produce sidebands with an RF frequency of RF_3=6589 MHz for the ^{87}Rb trap laser, RF_2=5458 MHz for the ^{85}Rb trap laser, and RF_1=2545 MHz for the ^{85}Rb repumper laser (lower trace of Fig 3.3). These frequencies are chosen such a way to make the trap laser by

19 MHz off resonance. Extra frequencies also appears because of non-linearity of the EOM which are RF_3-RF_2=1131 MHz and RF_3+RF_2=12047 MHz with very low power. The frequency of the second order of the harmonics for the trap lasers are $2RF_3$=13178 MHz and $2RF_2$=10916 MHz that are far enough from the resonance of DIMOT. Table 3.1 shows the frequencies of the all possible non-linearities (second and third order) made by RF_1, RF_2 and RF_3. The red and blue lines in lower trace of Fig 3.4 show the mentioned undesired frequencies in Table 3.1 which are close to the resonant zones. These non-linearities still do not threat the resonant frequencies shown in the upper trace of Fig 3.4. According to the Table 3.1 the taller red and blue lines are the closest (368 MHz) non-linearities to the resonances shown with taller black lines in lower trace of Fig 3.4.

The ^{85}Rb repumper sideband is smaller since the power needed is less than that for the trapping beams. The trap size is relatively constant over a broad repumper frequency range. All the blue detuned sidebands in the Fig 3.3 are far from the resonance and they have no noticeable effect on the atoms. The detunings from the closest transition for the trap laser of the ^{85}Rb and the ^{87}Rb are 8 GHz and 9 GHz, respectively.

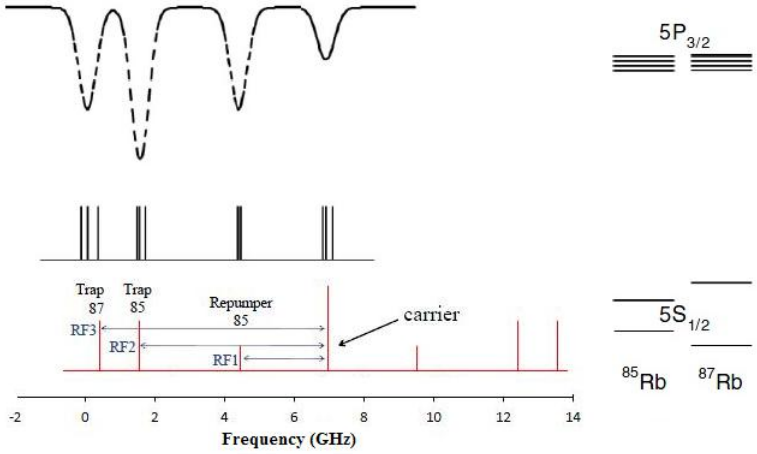

Figure 3.3: Spectrum of rubidium. The upper trace (dashed black line) shows the Doppler broadened spectrum of rubidium. The middle trace (solid black line) shows the excited state hyperfine transitions with the zero frequency corresponding to the leftmost transition. The lower trace (solid red line) shows the spectrum of laser light out of the fiber modulator. The tallest peak is the carrier and the rest are sidebands. The three left sidebands are tuned to the required transitions for the DIMOT. The laser is locked at the carrier position. The energy levels for the two isotopes are shown on the right [28].

We use the simplest implementation that gives us control over the repumper of ^{85}Rb, but not over the repumper of ^{87}Rb, since that corresponds to the carrier. This last beam could be set out of resonance with the use of AOMs to shift the frequency, or by locking the laser at a different frequency. An extra RF frequency must be injected into the modulator to recover and control the repumper beam

Non-linearities	**Frequency (MHz)**
$2RF_1$	5090
$2RF_2$	10916
$2RF_3$	13178
RF_1+RF_2	8003
RF_1+RF_3	9134
RF_2+RF_3	12047
RF_1-RF_2	-2913
RF_1-RF_3	-4044
RF_2-RF_1	2913
RF_2-RF_3	-1131
RF_3-RF_1	4044
RF_3-RF_2	1131
$3RF_1$	7635
$3RF_2$	16374
$3RF_3$	19767
$RF_1+RF_2+RF_3$	14592
$RF_1+RF_2-RF_3$	1414
$RF_1-RF_2+RF_3$	3676
$RF_1-RF_2-RF_3$	-9502
$RF_3-RF_2-RF_1$	-1414
$RF_2+RF_3-RF_1$	9502
RF_2-2RF_1	368
RF_3-2RF_1	1499
RF_1-2RF_2	-8371
RF_3-2RF_2	-4327
RF_1-2RF_3	-10633
RF_2-2RF_3	-7720
$2RF_1+RF_2$	10548
$2RF_1-RF_2$	-368
$2RF_1+RF_3$	11679
$2RF_1-RF_3$	-1499
$2RF_2+RF_1$	13461
$2RF_2-RF_1$	8371
$2RF_2+RF_3$	17505
$2RF_2-RF_3$	4327
$2RF_3+RF_1$	15723
$2RF_3-RF_1$	10633
$2RF_3+RF_2$	18636
$2RF_3-RF_2$	7720

Table 3.1: Undesired frequencies due to the non-linearities of EOM made by RF_1, RF_2 and RF_3 signals.

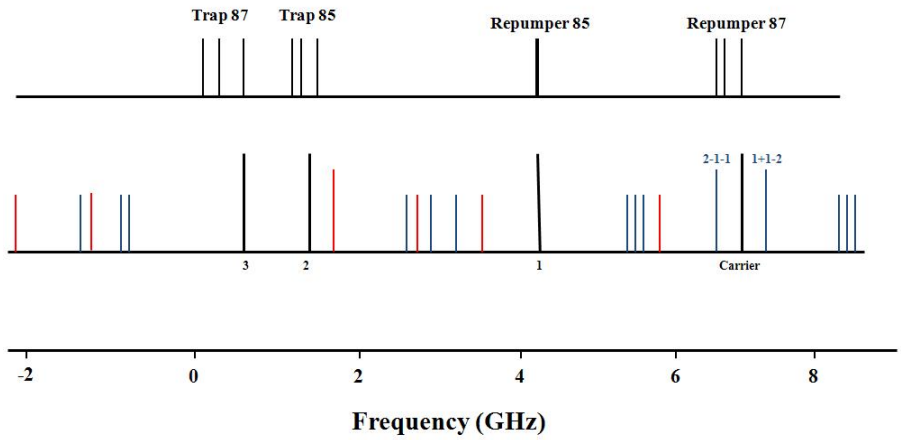

Figure 3.4: The second (red lines) and third order (blue lines) non-linearities made by RF_1, RF_2 and RF_3 signals (see Table 3.1). The taller red and blue lines are the closest (368 MHz) non-linearities to the resonances shown with the black lines. 1, 2 and 3 stands for RF_1, RF_2 and RF_3.

of ^{87}Rb. Turning the light completely off in our implementation must be done after the tapered amplifier. If an AOM is used to do it, then that will introduce an extra frequency shift for all the beams that needs to be taken into account when calculating the fiber modulator RF frequencies. An alternative is the use of very fast mechanical shutters that introduce no frequency shift [50]. The fiber modulator gives all the flexibility needed for atomic physics experiments. For example, to do optical molasses one needs to rapidly change the detuning of the trap laser. This is achieved by simply changing the corresponding RF frequency. We turn off a particular beam by just removing the RF, something that is done quickly and with a high extinction ratio. An additional beam for optical pumping to the lower ground hyperfine level can be obtained by adding the corresponding RF frequency to the fiber modulator.

3.3 RF world

The RF system for the fiber modulator is shown with the blue dashed lines in Fig 3.2. We have three separated oscillators to generate the required RF frequencies. Each oscillator is followed by an RF switch (Minicircuits ZFSWA2-63DR+) to turn off that frequency. We combine the three different frequencies using an RF splitter/combiner (RF Lambda RFLT3W2G08G). We chose this kind of splitter because of its low insertion loss (1 dB) and good isolation (18 dB) in contrast to a resistive one that has an insertion loss higher than 3 dB and poor isolation. The maximum input power (1 W) is also higher than the resistive one and after combination, the signal looks quite linear. We amplify the RF signals with a 35 dB amplifier (Minicircuits ZVE-3W-83+) that covers the entire range, and we send this signal to the fiber modulator.

There are two options for the oscillators (see Fig 3.5 a and b), one based on phase-locked loop (PLL) synthesizers and the other based on voltage con-

trolled oscillators (VCOs). For the first option we produce the 2545 MHz signal directly from a PLL synthesizer (EVALADF4350-EB2Z) that has a precision better than 1 Hz. Thanks to the rubidium atomic clock (Stanford Research Systems model:FS725), the accuracy of the frequency is 11 digits. The output signal from these synthesizers have very small variations around the desired frequency. The 5458MHz signal uses the same synthesizer, but we double (Minicircuits ZX90-2-36S+) and filter (Minicircuits VBFZ-5500-S+) the RF frequency to eliminate any unwanted harmonics. The same scheme works for the 6589 MHz signal we need, but we use another synthesizer (Gigatronics 1018) that directly gives the correct RF frequency. This choice of oscillators is useful for the situations when the high precision in frequency is important, but it is not very practical for making frequency changes. Each AD card must be connected to the computer through the USB connection and the change in the frequency must be applied via changing manually the parameter in the program.

Alternatively, we have also used Voltage Controlled Oscillators (VCOs) that are readily tunable with voltages derived from our control system. One needs to apply a small voltage to cover the wide frequency range. Fig 3.6 shows the linear dependence of the output frequencies for three VCOs which are fairly linear with the applied V_{tune} voltages. The ease of use comes from this fact that to generate the signal, the only thing we need is to apply a proper voltage. Therefore, we must consider the voltage and temperature variations than can be problematic. We measured the sensitivity to the voltage in the room temperature for the VCO_1=96 MHz/V (Minicircuits ZX95-3360-S+), VCO_2=67 MHz/V (Minicircuits ZX95-5776-S+) and VCO_3=87 MHz/V (Minicircuits ZX95-6840C-S+). Since we want frequency variations smaller than 100KHz in our DIMOT, by rounding the sensitivity in one of the VCOs to 100 MHz/V and considering V_{tune}=5 V, the voltage source requirements in terms of stability gives 2 parts in 10^{-4}. The VCO_2 with smaller voltage sensitivity gives better stability.
With this consideration, we designed a circuit that distributes the stabilized voltage in each VCO. The circuit of the voltage is demonstrated in Fig 3.7. VCO_1, VCO_2 and VCO_3 work in a different frequency range and are adjusted to generate 2.7 GHz, 5.6 GHz and 6.7 GHz respectively. We feed the circuit with $\pm$13 V and the voltage is stabilized using a very stable reference (LM399) which gives a stable 7 V to feed the V_{tune} via a voltage divider. There is an operational amplifier (TL084) in the circuit accompanied with the RC components to filter the noise and to add the voltage coming from the control system that we use to sweep the frequency. There are also three +12 V (model: L7812CT), -12 V (model: L7912CT) and +5V (model: 7805CT) regulators to feed the different components. Thanks to the 5 kΩ R_2, R_6 and R_7 resistors, the noise coming from the control system reduces 5 times when it goes to the V_{tune}. Due to that, we need to ask 5 times bigger voltage from the control system.
It is important to consider VCOs fast frequency changes. We are interested in sweeping the frequency since it has application in the optical molasses. During the molasses, we apply a change of 60 MHz for the detuning of the trap laser in 1 ms and the measured sweep rate for all of them is 158 $\pm$23 MHz/μs which is more than enough for the molasses. To measure the sweep rate, the trick is to deal with low frequency (less than 100 MHz) to be able to monitor in a oscilloscope. Figure 3.8 (a) shows the block diagram of the experiment. It is necessary to have a reference frequency close to the one under study. After mixing two signals using a mixer (Minicircuits model: ZX05-73L-S+), the output

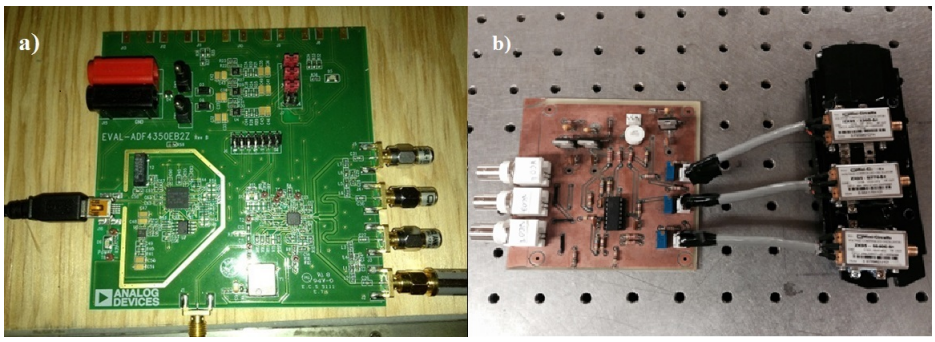

Figure 3.5: Oscillators. a)PLL synthesizer, model: EVALADF4350-EB2Z , b) VCO's from Minicircuits, models: ZX95-3360-S+, ZX95-5776-S+ and ZX95-6840C-S+ are connected to a voltage stabilizer circuit at the left hand of the picture.

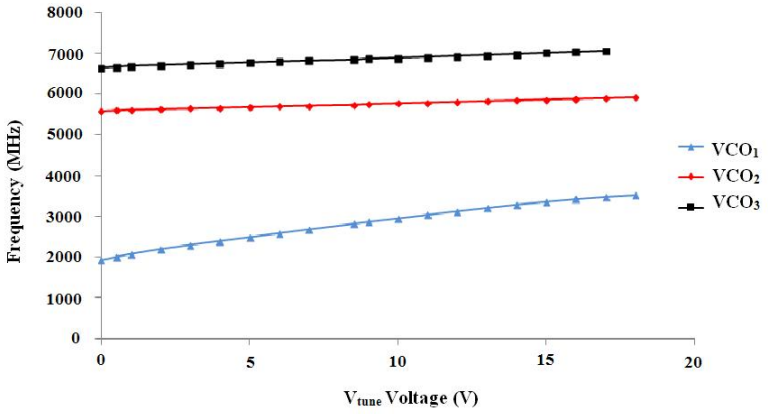

Figure 3.6: Output frequencies of three available VCOs versus applied V_{tune} voltage.

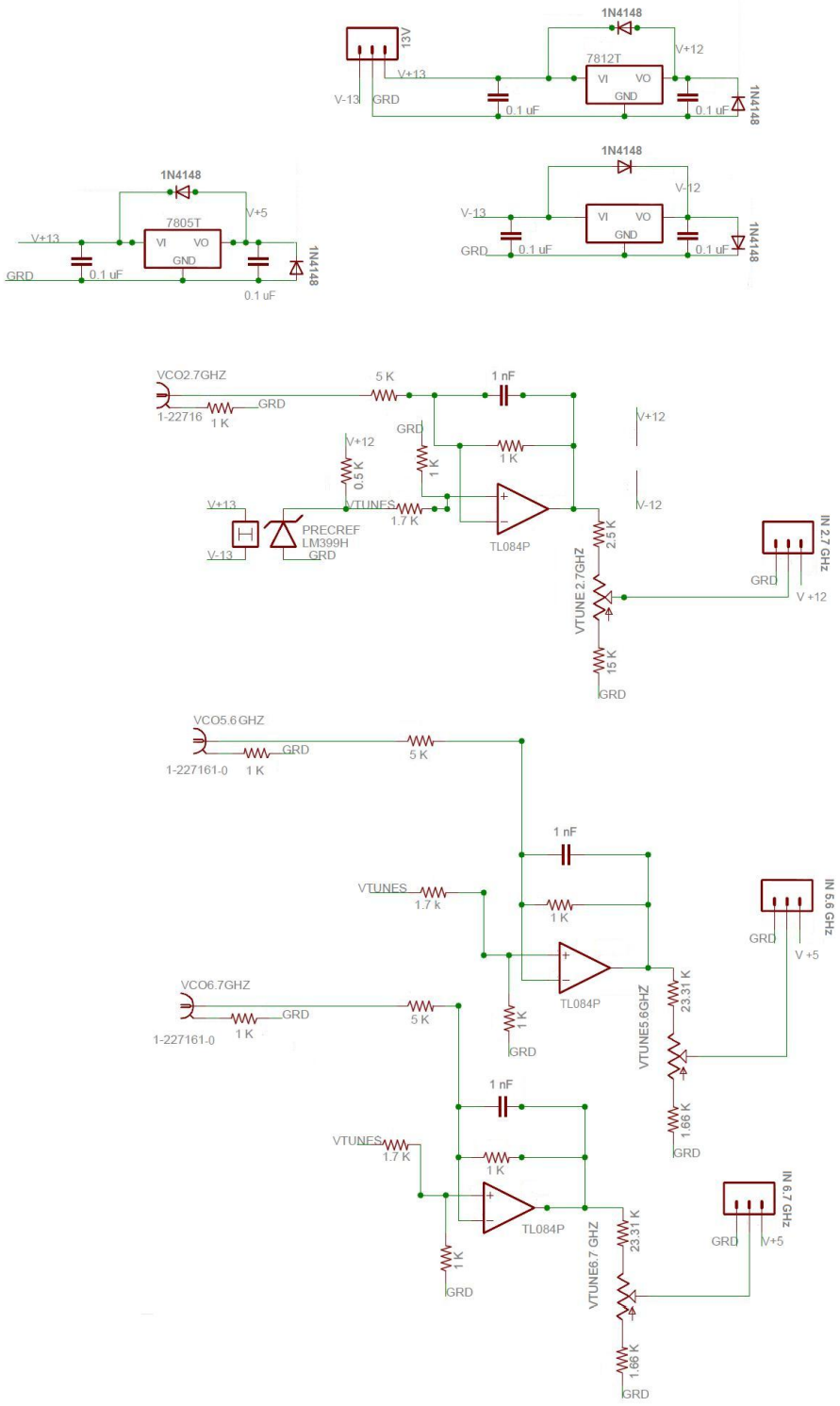

Figure 3.7: The diagram of voltage stabilizer circuit for the VCOs.

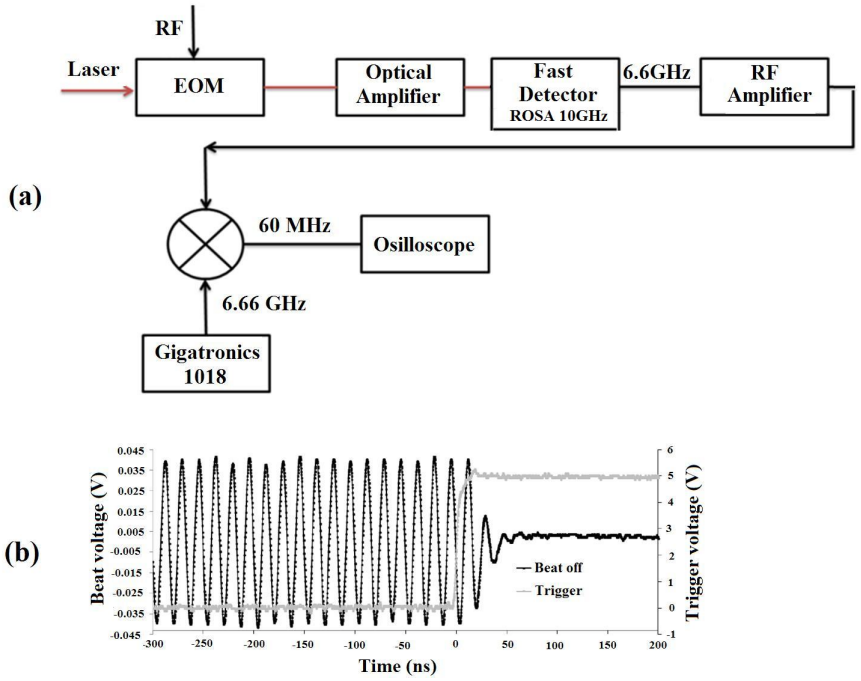

Figure 3.8: Fast turn-off of the sidebands using RF switch. (a) Experimental setup to measure the turn-off time. (b) The result of the output signal of the mixer.

frequency is the difference of two inputs. This low frequency signal is detectable in the oscilloscope. The optical amplifier reduces the sweep rate to 30 MHz/μs which is measurable here by more and less the same discussed trick. We send the output light of the EOM and amplifier to a fast detector (ROSA 10 GHz) which gives a beat note and we mix it with a reference signal using the same mixer. The output of the mixer is a 30 MHz signal can be interpreted in the oscilloscope.
The temperature also affects the VCOs behavior. We found that running the VCOs without any feedback system introduces 2 °C fluctuations which translates on at least 1 MHz change in the frequency. Therefore, the temperature stabilization considered uses an adhesive heater (HT10K) under the VCOs that was connected to a PI controller circuit (Thorlabs, model: TCM1000T). To send enough power to the heater, we need to amplify the output current of the controller using the homemade circuit shown in Fig 3.9. The circuit voltage range is from 12-15 V. It has a 5 V regulator which provides the power for the TCM1000T too. A transistor (TIP31C) enables the current increase proportional to the input and up to 2 A.

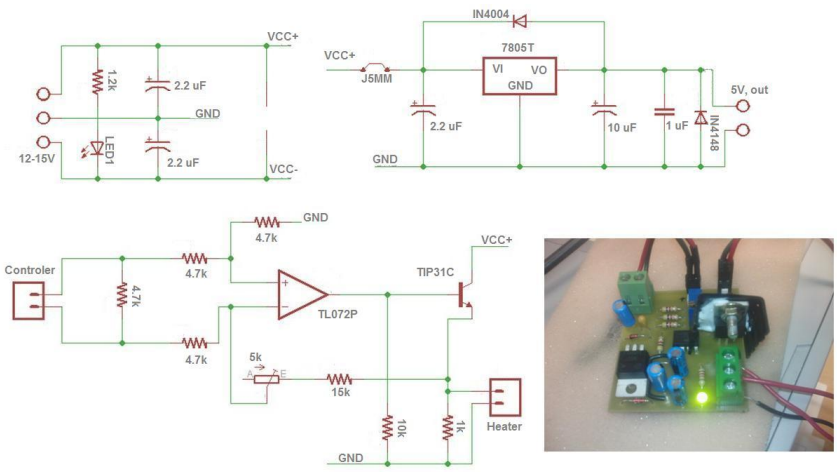

Figure 3.9: The diagram of the circuit used for amplifying the output current of the PI controller (TCM1000T) to stabilize temperature of VCOs.

The RF switch has a power reduction of 40 dB in the off mode. It is capable of turning off the laser beam in just 35 ns (3 ns switches are available). This is very convenient not only for the atom trapping but also for the measurements that require fast turn-off times. For example, lifetime measurements require turn off times of less than 10 ns, which is usually achieved using Pockels cells and AOMs [56]. Pockels cells have fast switching times (a few nanoseconds) but a bad extinction ratio (less than 20 dB) and they have to be shielded since they broadcast a lot of RF; AOMs have a good extinction ratio (40 dB), but they are slower (more than 30 ns). There is an advantage in turning off an RF signal rather than a DC signal. Using the fiber modulator, one obtains fast switching (3 ns), a good extinction ratio (40 dB) and almost no RF broadcasted. A fiber modulated beam could be added to a traditional trapping setup, but here it is already included in the system. We use a single broadband RF amplifier for

all the frequencies. This low noise amplifier gives enough gain (minimum 30 dB) to boost the power. We inject low RF powers (3.2 dBm at 6589 MHz, 3 dBm at 5458 MHz, and -3.2 dBm at 2545 MHz) into the fiber modulator to reduce nonlinear effects as we explain in the next section. The non-linearity at the RF amplifier introduces two extra frequency components equal to the sum and difference of the trapping beams' RF frequencies. The amplitude of these nonlinear components, however, is 27 dB below the trapping RF frequency level. Any spurious frequency becomes important only if it happens to be on resonance with some transition. The spurious frequency that gets closest to a particular resonance is 312 MHz away, and it is not visible up to a power of 63 dB below the trap RF power.

3.4 Optical modulation

Here in this section we describe the amplitude (AM) and phase modulation which have many applications in science, communication, etc. In AM as the name suggests, the carrier amplitude changes in accordance with the amplitude and frequency variations of the modulating signal. The carrier frequency remains constant during the modulation process, but its amplitude varies with the modulating signal. AM is used to transmit the voice by the radio. The electric field of the carrier signal has a sinusoidal form, by adding the modulation part we get

$$\begin{aligned} E(t) &= A_c(t)\cos(\omega_c t) \\ &= [A_0 + \frac{B_0}{2}(e^{i\Omega_m t} + e^{-i\Omega_m t})]\frac{1}{2}(e^{i\omega_c t} + e^{-i\omega_c t}) \\ &= A_0\cos(\omega_c t) + \frac{B_0}{2}\cos((\omega_c + \Omega_m)t) + \frac{B_0}{2}\cos((\omega_c - \Omega_m)t) \end{aligned} \tag{3.1}$$

The carrier is unchanged and two sidebands are created with frequencies slightly above and below the carrier. The same analogy is used for the phase modulation, in this case the instantaneous variation occurs for the phase of the carrier.

$$\Xi(t) = A_c\cos(\omega_c t + \varphi_c) \tag{3.2}$$

The modulated signal can be written as

$$\begin{aligned} \Xi(t) &= A_c\cos(\omega_c t + B\sin(\omega_m t)) \\ &= A_c\cos(\omega_c t)\cos[B\sin(\omega_m t)] - A_c\sin(\omega_c t)\sin[B\sin(\omega_m t)] \end{aligned} \tag{3.3}$$

We assume that B is very small and with this approximation $\cos[B\sin(\omega_m t)] \approx 1$ and $\sin[B\sin(\omega_m t)] \approx B\sin(\omega_m t)$, then we have

$$\begin{aligned} \Xi(t) &\approx A_c\cos(\omega_c t) - A_c\sin(\omega_c t) \times B\sin(\omega_m t) \\ &\approx A_c\cos(\omega_c t) + \frac{1}{2}BA_c(\cos[(\omega_c + \omega_m)t] - \cos[(\omega_c - \omega_m)t]) \end{aligned} \tag{3.4}$$

It is clear that there is a term for the carrier signal with the frequency of ω_c and two sidebands are modulating with $(\omega_c \pm \omega_m)$ frequencies. The commercial intensity modulators are based on a Mach-Zehnder interferometer such as in one path they use a nonlinear crystal (Pockels or Kerr medium) which is connected

to a voltage or a heater. In the case of the intensity modulator, the modulation is obtained by creating the phase differences between the two arms of the interferometer using the electric field thanks to the applied voltage, therefore here we induce the phase modulation. In the phase modulator, by applying the heat to the crystal, it expands and the index of refraction varies. This leads to a phase shift φ=n(E)k_0L [51]. For example, a π shift corresponds to a $\lambda/2$ path length change.
We chose an intensity rather than a phase modulator, since the latter one gives many sidebands and in our experiment the ones close to the resonance might be problematic. Although, our modulator creates higher order sidebands due to its non-zero chirped feature. Our EOM is designed to be used in the TM mode with a voltage for a π phase shift in the modulator of $V_\pi = 1.1$ V at DC. It has a crystal inside of LiNbO3 type, the insertion loss is 3.2 dB and the DC extinction ratio (a ratio of the powers when the source is on and off respectively) is 19 dB. The input light power must not exceed 10 mW to avoid damaging the crystal. We align the input polarization using a well defined axis of the fiber. If the input light polarization is matched to a precision of 1^o respect to the axis of the fiber (fast axis mode) we get the less output power from EOM, but a good polarization maintenance in it.

In absence of the fast mode matching, the output intensity modulation varies a lot with just 0.2 ^{o}C temperature changes. In addition of sending the light with the correct polarization, we also cover the EOM with a box from surrounding environment to make an stabilization for the temperature. In parallel, we use the same feedback system as described in the above section for VCOs. The output power of the fiber modulator sinusoidally oscillates and thanks to the mentioned consideration keeps the output power of the fiber modulator at one half of the maximum output power to have the best sideband efficiency. According to Eq 3.5, we lock the intensity in half of the modulation signal because the size of the sidebands are maximum there. For example we cannot lock the intensity of the modulator in the peak because then the slope is zero and if we change voltage, intensity does not change, so we want to have the biggest slope and it's in half of the signal and it also gives the highest modulation signal. A schematic of fiber modulator and the place we lock the intensity is shown in Fig 3.10. The output power lock is not necessary when using a phase modulator instead of an intensity modulator but the nonlinear response will change as well, since phase modulators has no DC input voltage. The electric field at the output path of the interferometer in the EOM is given by

$$E = \frac{E_0}{2}\left[\cos(\gamma t) + \cos\left(\gamma t + \pi\frac{V_0}{V_\pi}\right)\right], \tag{3.5}$$

with γ the light frequency and V_0 the input voltage to the modulator. The zero-chirped versions among the intensity modulators have nonlinear crystal in two paths of interferometer and the second crystal induces a phase shift with exactly opposite sign of the first one (-$\pi\frac{V_0}{V_\pi}$) which results in Eq 3.1. Figure 3.11 (red squares) shows the first order sideband amplitude as a function of the input RF power when we modulate at 5.6 GHz. The input RF power should not exceed 27 dBm for our modulator model. We measure the sideband amplitude by looking at the transmitted light on a Fabry-Perot cavity with 1.5 GHz free spectral range (model: SA200-12B) to identify each frequency component separately. The solid red line is a fit to the theoretical dependence on RF power given by

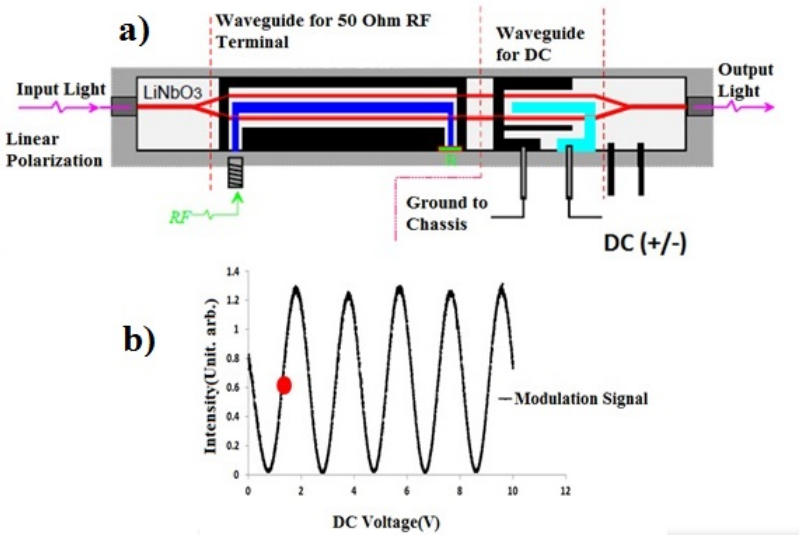

Figure 3.10: Fiber modulator. a) schematic of fiber modulator, b) output intensity of modulator versus DC voltage, the red point shows the locking point of the intensity.

$$S_1 = J_1^2\left(\frac{\pi V_m}{V_\pi}\right), \tag{3.6}$$

where V_m is the amplitude of the modulating RF voltage and J_1 is the Bessel function of the first kind. It is straightforward to obtain the V_m from RF power using P=V^2/R, where we consider a 50Ω resistance in the connection.
An applied voltage in a crystal presents a phase change of

$$\begin{aligned}\varphi &= \varphi_0 - \pi\frac{\varsigma E L n^3}{\lambda_0} \\ &= \varphi_0 - \pi\frac{V_m}{V_\pi}\end{aligned} \tag{3.7}$$

The Appendix B gives the derivation of Eqs 3.6 to 3.9. The fit to the data gives a $V_\pi = 3.32\pm0.08$ at 2.7 GHz, $V_\pi = 4.17\pm0.08$ at 5.6 GHz and $V_\pi = 3.80\pm0.06$ at 6.8 GHz. The dependance of V_π to RF frequency comes from bandwidth for the modulator. At high input RF powers the modulator generates a second order sideband. The size of the second order sideband is shown in Fig 3.11 (green triangles) together with the theoretical value (solid green line) given by

$$S_2 = J_2^2\left(\frac{\pi V_m}{V_\pi}\right). \tag{3.8}$$

The output power P of the fiber modulator is set by the DC voltage port. The visibility V=(P_{max}-P_{min})/(P_{max}+P_{min}) of the output power of the modulator decreases as we increase the input RF power (blue diamonds in Fig 3.11). The visibility is reduced since the photo detector averages the modulated signal over a certain voltage range. The solid blue line is the theoretical value given by

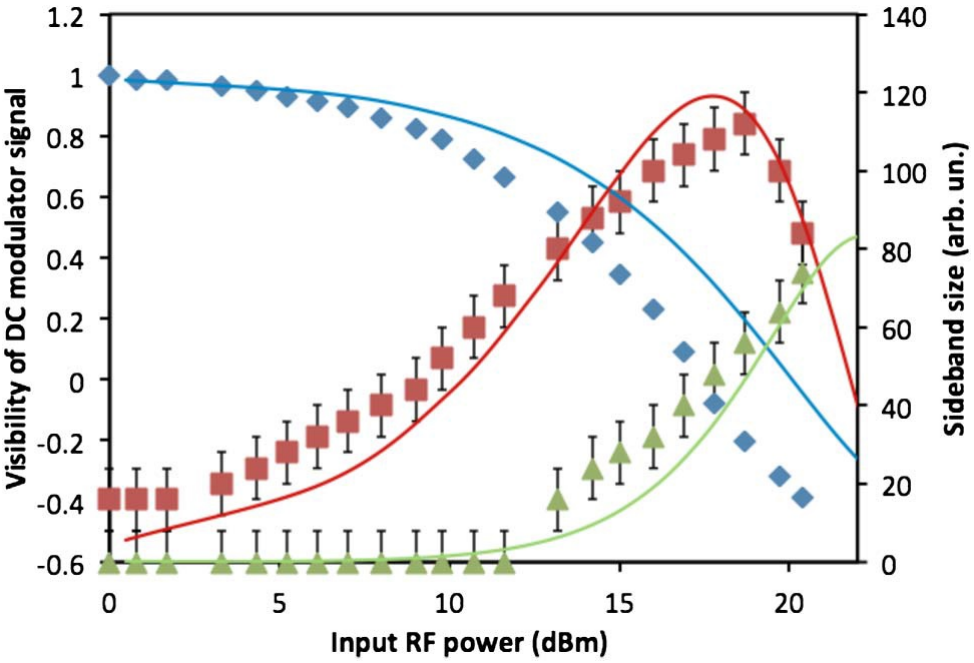

Figure 3.11: Fiber modulator characterization. It shows the first order sideband amplitude (red squares), second order sideband amplitude (green triangles), and visibility of the DC locking signal (blue diamonds). The solid lines correspond to the theoretical values. The fit is done to the first order sideband to obtain the three curves as indicated in the text. The second order sideband signal is buried in the noise for RF powers below 13 dBm [28].

$$S_L = J_0\left(\frac{\pi V_m}{V_\pi}\right). \tag{3.9}$$

A good visibility is important in order to keep the output power of the laser locked. The visibility goes to zero at a particular input RF power and the output intensity of the fiber cannot be locked there. The visibility becomes negative (reverses sign) at even higher RF powers and one must invert the sign of the feedback in order to keep the output power locked.

All the theoretical curves in Fig 3.11 are obtained with a single set of parameters determined by a fit to only the first order sideband data. Even when better results could be achieved with independent fits, the agreement obtained using a single set of parameters shows a clear understanding of the process. The small discrepancy observed in the visibility fit may be due to the finite bandwidth of the detector used.

The amplitude of the first order sideband is maximum at a power of 18 dBm (corresponding to about 30 % of the total optical power in a single sideband), but at this power one gets a considerable amount of the second order sideband. Also the visibility of the intensity modulation goes to zero and it is not possible to lock the output power of the fiber modulator. Adding more than one frequency produces quite a bit of frequency mixing at high RF powers. We operate at lower RF powers (3 dBm) to reduce the appearance of additional frequencies and we have sidebands with about 7 % of the total optical power.

In Fig 3.12 the optical spectrum after the tapered amplifier is obtained using a Fabry-Perot cavity. This cavity is a multiple beam interferometer which consists of two mirrors with high reflectivity. It is possible to scan the cavity by varying the mirror separation with a piezoelectric transducer. In our case we scan the piezo and thus the cavity length changes and instead we keep fixed the laser frequency to get the spectra of the beam entering the cavity. By doing that, when the cavity length becomes equal to an integral number of half the wavelength, due to the constructive interferences of multiple reflected lights, a series of periodical peaks appear. The distance between two peaks is called the free spectral range which in our case is 1.5 GHz. The total transmission of the light in the cavity can describe by

$$\frac{I_t}{I_i} = \frac{T^2}{1 + R^2 - 2R\cos\delta} \tag{3.10}$$

where I_t and I_i are the transmitted and incident flux densities, respectively and T is total transmittance, R is reflectance. There can be an additional phase shift $\delta = k.d$ introduced by the mirrors [62]. As Fig 3.12 shows, the tallest peaks indicate the carrier. One must be careful to identify the exact sidebands corresponding to the exact carriers. For instance, by focusing on a particular peak like RF_3=6.589 GHz (trap laser of ^{87}Rb), it is important to look for the proper sideband keeping in mind 1.5 GHz is the free spectral range. The sidebands corresponding to the traps (ν_1= 6589 MHz and ν_2= 5458 MHz) and repumper (ν_3= 2545 MHz) frequencies and have a height equal to 7 %, 8 % and 4 % of the carrier. Additional peaks corresponding to the sum (12047 MHz) and difference (1130 MHz) of the trapping frequencies are also visible but they are very far from any resonance to be of importance. Blue detuned sidebands are also visible and make the figure symmetric.

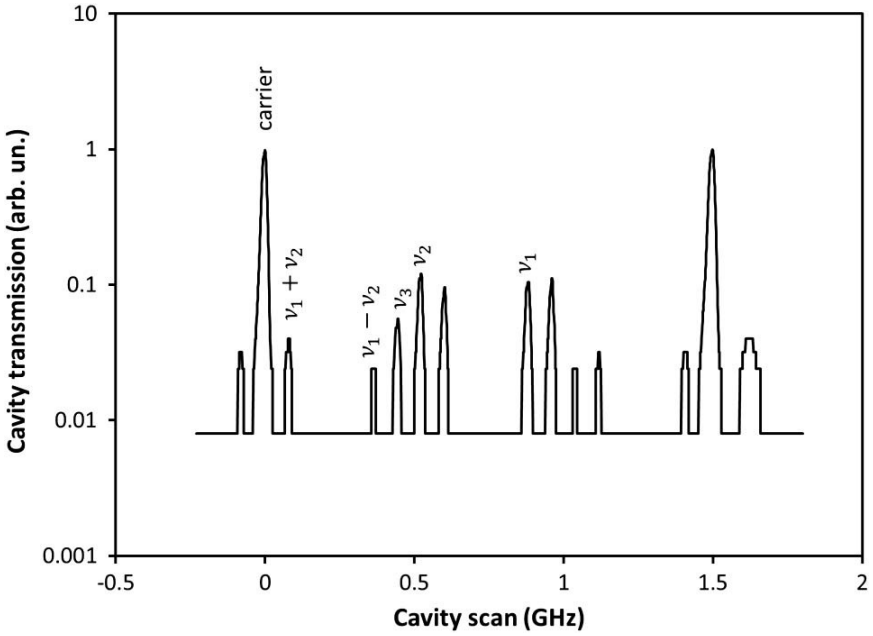

Figure 3.12: Optical spectrum after the tapered amplifier measured in a Fabry–Perot cavity. The tallest peaks indicate the carrier and free spectral range of the cavity (1.5 GHz). The peaks with ν_1=6589 MHz and ν_2= 5458 MHz correspond to the trapping frequencies, and the peak with ν_3=2545 MHz is the repumper frequency. The non-linearity and blue detuned sidebands are also visible [28].

The input RF power used (3 dBm) gives good modulation efficiency but still let us treat each trapping frequency almost independently since changes of one introduce variations on the other sideband smaller than 10 %. This is not the case at higher RF powers where we see considerable frequency mixing and a strong influence on the presence or absence of one sideband over the size of the other. At low Rf levels the output power of the fiber modulator remains stably locked when switching the RF on and off. The tapered amplifier gives high output power (1 W) and it is simpler to use than diode laser injection locking [33]. It has a gain range of 20 nm around 780 nm which is more than enough for isotope shifts, but it is usually not enough for different atomic elements. We observed no additional frequency mixing introduced by the tapered amplifier. Frequency mixing is expected to be small since any frequency difference is larger than 1 GHz [59]. Thermal fluctuations in the amplifier change the power distribution between carrier and sidebands. This effect seems to be coming from an etalon effect due to reflections on the end faces of the tapered amplifier. The effect is more evident for us probably due to the competition of amplification at different frequencies. At the highest current (3 Amp) in the tapered amplifier we see fluctuations of 20 % on the sideband efficiency for a period of 5 minutes whereas at lower currents (2 Amp) where the heat load is smaller the fluctuations are reduced to 7 % for the same time scale. The fluctuations should improve with better temperature stability. Both the amplifier and fiber modulator introduce no reduction on the speed of light switching. We tested how fast the output light of EOM is turn-off by each RF switch. The experimental setup is shown in Fig 3.8 (a). We send the output light to a fast detector and it gives an RF at 6.6 GHz, then we mix it with a reference signal using a mixer. The low frequency signal (60 MHz) is sent to the oscilloscope and we get the switching result in Fig 3.8 (b). The switching time we get (90 ns) is different than the specified by the company (35 ns). The input optical power to the tapered amplifier must not change rapidly to avoid the risk of damaging it. Feed forward strategies are applied when the amplifier is preceded by AOMs [48]. When using a fiber modulator this is not a big concern since the output power of the modulator remains constant as we change either the frequency or power of the RF injected to the modulator; V_π does not change too much by the RF frequency variations in 10 GHz bandwidth. Switching the RF off suddenly transfers the sideband power to the carrier keeping the total laser power constant.

3.5 Results of DIMOT

We use the system to obtain a simultaneous trap of the two stable rubidium isotopes. We capture 4×10^8 atoms of ^{87}Rb and a similar amount of ^{85}Rb. The number of atoms of each isotope depends on the laser power of the trapping beams. Using tapered amplifier, we send 260 mW of optical power to the atoms. Each trapping beam has a diameter of 3 cm and an intensity of 7.6 mW/cm^2. The sideband corresponding to ^{87}Rb (^{85}Rb) has 7 % (8 %) of the power and therefore the trapping intensity is 0.5 (0.6) mW/cm^2 respectively. The number of atoms trapped as a function of time is shown in Fig 3.13. At t=0 all RF switches are off and there are no atoms trapped. The sequence is: ^{87}Rb only - ^{87}Rb and ^{85}Rb - ^{87}Rb only, with each stage lasting for 10 s and we turn traps

off at the end. A clear increase is observed when both traps are on. Also the fluorescence does not go to zero at t=20 s since one of the isotopes still remains trapped. We imaged both traps separately to further verify that both isotopes are trapped simultaneously and we see a good overlap of 30 μm between the two clouds. The trap has a lifetime of 6 s limited by the quality of the vacuum. The noise observed in Fig 3.8 is partially due to the stability of our frequency locking system, but it has also some contribution from the intensity fluctuations of the sidebands described before. The steady state atom number remains constant for longer times up to fluctuations like those shown in Fig 3.13.

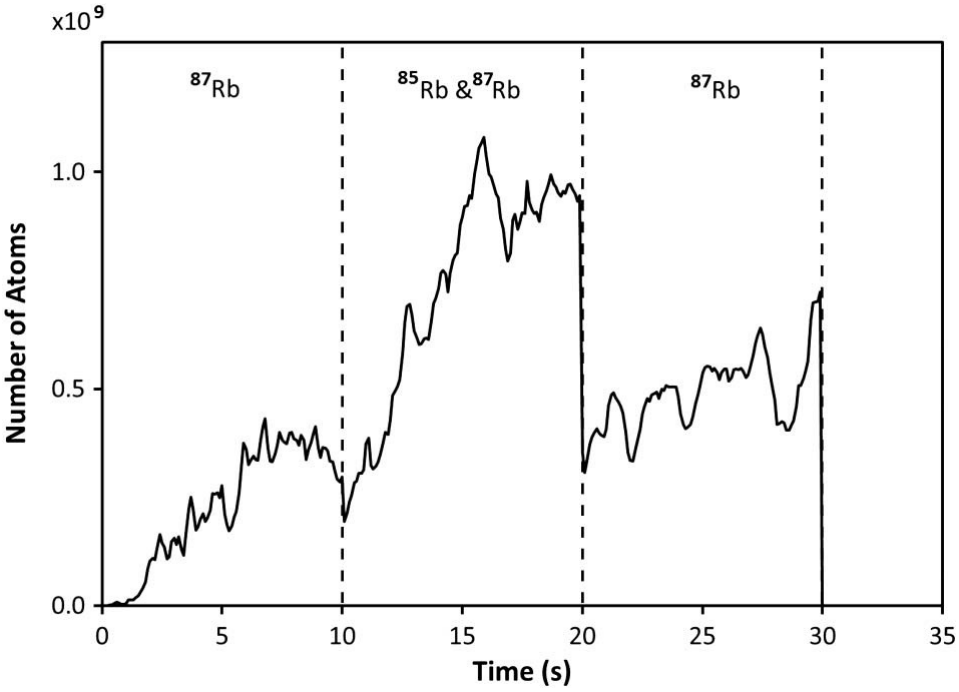

Figure 3.13: Atom number in the DIMOT. The sequence is ^{87}Rb only - ^{87}Rb and ^{85}Rb - ^{87}Rb only, with each stage lasting for 10 s; we turn the traps off at the end [28].

The two trapping beams are fairly independent of each other since turning one off changes the power on the other beam by no more than 10 %. Working at high RF power gives a nonlinear response but on the other hand it helps increasing the number of atoms. Setting the RF power of ^{87}Rb (6589 MHz) close to the diffraction efficiency maximum of Fig 3.11 translates into a 7 fold increase in the trapping power and gives a trap 3 times bigger. This means that we can trap in excess of 10^9 atoms.

We demonstrated a dual isotope trapping introduced as DIMOT. At the heart of the system a fiber intensity modulator simplifies the optics requirements. Just a single diode laser with three RF signals produce all the required optical frequencies. They are amplified simultaneously with a tapered amplifier to obtain high output power. The control of the different optical frequencies and their intensities is now moved to the RF side. We achieved an enormous

simplicity over traditional setups. We believe that this setup will promote the use of multiple species in atomic physics experiments.

Chapter 4

Preparations for atom interferometry

4.1 Introduction

The Ramsey sequence for our dual interferometer must start from a particular initial state. We require to do many preparation steps. First of all we need to capture the atoms in the MOT and further cool the atoms using an optical molasses (see Chapter 2). Once the atoms are prepared in $F = 2$ we apply optical and Zeeman pumping to send all of them to $|F = 1, m = 0\rangle$. Before discussing the experimental procedure for the initialization steps, we mention about some required elements in our work.
The interferometry uses the Ramsey method [57] where we apply initially a $\pi/2$ pulse for a duration of τ. The atomic cloud will be in a superposition states of two levels. Then we let them to evolve with the time T, this step happens during the darkness where all electromagnetic radiations and magnetic fields are switched off. The second $\pi/2$ pulse with the same duration recombines two clouds. We usually use the pulse durations (τ) an order of magnitude smaller than the evolution time (T). More times atoms being in the darkness, more precision for the transition is acquired.

4.2 Rabi oscillations

Atoms in any interferometer require to be initialized. Each mentioned pulse in the previous section induces the atoms to do the Rabi oscillations. Light interaction with a two level ground state system (an atom or even an ion) leads to an exchange of energy between the light field and the two level system. Rabi oscillations honored to the Nobel Prize winner Isaac Rabi [52], are interpreted as a periodic change between absorption and stimulated emission of photons. It also can be modeled using the Bloch vector formalism [53]. A destructive process that interrupts these oscillations, is the spontaneous emission. The angular frequency of the Rabi oscillations (2π times the number of Rabi cycles per second) is called the Rabi frequency. It is proportional to the amplitude of the light field and to the dipole moment of the level transition. Ω is the Rabi

frequency defined by [14]

$$\Omega \equiv \frac{-eE_0}{\hbar} \langle e \left| r \right| g \rangle , \tag{4.1}$$

where r is the electron coordinate. For a two level atom the dipole moment $e\vec{r}$ is parallel to the polarization $\hat{\epsilon}$ of the field. The Rabi frequency corresponds to the matrix element $\langle e \left| r \right| g \rangle$ which in general is not easily calculated for all atoms except the hydrogen. Since hydrogen's wave function in the bound states is well known, these elements can be calculated precisely [14]. The probability for finding the atom in the initial state $|g\rangle$ is $|c_g(t)|^2$ and in the excited state $|e\rangle$ is $|c_e(t)|^2$ which oscillates at frequency Ω'

$$|c_e(t)|^2 = (\frac{\Omega}{\Omega'})^2 \sin^2(\frac{\Omega' t}{2}), \tag{4.2}$$

where $\Omega' = \sqrt{\Omega^2 + \delta^2}$ and δ is detuning. In Eq 4.2 it was assumed that the atom is initially in the lower ground state $|g\rangle$. A resonant field (δ=0) gives the maximum visibility on the oscillations.

4.3 Microwave setup

Our first demonstration of Rabi oscillations is based on the clock transition $|F = 1, m = 0\rangle \longrightarrow |l\rangle$ to $|F = 2, m = 0\rangle \longrightarrow |u\rangle$. To see this result we do the following steps:

1. Prepare the atoms in $F = 2$ (MOT is active).
2. Send the atoms to the lower level $F = 1$ (Optical pumping).
3. Send the atoms to a specific sublevel in $F = 1$ (Zeeman pumping into $m = 0$).
4. Shine microwaves for a particular duration.

We load 10^9 ^{87}Rb in the MOT. The next step is sending the atoms to the lower level $F = 1$. We switch the repumper laser off. We transfer all the atoms to the lower level in 2 ms. Our plan is to pump them as fast as possible, therefore we used another laser beam (depumper laser). We obtain the depumper by sending a portion of the light after locking the trap laser into the crossover of $F' = 2$ and $F' = 3$, then this light goes to a double pass AOM (Model: R46110-.5 Gooch Housego) and the -1 order of diffracted light shifts the frequency of laser by 133 MHz and play the role of the resonant light to $F = 2 \rightarrow F' = 2$ transition. This beam goes through the cell once overlapped with one of the MOT beams. We retro-reflect this beam to avoid mechanical effects on the atoms. Thanks to the depumper laser, we are able optically pump the atoms into $F = 1$ level in less than 100 μs. Once the atoms are in $F = 1$ level, it is the time to use the microwave signal, we have our RF components ready to work.

A block diagram in Fig 4.1 shows the components that are used in the microwave side. We generate the signal by a synthesizer (EVAL-AD4350EB2Z), this card generates microwaves at 3.4 GHz which has a precision better than 1 Hz. Then we double that frequency using a doubler (ZX90-2-36-S+) to make the frequency close to the hyperfine gap in ^{87}Rb. Finally the 6.82 GHz signal goes as

the local oscillator input of the single sideband modulator (SSB4080A Polyphase MICROWAVE). We use another low frequency RF synthesizer (DS345 Stanford Research System) to do the frequency ramping since it is hard to scan at higher frequencies. The low frequency signal also enters from the intermediate frequency input and in the RF output we get the sum of these two frequencies as a single sideband.
The accuracy of our frequencies is good to 11 digits thanks to the atomic clock which is connected to both synthesizers. We use an RF switch (ZFSWA2-63DR+) to turn the signal on and off very fast (35 ns). A filter (VBFZ-6260-S+) clears all the non desired frequencies, and two amplifiers (ZRL-3500+, ZX60-24S+) are used to gain enough power. We amplify this last signal using a 30 dB gain amplifier (ZVE-3W-83+). The spectrum analyzer measures 31.5 dBm (which is around 1.5 W) output power to the horn. The amplified signal travels through the horn that is installed in one edge of the cell. The big axis of the horn corresponds to direction of the polarization of the magnetic part of the radiation B_{mw}.

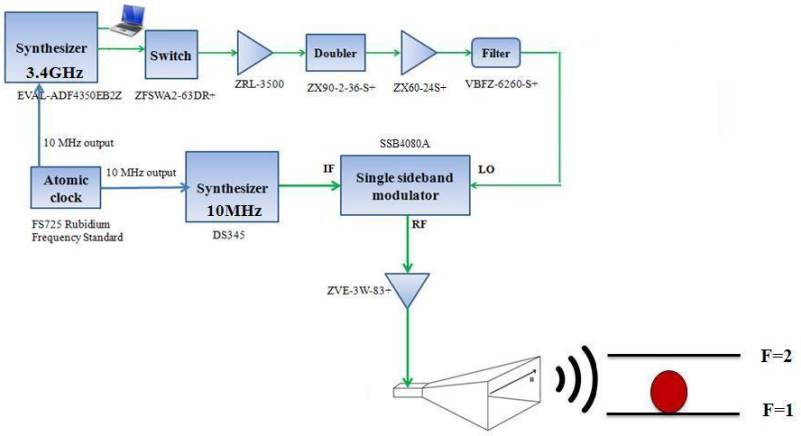

Figure 4.1: A block diagram shows the microwave system used for microwave spectroscopy.

4.4 Results

Depending on the polarization of the horn we can excite different transitions. In Fig 4.2, the possible polarizations are described for ground state of ^{87}Rb. Once the microwave shines, the atoms travel to the different sublevel addressed by the corresponding microwave polarization. All three different polarizations lead to 9 atomic transitions. We also need to turn the magnetic field gradient off beside considering a small delay for the IGBT (1 ms). We shine the microwave for hundreds of μs while all laser are off. Then we start to take an image using CCD camera or using the photodiode with the NI card (NI USB-6289).

We block the beams with mechanical shutters to ensure that there is no scattered lights coming from the lasers [54]. We use four of them and they are based on step motors. We verified 100 μs jitter time in each.

4.4.1 Demonstration of π polarizations.

Applying the microwaves we get 9 peaks as shown in Fig 4.3 which its vertical axes is proportional to the population in $F = 2$ and the horizontal one is the detuning. Pairs of transitions with circular polarization overlap with each other, that's why instead we see 7 peaks. The width of each peak differs from the other due to the different sensitivity to magnetic field fluctuation.

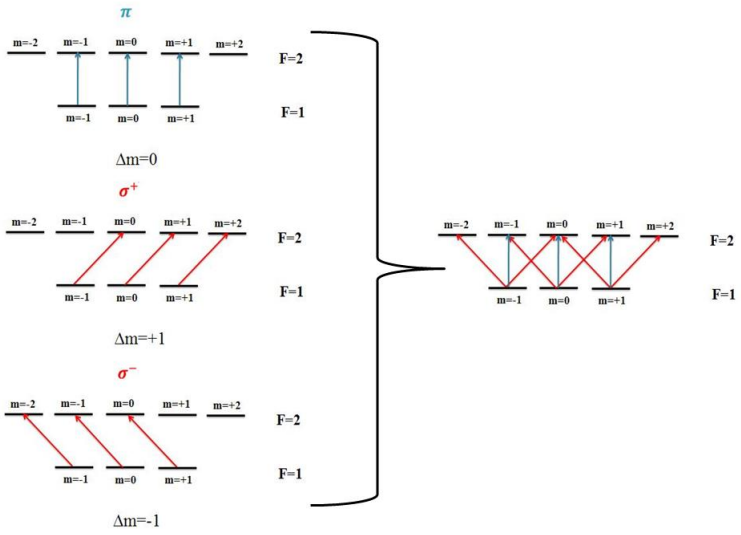

Figure 4.2: Microwave linear and circular polarization.

We see these 7 peaks because $\vec{B}_{static}$ has an angle with respect to the field of the microwaves $\vec{B}_{mw}$. By playing with the orientation of the horn field or changing the bias (static) field, we get the different results for the same spectroscopy. We aim to keep only π polarizations and eliminate the contributions of the circular polarizations. Once we get only π polarizations, it means that $\vec{B}_{static} \parallel \vec{B}_{mw}$. The result for the π polarizations is shown in Fig 4.4. The π polarizations plot is inverted for better comparison with the 7 transitions peaks. The bias magnetic field is slightly different for both plots. The height of these peaks helps us to determine what are the populations in each sublevels in $F = 1$.

We verified that varying the bias field in the low regime (hundreds of mG), does not affect the position of central peak which corresponds to the clock transition. But the other peaks have the frequency shifts due to their sensitivity to the magnetic field.

4.4.2 Zeeman pumping to a dark state

Here in this section we explain the initializing process of the atoms to a specific sublevel ($|l\rangle$). Figure 4.5 shows the extra beams used for the Zeeman pumping to $m = 0$. The beam corresponding to the $F = 1 \rightarrow F' = 1$ transition must be π polarized but the other laser beam which is not depicted in Fig 4.5 ($F = 2 \rightarrow F' = 2$) could have any arbitrary polarizations. In the case of the π polarized light, one of the transition as shown in Fig 4.5 is forbidden because of its zero

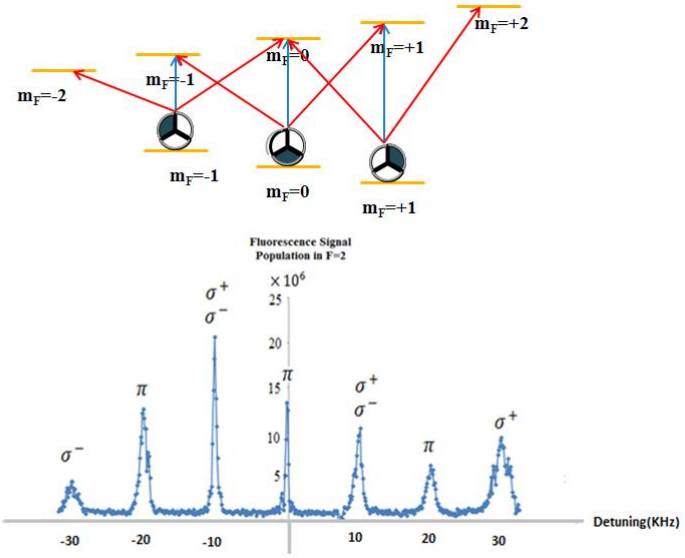

Figure 4.3: Microwave spectroscopy, the peaks correspond to the different transition.

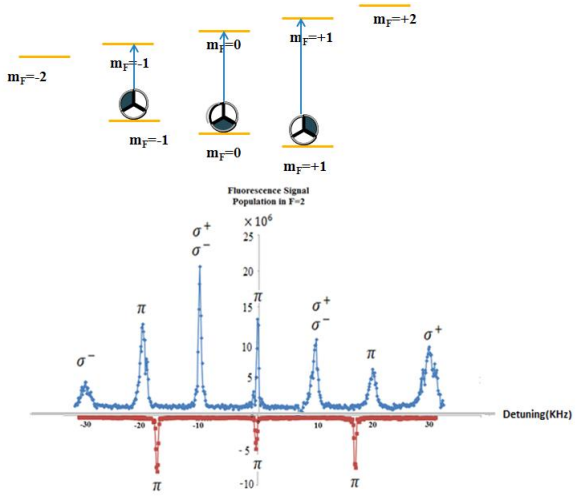

Figure 4.4: Demonstration of π polarizations, the blue line shows spectroscopy with 9 transitions and the inverted red one only π polarized transitions.

Clebsch-Gordon coefficient. Thanks to these two lasers, after a very short time we assure that all atoms fall into the dark state. In order to do Zeeman pumping, thanks to the repumper ($F = 1 \rightarrow F' = 1$) and depumper($F = 2 \rightarrow F' = 2$) lasers, we have all the frequencies we need. We split the repumper light into two path using a polarized beam splitter cube. The intensity of the π light is lowered to be less than the saturation intensity [55] (3 mW/cm^2) using an optical attenuator.
We found that a bias field of about 400 mG gives good results for Zeeman pumping. This field is acquired by adjusting the B_z in Agilent supply (Model: E3614A) which is remotely controlled via the control system.

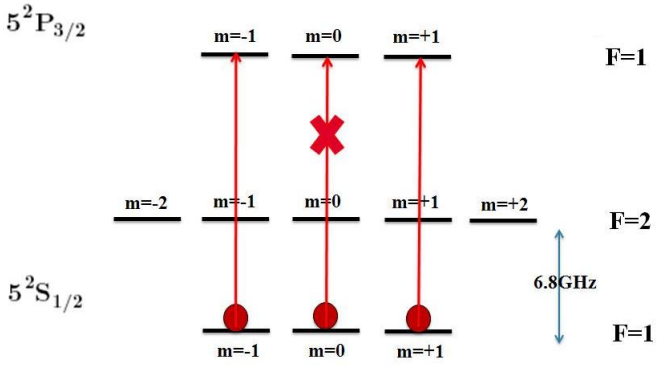

Figure 4.5: π polarized light for Zeeman pumping. Here part of ^{87}Rb D_2 transition hyperfine structure is shown. An extra laser is used to send the atoms into the dark state. The $F = 1 \rightarrow F' = 1$ laser must be π polarized (red).

We verify that we achieve more than 94 % of the atoms are in the correct state using microwave spectroscopy. The two mentioned lasers excite the atoms for a short duration (50 μs) before shining the microwaves. Figure 4.6 (red inverse) shows the result we get for Zeeman pumping. In this figure we see that only the three central peaks survive which are the ones that correspond to transitions starting from $|F = 1, m = 0\rangle$. We use this procedure from now on to initialize the atoms in exactly the same level each time.

4.4.3 Demonstration of Rabi oscillations

The microwaves shine and we detect the fluorescence of the atoms using the trap laser in the $F = 2$ level by a CCD camera or by the photodiode. In the control system we change the microwave duration from a couple of μs to 2 ms and we get a clear Rabi oscillation with a high Rabi frequency ($5{\times}10^4 s^{-1}$). Figure 4.7 shows the result, blue squares are experimental data points and we compare the experimental data with a theoretical fit (red curve) as described by [63]

$$\rho_{ee} = \frac{A}{2(1+2\xi^2)}[1 - (\cos(\Omega' t) + \frac{3\xi}{\sqrt{(4-\xi^2)}}\sin(\Omega' t))\exp(-3\gamma t/2)], \qquad (4.3)$$

where A is the amplitude, $\xi = \frac{\gamma}{\Omega}$, Ω is the Rabi frequency and $\Omega' = \Omega\sqrt{1-\xi^2/4}$ and γ is the decoherence rate. Since all the lasers during the broadcasting of

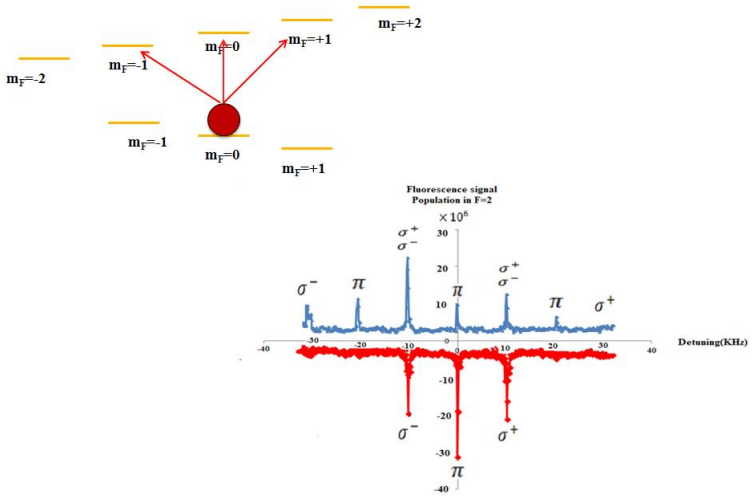

Figure 4.6: Demonstration of Zeeman pumping into the $|F = 1, m = 0\rangle$ dark state. The red (blue) trace is the result with (without) the pi polarized Zeeman pumping beam.

the microwaves are off, then our first guess for the existing decoherence was the leakage of intense beams and consequently spontaneous emissions damp the oscillations. Therefore, we installed mechanical shutters for all paths. Decreasing only the intensity of trap light (which is the most intense one) by a factor of 2, we could see a small changes in the oscillations damping before adding the shutters. We verified the existing decoherence is not due to the photon scattering, instead it seems to be due to the nonuniform illumination of microwaves. The oscillations have improve since this initial demonstration and we obtain now better oscillations as will be shown in the next chapter.

4.5 Zeroing B

This section describes the measurement for zeroing the static $\vec{B}$ in the center of the cell where the atoms are confined. We do this to have a clear understanding of the magnetic field that we have for the experiments. We use the atoms as scalar magnetometers to measure the field.
The bias (static) field in our system is created by a set of x, y and z Helmholtz coils (see Section 2.4.3). The current is injected to them using three different power supplies. Figure 4.8 shows a designed monitoring box connected to the voltmeter to read the voltage and consequently the current we send to the each coil. We added a potentiometer to direct part of the current to a dummy load to fine tune the current we send into the coils. In the experiment, first we kept fix the current in the $\hat{y}$ and $\hat{z}$ coils and we only change the current in the $\hat{x}$ coils from 0 to almost 400 mA. In parallel, we take the microwave spectroscopy and only focus on one particular peak in the left hand $|F = 1, m_F = -1\rangle \rightarrow |F = 2, m_F = -2\rangle$ transition (first peak from the left side in Fig 4.9) which corresponds to the σ^- microwave polarization. The result is a shift in the frequency of the peak in the spectrum due to the magnetic field changes. We

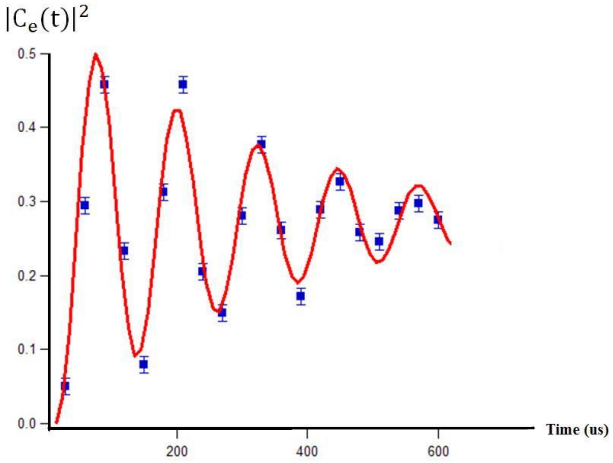

Figure 4.7: Demonstration of the Rabi oscillations for the clock transition. Blue points are experimental data and the red line correspond to the fit.

immediately translate this frequency change to the magnetic field using the first order Zeeman shift. Linear Zeeman shift for a level is $\Delta\vec{E} = m_F g_F \mu_B . \Delta\vec{B}$. The energy shift for the transition between $|F = 1, m = -1\rangle$ and $|F = 2, m = -2\rangle$ (Fig 4.9) is written by

$$\begin{aligned} \frac{\Delta E_T}{h} &= \frac{1}{h}\left[E(m=-2) - E(m=-1)\right] \\ &= \nu_{HFS} + 2.1(MHz/G)B \end{aligned} \tag{4.4}$$

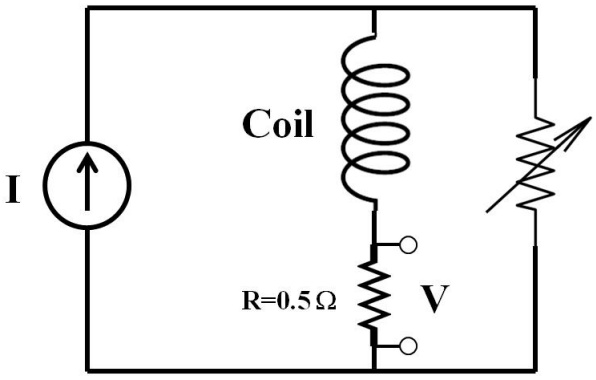

Figure 4.8: Monitoring box used for each coil to read the voltage (current) that goes directly in the $\hat{x}$, $\hat{y}$ and $\hat{z}$ coils.

Since our magnetometer is the scalar one, we have $B = \sqrt{B_x^2 + B_y^2 + B_z^2}$. A fit (solid blue line in Fig 4.10) on equation $B = \sqrt{d_j(I_j - I_{0j})^2 + c_j}$ is used where $j = x, y$ and z matches very well with the experimental data. According to

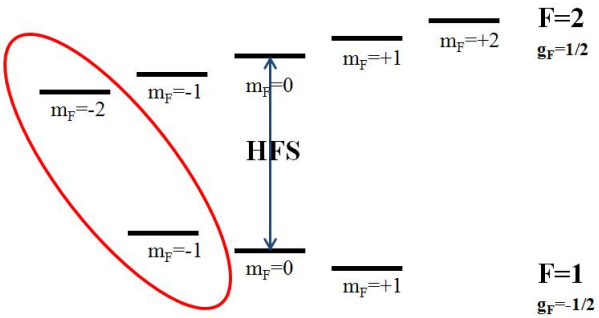

Figure 4.9: The particular transition used to zero the field in each coordinate.

Fig 4.10 (a), by scanning the current in the first pair of the coils, a curve appears with a minimum that the fit determines the corresponding current I_{0x}=194 mA for this minimum which eliminates B_x. Here we have $B_x^2 = d_x(I_x - I_{0x})^2$ and $c_x = B_{y0}^2 + B_{z0}^2$. We continue and fix the I_{0x} at 194 mA and start to scan the current of the second pair ($\hat{y}$). The second curve (Fig 4.10 (b)) shows another local minimum at I_{0y}=120 mA to zero the B_y. So far we could kill the B_x and B_y terms in $B = \sqrt{B_x^2 + B_y^2 + B_z^2}$ expression. In the last step we do the same for the third pair in the $\hat{z}$ direction and it gives an absolute value for the current (I_{0z}=161 mA) or the voltage to zero the $\vec{B}$ (See Fig 4.10 (c)).
Igor pro software gives $d_x = 0.71671 \pm 0.0103(\frac{mG}{mA})^2, c_x = 142150 \pm 172(mG)^2$, $d_y = 1.1513 \pm 0.0159(\frac{mG}{mA})^2, c_y = 136250 \pm 261(mG)^2$ and $d_z = 4.8758 \pm 0.013(\frac{mG}{mA})^2$ which are fix numbers one can read to zero the field. One of the supplies (Agilent E3614A) has this advantage to be remotely controlled via sending a voltage between 0-1 Volts through the control system and that controls the bias field in the z (vertical) axis that we can set starting from this zero field condition.

4.6 Improvement of fluorescence detection

In Section 2.6 we describe our imaging system. The fluorescence reaches a photodiode that is connected to National Instruments acquisition card (NI-USB 6289). In our daily work, for example we need to take an atomic spectrum for the magnetometry (measuring B using atoms). The microwave spectrum had a limited signal to noise ratio (Fig 4.11 (a)). Part of the reason was due to the electromagnetic noise in the lab. For instance, we found out by turning off the monitoring TV beside NI card which had a high current source, we could clearly see an enhancement in our signal. The main source of the noise in our signal was from the scattered lights of trap and repumper lasers in addition to the electronic noise. We correct the LabView codes in our control system and also in detection part. In the control system program we added four flashes to save the atom numbers P_1, P_2, P_3 and P_4. In the first flash only the trap laser is on and the fluorescence is proportional to the number of atoms that were transferred to $F = 2$ (P_1). During the second flash both trap and repumper laser are on, so one can get the population in $F = 1$ and $F = 2$ hyperfine levels (P_2). With

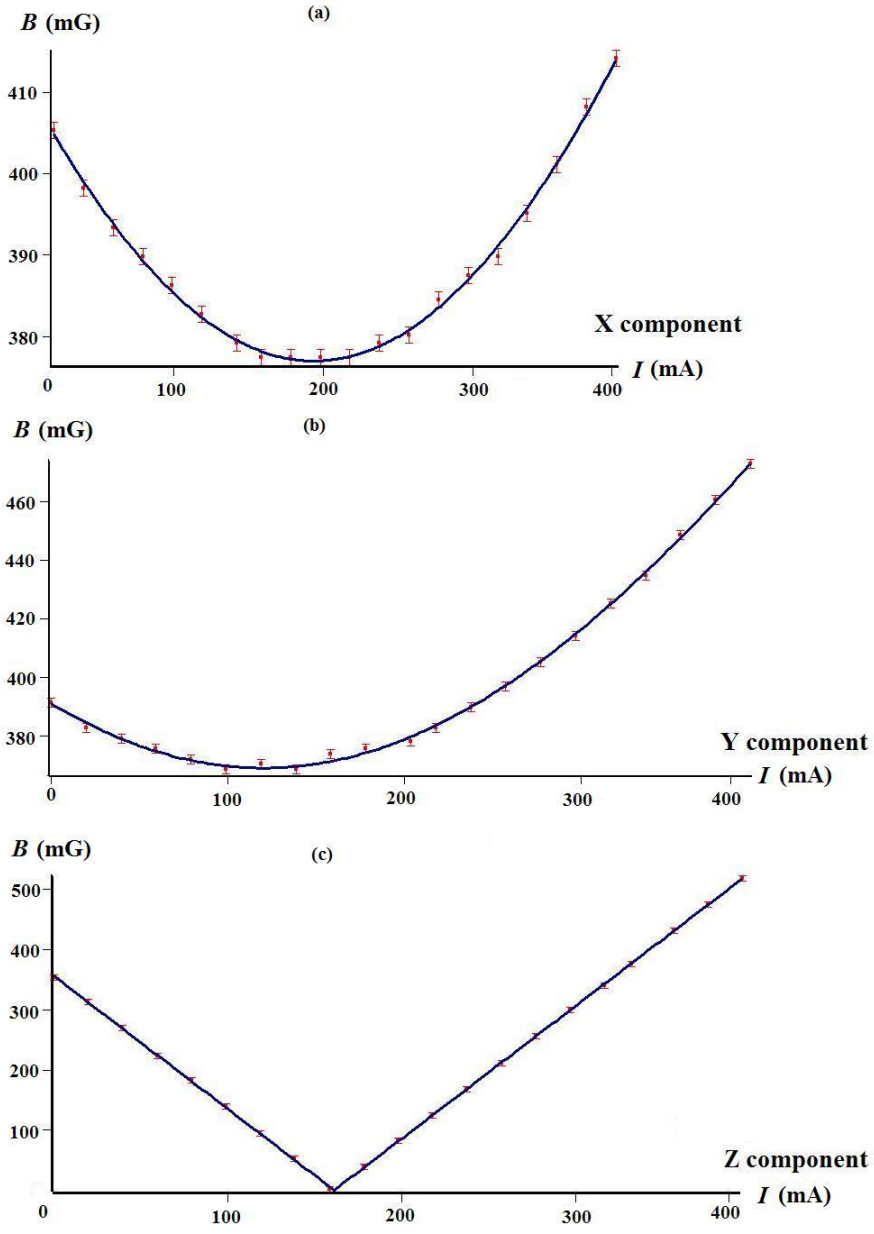

Figure 4.10: Results of the magnetometry using the atoms. Experimental data (red points) determines the zero for the B_x (a), B_y (b) and B_z (c). A blue solid line is a fit as explained in the text.

this signal we can normalize the P_1 signal. During the third flash, the repumper laser is off and we turn on the depumper laser in advance to optically pump the atoms to $F = 1$. Then in this case we record only the fluorescence coming from the scattered light of trap laser (P_3). Last flash applies when the repumper laser is on and the trap is off. Since the trap laser is off, there are no atoms anymore to transfer and we only see the noise contribution (scattered light) of repumper laser (P_4). Therefore, in the screen we see four hills corresponding to the mentioned populations. During the detection, the only consideration is to check the heights of the signals in the screen. We see that the quality of the signal depends on the quality of the trap lock, and playing with the gain to get a more stable lock gives lower noise. It is also important to check the position of photo diode every now and then to maximize the measured fluorescence. The fraction of atoms in $F = 2$ properly normalized and corrected for background light can be calculated from $(P_1 - P_3)/(P_2 - P_3 - P_4)$. This modification gives us the fraction population in $F = 2$ without the effects from the scattered lights and we could see a clear enhancement in our signal to noise ratio (Fig 4.11 (b)). The noise we observe in our measurements is still limited by the fluorescence detection to about 0.1. This could be improved in the future with a region in the system dedicated to only detection with high collection efficiency.

4.7 Results of Ramsey method for the clock transition

In a Ramsey type interferometer, the population of the atoms in the excited state is described by [64]

$$|c_e(t)|^2 = \left(\frac{2\Omega}{\Omega'}\right)^2 \sin^2(\frac{\Omega'\tau}{2}) \times \left[\cos(\frac{\Omega'\tau}{2})\cos(\frac{\delta T}{2}) - \frac{\delta}{\Omega'}\sin(\frac{\Omega'\tau}{2})\sin(\frac{\delta T}{2})\right] \tag{4.5}$$

where $\Omega' = \sqrt{\Omega^2 + \delta^2}$ and δ is detuning. τ is the duration of pulses and T is the evolution time in the darkness.

The experimental setup for Ramsey type interferometry uses the same microwave system illustrated in Section 4.4. According to the procedure in Section 4.1 when we close the interferometer between $|l\rangle \leftrightarrow |u\rangle$, we detect the fractional population in $F = 2$ using fluorescence imaging. We set the microwave frequency resonantly on clock transition. We initialize the atoms in $|l\rangle$ as explained before. We apply a first $\pi/2$ pulse with a duration of τ. We let the atoms to evolve with the time T. The second $\pi/2$ pulse closes the interferometer. Figure 4.12 (a) shows Ramsey fringes of the clock transition with τ=75 μs and T =750 μs. We get narrower peaks by increasing T as in Fig 4.12 (b) that shows a zoom of the spectrum with τ=20 μs and T =9.96 ms.
The width of the fringes is given by $\nu = 1/2T$ and corresponds to 50 Hz in our case (see Fig 4.12 (b)). Given our signal to noise ratio ($S/N = 10$), we currently have a precision of about 5 Hz using this method. There are the slow and fast oscillations in Fig 4.12 (a) where the slow oscillations (the envelope) corresponds to the Sinc function $\left(\frac{2\Omega}{\Omega'}\right)^2 \sin^2(\frac{\Omega'\tau}{2})$ in Eq 4.5 and the fast oscillations relates

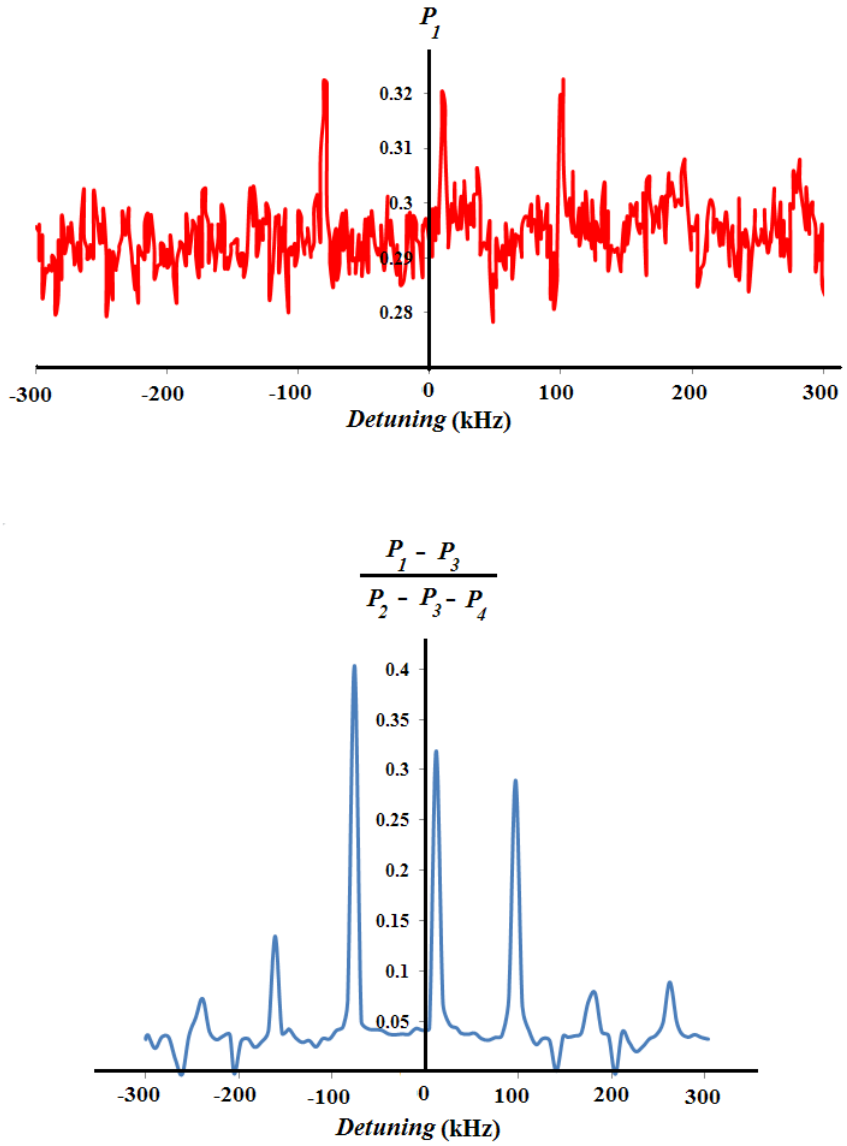

Figure 4.11: Microwave spectrum with a) only the trap fluorescence and b) with background suppression and correct normalization.

to the term that is defined by $\cos(\frac{\delta T}{2})$. We found a noise floor (the pedestal of microwave) in our experiment while using the synthesizer (Giga Tronics, Model 1018). We fixed that problem by replacing it with the PLL synthesizer (model: EVALADF4350-EB2Z). Figure 4.12 are the preliminary results of interferometric fringes and the visibilities are not the best, we show the better results later on in the next chapter.

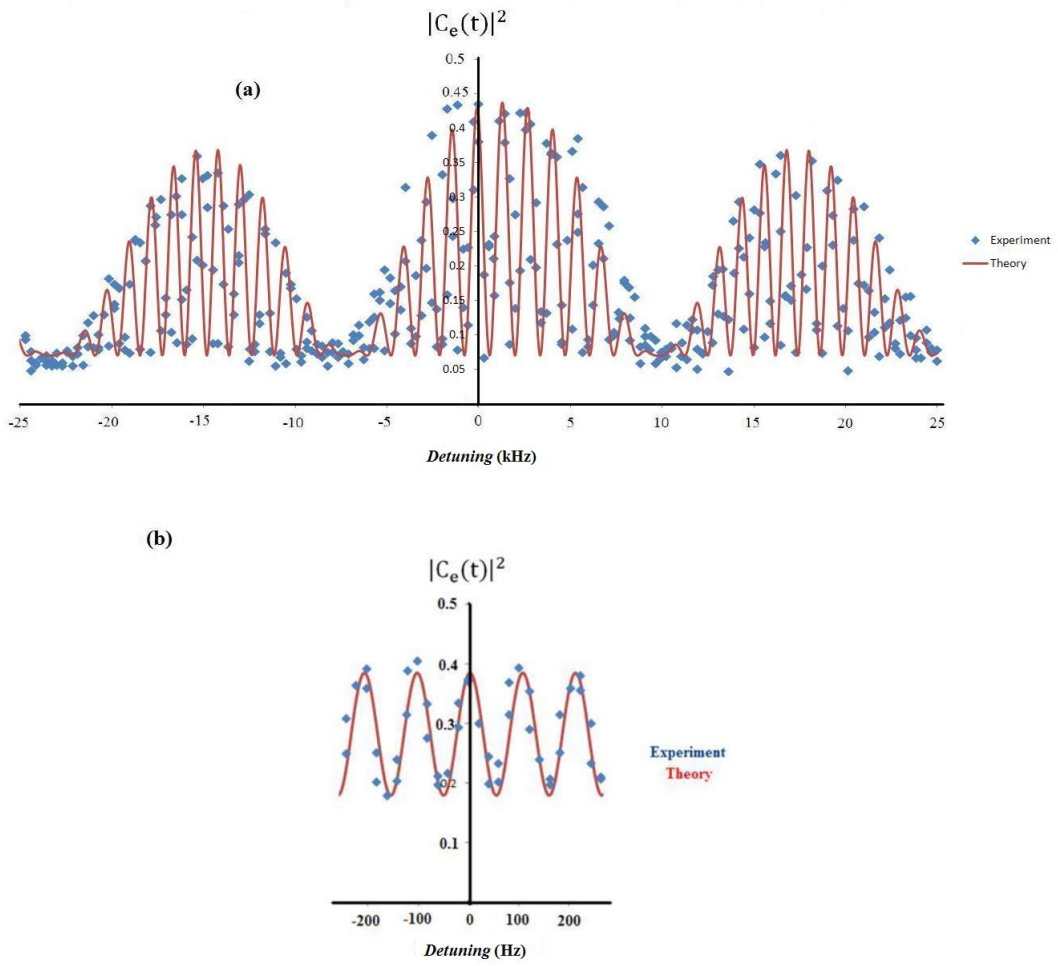

Figure 4.12: Demonstration of Ramsey interferometry for the clock transition, (a) with a $\pi/2$ pulse of duration τ=75 μs and a time between pulses of T =750 μs, (b) shows a zoom on the central part of the fringes to show the oscillations with τ=20 μs and T =9.96 ms.

4.8 Conclusion

In order to do atom interferometry, we need to consider some experimental requirements. After capturing (in the MOT) and further cooling of the atoms

by optical molasses, we showed that we are able to optically pump them to a particular Zeeman sublevel. Zeroing the magnetic field at the position of the atoms has been demonstrated. Our detection system based on fractional population in $F = 2$ is also described and finally the first experimental Ramsey fringes for the case of the clock transition were observed. The width of the peaks depends on the time T between pulses. In the next chapter, we discuss the two photon transition between $|F = 1, m = -1\rangle \rightarrow |F = 2, m = 1\rangle$ to then mix the two transitions in a dual interferometer.

Chapter 5

Two Photon Transition

5.1 Introduction

We mentioned in Chapter 1 that we are interested to do atomic interferometry using magnetic sensitive states. Two of these states are shown in red in Fig 1.1 and corresponds to the transition $|F = 1, m = -1\rangle \rightarrow |F = 2, m = 1\rangle$. The other one can be the $|F = 1, m = 1\rangle \rightarrow |F = 2, m = -1\rangle$ transition, but this one has the minimum magnetic sensitivity point at negative magnetic field values. In this chapter we characterize the two photon transition.

5.2 Preparation of two photon transition

To characterize the two photon transition, we first excited the transition $|F = 1, m = 0\rangle \rightarrow |F = 2, m = 2\rangle$. Figure 5.1 shows these two levels, along with the required microwaves and RF signals. We applied a bias field and this shifts the Zeeman sublevels. Again here we start all the atoms in $|l\rangle$. The RF frequency would be hundreds of kHz up to few of MHz depending on the applied bias field. We use a magnetic field of 385 mG and using MW spectroscopy we verified that the separation between the Zeeman sublevels is about 270 kHz. The RF signal is detuned from Zeeman transitions by Δ=70 kHz. For the MW signal we use a horn and for the RF we use a homemade antenna [65].

5.2.1 RF antenna

We designed an RF antenna which is a coil of 33 turns of copper wires around a plastic structure with a radius of 5 cm [65]. We added 16 capacitors in parallel and we are able to vary the capacitance in the LC circuit by jumpers (switches) on top of the antenna (see Fig 5.2). By making the antenna resonant we enhance its emission. A BNC connector is made to receive the signal from the synthesizer. We made three antennas, each of them are resonant in a particular frequency range. Table 5.1 shows the resonant frequencies generated by antenna number 3. We verified that the antenna has approximately 35 kHz bandwidth. By adding more capacitance in the LC circuit, the resonant frequency decreases since $\omega_c = 1/\sqrt{LC}$.

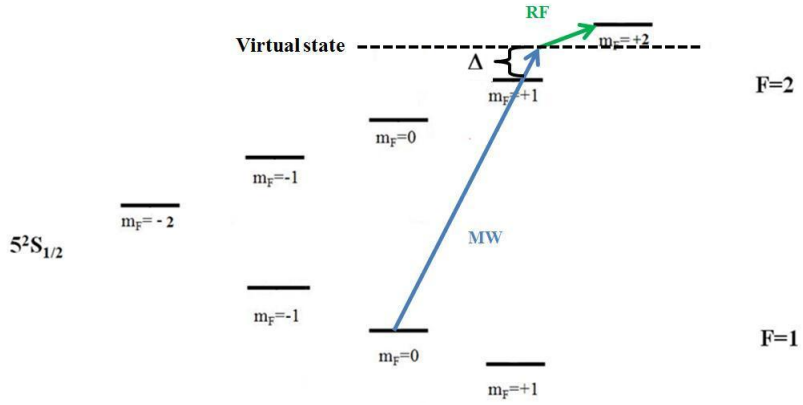

Figure 5.1: Two photon transition of $|F = 1, m = 0\rangle$ to $|F = 2, m = 2\rangle$ in ^{87}Rb. In presence of 385 mG the degeneracy is lifted. A MW and RF signals are used to drive the two photon transition. $\Delta = 50kHz$ is the detuning.

Jumper Number(s) ON	**Resonant Frequency (MHz) ± 0.01**
1	2.41
1-2	2.379
1-3	2.322
1-4	2.234
4,5	2.17
1-5	2.088
1-6	1.958
5,11,12,13	1.946
1-7	1.832
2,3,4,5,6,7,9	1.82
1,2,4,5,6,7,8	1.75
1-8	1.745
1-9	1.725
4-8,14,15	1.722
1-10	1.71
1-11	1.675
1-12	1.607
1-13	1.582
1-14	1.562
1-15	1.54
1-16	1.052

Table 5.1: Resonant frequencies of RF antenna number 3.

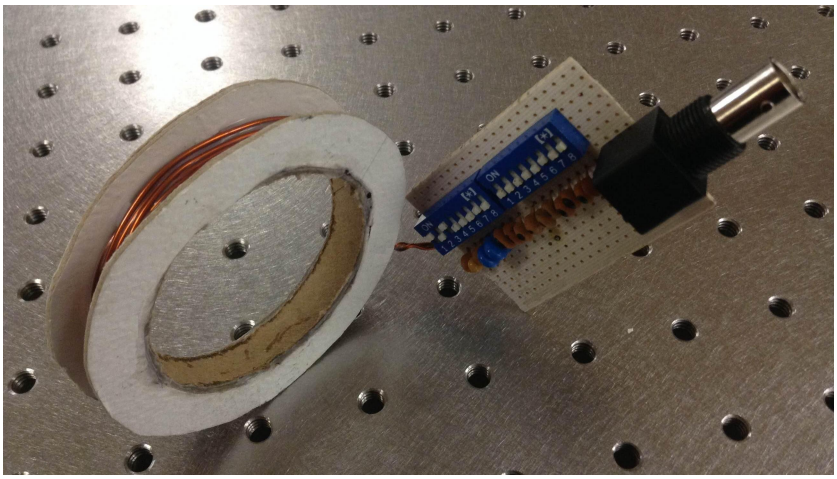

Figure 5.2: An image of the RF antenna.

In order to test the functionality of the antenna we apply a 385 mG field (perpendicular to the optical table) which gives 270 kHz linear Zeeman shift on the $|F = 1, m = 0\rangle \rightarrow |l\rangle$ to $|F = 2, m = 1\rangle \rightarrow |p\rangle$ transition. After successful Zeeman pumping to the dark state $|l\rangle$, we send an RF signal to transfer the population to $|F = 1, m = 1\rangle$ and then immediately a MW signal sends the population to $F = 2$ state for the fluorescence detection from the cycling transition. The MW signal is resonant with$|F = 1, m = 1\rangle \rightarrow |F = 2, m = 1\rangle$. The RF antenna is connected to a synthesizer (Rigol DG1022A) and the Burst feature is used to control the duration of RF pulse by defining the number of cycles in a burst. By changing the duration for the MW signal and varying the number of cycles in the RF synthesizer, the Rabi oscillation are observed (Fig 5.3). The oscillations in the experimental data (black points and curve) have an M shape and this is due to the fact that the RF pulse couples the three Zeeman sublevels of $F = 1$ simultaneously. The 12 kHz oscillation frequency measured is twice the Rabi frequency of hyperfine $|l\rangle \rightarrow |p\rangle$ transitions. The Rabi frequency of RF antenna can be decreased by lowering the intensity of its synthesizer or installing antenna far from the atoms. The fit was done using Eq 4.3 from where we can extract the oscillation frequency and from there obtaining the Zeeman Rabi frequency. We need the RF antenna to couple the two photon $|F = 1, m = 0\rangle \longrightarrow |F = 2, m = 2\rangle$ transition. Then we need a circular (σ_+) RF transition shown in Fig 5.1 (green arrow). It is so complicated to design a helicoil RF antenna to give us pure circular polarizations. So we installed the coil (RF antenna) close to the cell somehow that the B_{RF} is perpendicular to the z axes. This produces the linear polarizations which have the components of σ_+ and σ_- as well. We tested the functionality of the antenna between $F = 1$ Zeeman sublevels and we obtained the Rabi frequency of the $|F = 1, m = 0\rangle \longrightarrow |F = 1, m = 1\rangle$ transition. The Rabi frequency of interest $|F = 2, m = 0\rangle \longrightarrow |F = 2, m = 1\rangle$ which is the green arrow shown in Fig 5.1 will be different with the tested one and it can be calculated from the $3j$ symbol (Clebsch-Gordan coefficient).

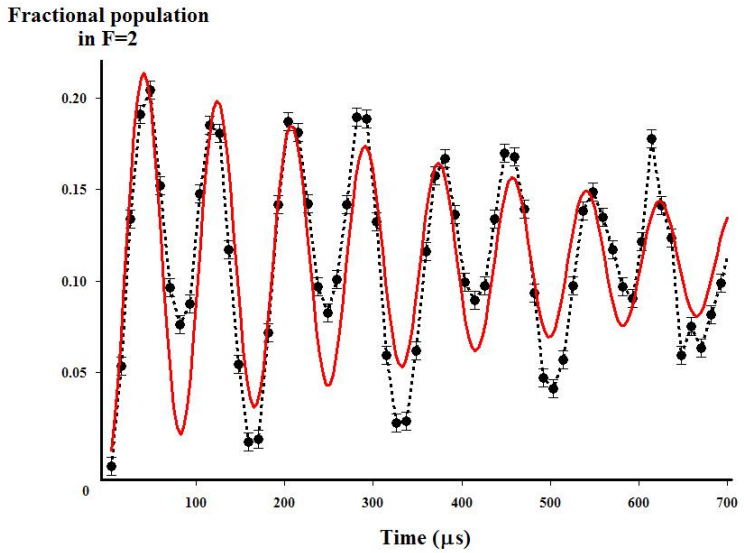

Figure 5.3: Rabi oscillations of Zeeman sublevels in $F = 1$ using an RF antenna. The data points are joined by a black dashed line and the red solid curve is a fit. The fit gives 12 kHz Rabi frequency and the duration for a π pulse is 41 us.

5.2.2 Demonstration of the $|F = 1, m = 0\rangle \rightarrow |F = 2, m = 2\rangle$ transition

Once the functionality of the RF antenna is checked, the plan is to get the signal of two photon transition that shown in Fig 5.1 by the following steps:

1. Initializing the atoms in presence of 385 mG at $|F = 1, m = 0\rangle$.
2. Shine simultaneously the MW and RF fields to transfer the atoms to the $|F = 2, m = 2\rangle$ level.
3. Detection using the fluorescence imaging technique in $F = 2$.

We clearly see the signal goes away when either MW or RF are switched off using the control system. In order to estimate the Rabi frequency of the two photon transition, we swept the duration of MW and RF pulses manually. In the case of RF signal, changing the number of cycles determine radiation time thanks to the Burst feature in its synthesizer. The Rabi frequency of the two photon transition is described by [60]

$$\Omega_2 = \frac{\Omega_{MW}\Omega_{RF}}{2\Delta} \tag{5.1}$$

where Δ is detuning as shown in Fig 5.1. The experimental results are shown in Fig 5.4 (a), (b) and (c) corresponding to 24, 50 and 100 kHz respectively. Changing the detuning of the transition requires the new values of resonant frequencies for both MW and RF signals. The curves give the correct detuning scaling as given by Eq 5.1. The measured Rabi frequencies for Δ=24 kHz, Δ=50 kHz and Δ=100 kHz are 2$\pm$0.07 kHz, 1$\pm$0.01 kHz and 400$\pm$25 Hz respectively.

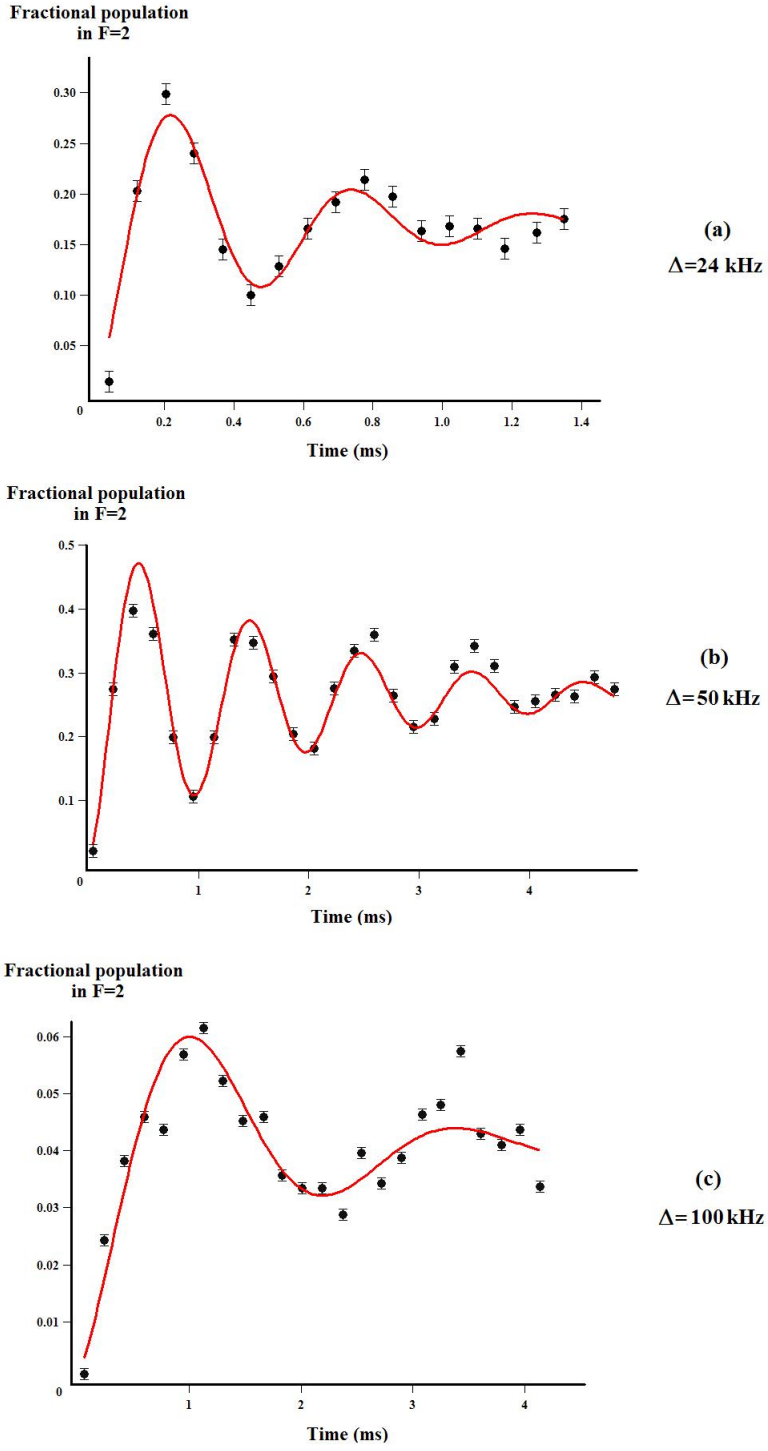

Figure 5.4: Rabi oscillations for two photon transition of $|F = 1, m = 0\rangle$ to $|F = 2, m = +2\rangle$ with (a) Δ=24 kHz, (b) Δ=50 kHz and (c) Δ=100 kHz, the black points are experimental data and solid red curves are the fits which give the Rabi frequencies of $\Omega_{(a)}$=1920$\pm$70 Hz, $\Omega_{(b)}$=990$\pm$10 Hz and $\Omega_{(c)}$=420$\pm$25 Hz.

We use the above results to demonstrate we can drive a two photon transition in the simplest case, and we are now ready to go to the transition of interest.

5.3 Coupling magnetic sensitive states $|F = 1, m = -1\rangle \rightarrow |m\rangle$ to $|F = 2, m = 1\rangle \rightarrow |p\rangle$ (desired transition) at low field

The same discussed initialization procedure is considered for $|m\rangle \rightarrow |p\rangle$.

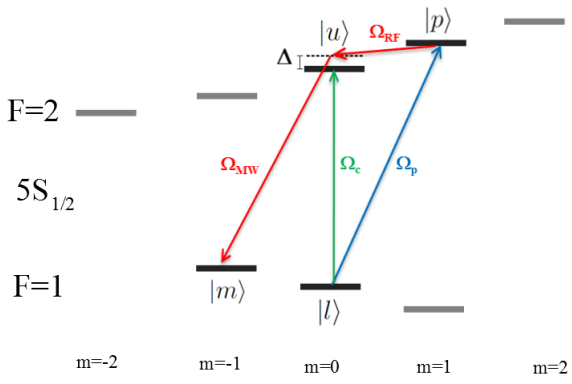

Figure 5.5: Two photon transition of magnetic sensitive states $|p\rangle$ to $|m\rangle$ in ^{87}Rb. In presence of 385 mG the degeneracy is lifted. Starting all atoms in $|l\rangle$, a π pulse sends all atoms to $|p\rangle$. The Ω_{MW} and Ω_{RF} drive the two photon. Δ is detuning.

We initialize all atoms in $|l\rangle$, a π pulse generated using a separated synthesizer (Novatech 409B) for the RF, sends all atoms to $|p\rangle$. This RF signal mixes with the microwave signal (6.8 GHz) in the single sideband modulator which discussed in the previous chapter that generates the preparation microwave pulse. The Ω_{MW} and Ω_{RF} drive the two photon transition as shown in Fig 5.5. The RF synthesizer has a limit of 1 V_{pp} for the output signals so we require to use an amplifier (Mini-Circuits ZFL-500+) to reach a power of 2.24 V_{pp}. Figure 5.6 shows the Ω_{MW} is driven by mixing a low frequency synthesizer (SRS DS345) with the single sideband modulator (SSB4080A) and Ω_{RF} is directly produced by an arbitrary waveform generator (RIGOL DG5071). The sum of the frequencies $(\Omega_{MW} + \Omega_{RF})$ will be resonant with the $|m\rangle \longrightarrow |p\rangle$ transition. A switch (Mini-Circuits ZFSWA-2-46) receives the two RF signals from two low frequency synthesizers (Novatech 409B and SRS DS345). Using an RF switch, a particular low frequency synthesizer can be selected to be combined on the single sideband modulator.

We consider all the possible transitions such as single photon and two photons when we shine the MW and RF signals simultaneously. We fix the RF frequency and sweep the MW signal. There are cases that ν_m (MW frequency) is exactly resonant with ν_a (atomic frequency), in this case $\nu_a = \nu_m = \nu_{HFS} + CB + DB^2$ where C and D are linear and quadratic Zeeman coefficients (see

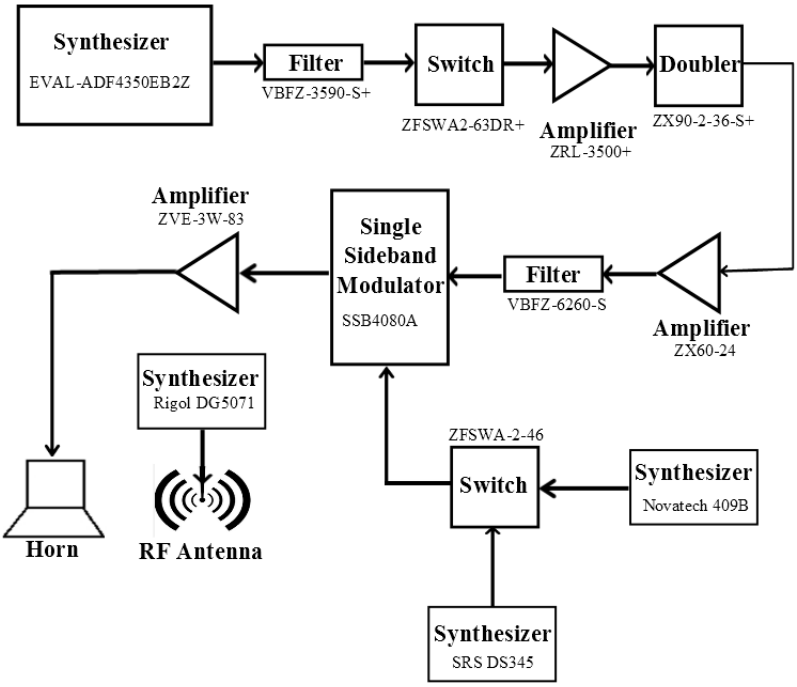

Figure 5.6: A block diagram of MW and RF setup for coupling $|m\rangle \rightarrow |p\rangle$ transition.

Appendix C). The other groups of transitions are two photon transitions $\nu_a = \nu_m \pm \nu_{RF}$. In these transitions, the difference for the m quantum number can be 1 and 2. There are 18 possible transitions for the case of Δm=1 and 8 possible transitions for the case of Δm=2. Figure 5.7 shows these transitions once we consider a fix frequency for the RF signal at 2.17 MHz and sweep the MW. Each group of transitions are demonstrated with a color code. For example we zoom at 2.95 G; our desired transition (black line) is surrounded with T_1...T_6 (see inset in Fig 5.7). The closest transitions in this case are T_1 and T_2. T_1 belongs to the two photon excitation of the clock $|l\rangle \longrightarrow |u\rangle$ and T_2 is the two photon of $|F = 1, m = 1\rangle$ to $|F = 2, m = -1\rangle$ transition. T_1 is the most dangerous one as depicted in the inset of Fig 5.7 is separated by 10 kHz from $|m\rangle \longrightarrow |p\rangle$ (black line) at 2.95 G. The anti peak ($|m\rangle \rightarrow |p\rangle$) and the peak ($|l\rangle \rightarrow |u\rangle$) in Fig 5.8 show exactly the same black and red transitions in Fig 5.7. In contrast to the case of low magnetic field, one can differentiate spectrally the desired two photon $|p\rangle \longrightarrow |m\rangle$ transition (red trace in Fig 5.8) and undesired T_1 transition (blue trace in Fig 5.8) very well thanks to the quadratic Zeeman shift. In the blue lower trace of Fig 5.8, we did not apply the preparation pulse between $|l\rangle$ to $|p\rangle$ so that all the atoms are in $|l\rangle$ and we drive only the two photon of the clock transition while in the red upper trace the preparation signal is on and tuned to be a π pulse. It means that all the atoms are initially in $|p\rangle$ and we drive the $|p\rangle$ to $|m\rangle$ two photon transition. The height of the peaks depends on the pulse duration that is shorter than a π pulse in this case. There is an small peak in the lower blue trace of Fig 5.8 at -4.5 kHz coming from the residual population

in the $|F = 1, m = -1\rangle$ level after optical pumping. According to Eq 5.5 these two transitions at 3.2 G are separated by 10.4 kHz and this is 21 times larger than their width of 500 Hz, with this last one determined by the pulse duration of 1 ms. The width gives the Rabi frequency of the transition and it can be translated into the duration of the pulse. Although the undesired transition is separated by 10.4 kHz away from our wanted two photon transition, it gives a negligible population transfer of at most 0.3 %. This is derived by substituting the Ω_2=0.5 kHz and detuning δ=10.4 kHz in $\Omega_2^2/[\Omega_2^2 + \delta^2]$ which comes from Eq 4.2. According to this expression, the undesired transition at 385 mG has the 20 % transfer which is not negligible at all.

We do not need to be worried about T_2 transition in the inset of Fig 5.7 since there is no population in either $|F = 1, m = 1\rangle$ or $|F = 2, m = -1\rangle$ states. T_3 and T_4 are the single photon transitions which are separated 50 kHz away from the desired transition (black line). Given the 6 kHz Rabi frequency (for the single transitions) and 50 kHz separation from the desired transition (black line), the possibility of excitations by T_3 and T_4 are quite negligible (about 1 % transfer). T_5 and T_6, the other possible two photon transitions which are even further away from our desired one. Considering 0.5 kHz Rabi frequency for the two photon transitions, the excitations by T_5 and T_6 will be quite unlike.

We illustrated in Fig 5.9 the frequencies of two photon transition in different magnetic fields (black data points) which it means that we couple exactly the $|p\rangle$ to $|m\rangle$ states and not for example the two unwanted transitions of $|l\rangle$ to $|u\rangle$ or $|F = 1, m = 1\rangle$ to $|F = 2, m = -1\rangle$. Using Eq C.3 in Appendix C, the red solid curve gives the theoretical expression for this transition given by

$$\nu_2 = (\omega_{HFS}/2\pi)(1 + 2\gamma_2 aB + \frac{3}{8}a^2B^2) \tag{5.2}$$

where $(\omega_{HFS}/2\pi)$ is the hyperfine splitting, B is the magnetic field, $\gamma_2 = (g_I m_e/m_p)/(g_s + g_I m_e/m_p)$, $a = (g_s\mu_B + g_I\mu_N)/(\hbar\omega_{HFS})$, g_s and g_I are the electron orbital and nuclear g-factors, μ_B and μ_N are the Bohr magneton for the electron and nucleus, m_e and m_p are the mass of electron and proton, and the values have been evaluated for ^{87}Rb in Appendix C. The green dashed curve in Fig 5.9 gives the theory fit for the T_1 undesired two photon clock excitation. It is described by

$$\nu_c = (\omega_{HFS}/2\pi)(1 + \frac{1}{2}a^2B^2) \tag{5.3}$$

and the black dashed line in Fig 5.9 is the theory fit for the undesired (T_2) $|F = 1, m = 1\rangle$ to $|F = 2, m = -1\rangle$ transition in the form of

$$\nu_2' = (\omega_{HFS}/2\pi)(1 - 2\gamma_2 aB + \frac{3}{8}a^2B^2) \tag{5.4}$$

The vertical axes in that plot is the frequency of the transition. Figure 5.9 confirms that we couple the correct $|p\rangle \longrightarrow |m\rangle$ two photon transition.
To further check this we coupled the $|p\rangle \longrightarrow |m\rangle$ transition is to change the magnetic field slightly around 3.2 G and taking an spectrum. The dips in Fig 5.10 shows the transitions from $|p\rangle$ to $|m\rangle$ sublevels. Since the field is close to

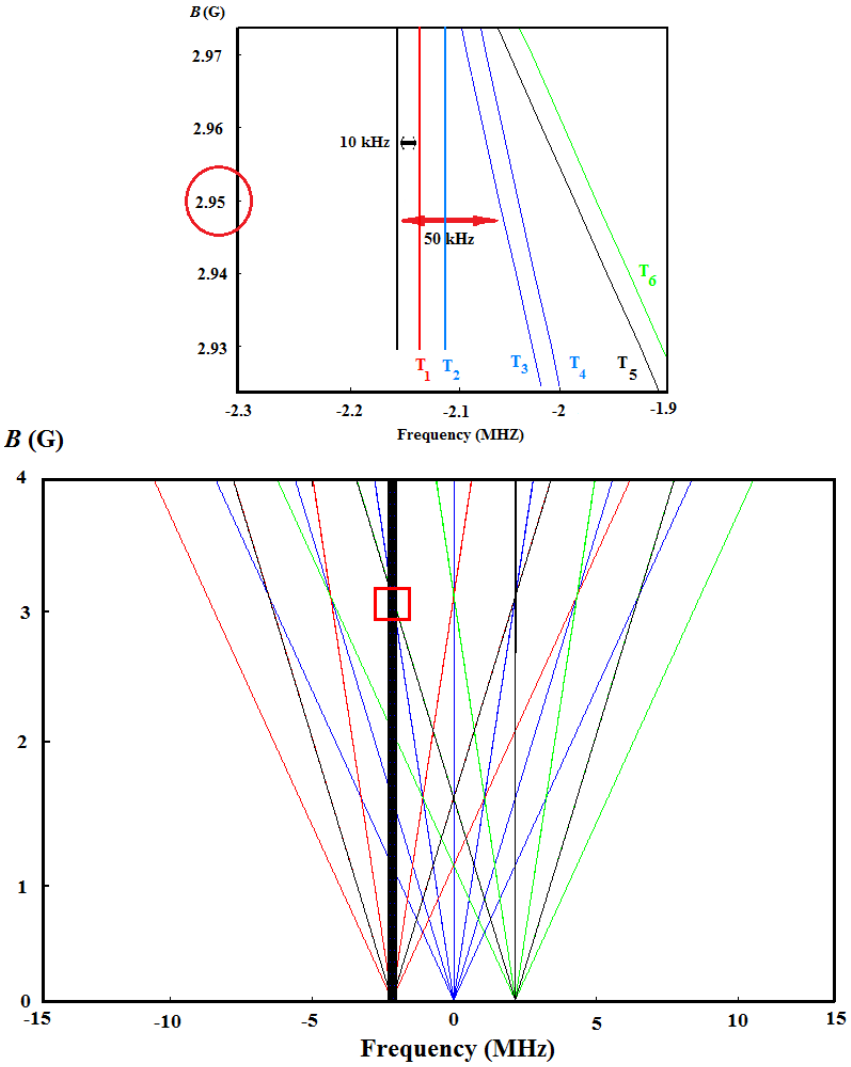

Figure 5.7: Single and two photon transitions for a fixed RF frequency and modulating MW. The thick black line in the center shows the desired two photon $|m\rangle \longrightarrow |p\rangle$ transition. The center blue lines show the single photon transitions. The other groups are the two photon transitions $\nu_a = \nu_m + \nu_{RF}$ (red lines with $\Delta m = 1$) and $\nu_a = \nu_m - \nu_{RF}$ (green lines with $\Delta m = 1$). In these transitions, the difference for the m quantum number can be 2 which is shown by thin black lines. The plot has a zoom in the red square zone (inset) at the field of 2.95 G.

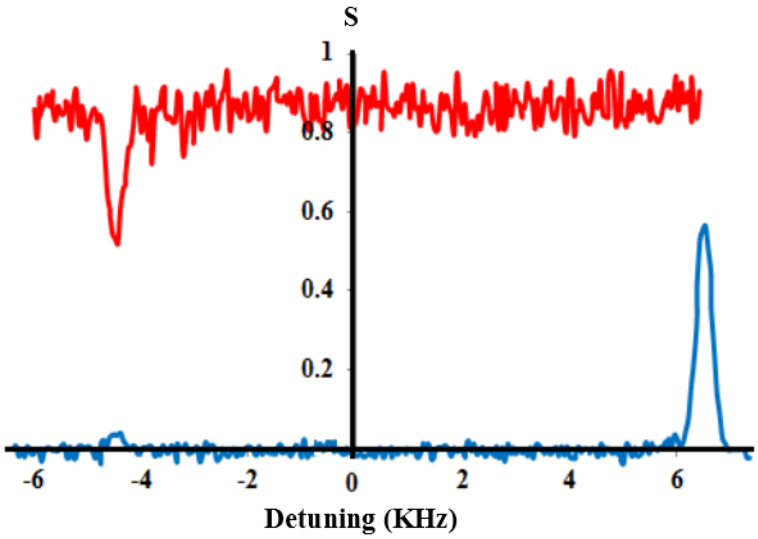

Figure 5.8: Spectrum taken with only the two photon fields on, $|p\rangle \longrightarrow |m\rangle$ transition (higher red trace) and $|l\rangle \longrightarrow |u\rangle$ transition (lower blue trace). The small peak in the lower blue trace comes from the residual population in the $|F = 1, m = -1\rangle$ level after optical pumping.

minimum sensitive point (minimum of parabola in Fig 1.2), the distance among dips is quite small. Each color code in Fig 5.10 belongs to a particular magnetic field.

Equation 5.5 shows the difference of required frequencies for the desired ν_2 ($|m\rangle \longrightarrow |p\rangle$) and undesired ν_c ($|l\rangle \longrightarrow |u\rangle$) two photon transitions which are written based on their Zeeman coefficients: $D_1/2\pi = 575$ Hz/G^2 (Quadratic coefficient for the clock transition), $D_2/2\pi = 431$ Hz/G^2 and $C_2/2\pi = -2785$ Hz/G (quadratic and linear coefficients for the $|m\rangle \rightarrow |p\rangle$ transition respectively)

$$\Delta\nu = \nu_2 - \nu_c = (D_2 - D_1)\ B^2 - C_2\ B \tag{5.5}$$

In such a low field as 385 mG, we must consider ν_c since it is close to ν_2 frequency. The two photon transition (ν_2) and the two photon of clock excitation (ν_c) are separated from each other by 1 kHz (at 385 mG) and any remanent fraction of atoms in $|l\rangle$ can induce undesired two photon transitions of clock excitation. By taking into account the correct duration for a π pulse on the $|l\rangle$ to $|p\rangle$ transition (95 μs corresponds to 5.3 kHz Rabi frequency), we could assure that the mentioned undesired transition will not appear because there is no atom in $F = 1$. Figure 5.11 (a) shows the Rabi oscillations for the desired two photon transition and (b) shows the Rabi oscillations for the undesired two photon excitation of the clock transition due to presence of atoms in $|l\rangle$ level. We did the experiment in Fig 5.11 (a) and (b) with and without preparation pulse Ω_p. The existence of an exact π pulse of Ω_p can produce the population in $|p\rangle$ while the absence of that leaves the atoms in $|l\rangle$ level. This explains why our signal has a positive slope at the beginning in Fig 5.11 (a) and a negative slope for the

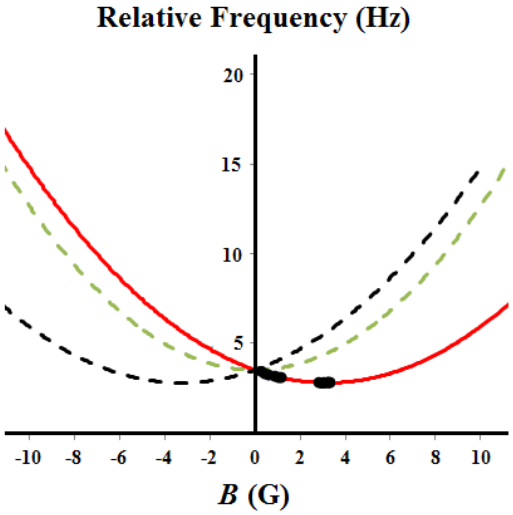

Figure 5.9: Frequencies of two photon transitions vs magnetic field. The black data points shows the measured frequency corresponding to the two photon $|p\rangle \longrightarrow |m\rangle$ transition in particular magnetic field. The red solid curve is the theory in Eq 5.2 for the desired two photon transition. The green and black dashed curves belong to the theory for the two photon of clock excitation and $|F = 1, m = 1\rangle \longrightarrow |F = 2, m = -1\rangle$ transition in Eqs 5.3 and 5.4 respectively.

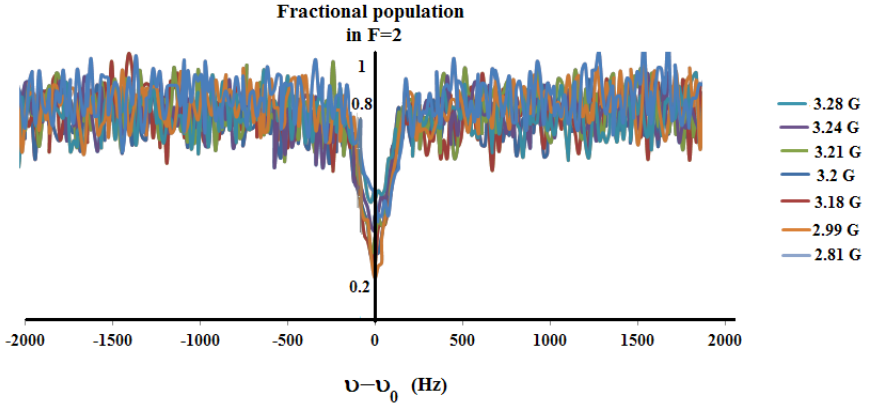

Figure 5.10: Spectroscopy of two photon transitions around 3.2 G. Each color belongs to a particular magnetic field that are shown in the plot. ν_0 is the resonant frequency at 3.2 G.

(b). Working at high fields sends the undesired two photon transition further away from our main $|m\rangle \rightarrow |p\rangle$ two photon transition. For example, at 3.2 G the difference between these two transitions increases by an order of magnitude (10 kHz) compared with 385 mG. The fits in Fig 5.11 (a) and (b) give the Rabi frequencies of 900±5 Hz and 785±5 Hz respectively. Having such a huge detuning (10 kHz) reduces the probability for the excitation of the two photon in clock transition.

5.3.1 Two photon transition at high field

We need to operate the interferometer in a field up to 3.2 G because at that field we get minimum magnetic sensitivity for the transition from $|p\rangle$ to $|m\rangle$. We are able to remotely change the value of the magnetic field controlled with a power supply (Agilent E3614A) whose current is determined by the control system. We observed 16 ms delay to jump from a low field to a high field and vice verse. This is too long for us since the atoms will fall under gravity during that time.

We implemented a circuit to change the current rapidly between two values (Fig 5.12) [65]. The system uses two Insulated-Gate Bipolar Transistors (IGBT) to redirect part of the current from the coil to a dummy load. The two IGBT's have opposite logic so that one is open when the other one is closed, and they are both controlled with a TTL pulse from the control system. In the low TTL condition all the current from the supply (that works in constant current mode) goes through the coils producing the desired bias magnetic field (dashed red in Fig 5.12 (b)). In the high TTL condition we split the current between the path with the coils and that of a dummy resistor (dashed blue in Fig 5.12 (b)). The value of the resistor is adjusted to have the 385 mG used during the preparation stage. We measured the magnetic field as a function of time using microwave spectroscopy on the atoms (Fig 5.13). The magnetic field approaches exponentially the desired value with a 1.5±0.1 ms time constant (1/e). With this circuit we can now do all the preparation at a low field and then quickly ramp the magnetic field to any desired value up to 3.2 G to do the interferometric experiments.

We apply a π preparation pulse Ω_p (blue arrow in Fig 5.5) to send all the atoms from $|l\rangle \longrightarrow |p\rangle$ to characterize the two photon transition. The detuning of 70 kHz is sufficiently large to avoid excitations to the intermediate level. Atomic spectroscopy confirms that the two photon transition works successfully at the high field of 3.2 G. Figure 5.14 is the spectrum that shows an anti-peak since we transfer all the atoms to $F = 1$ and image them in $F = 2$. It's worth mentioning that the detection method does not distinguish between Zeeman sublevels in the upper hyperfine level $F = 2$.

Figure 5.15 shows the Rabi oscillations for the two photon transition at 3.2 G with a typical Rabi frequency of Ω_2=500±2 Hz giving $\pi/2$ pulses of 500 μs. The interference Ramsey fringes for that same transition are shown in Fig 5.16. The width of the fringe is 55 Hz that is related to the time between the pulses as T =9 ms.

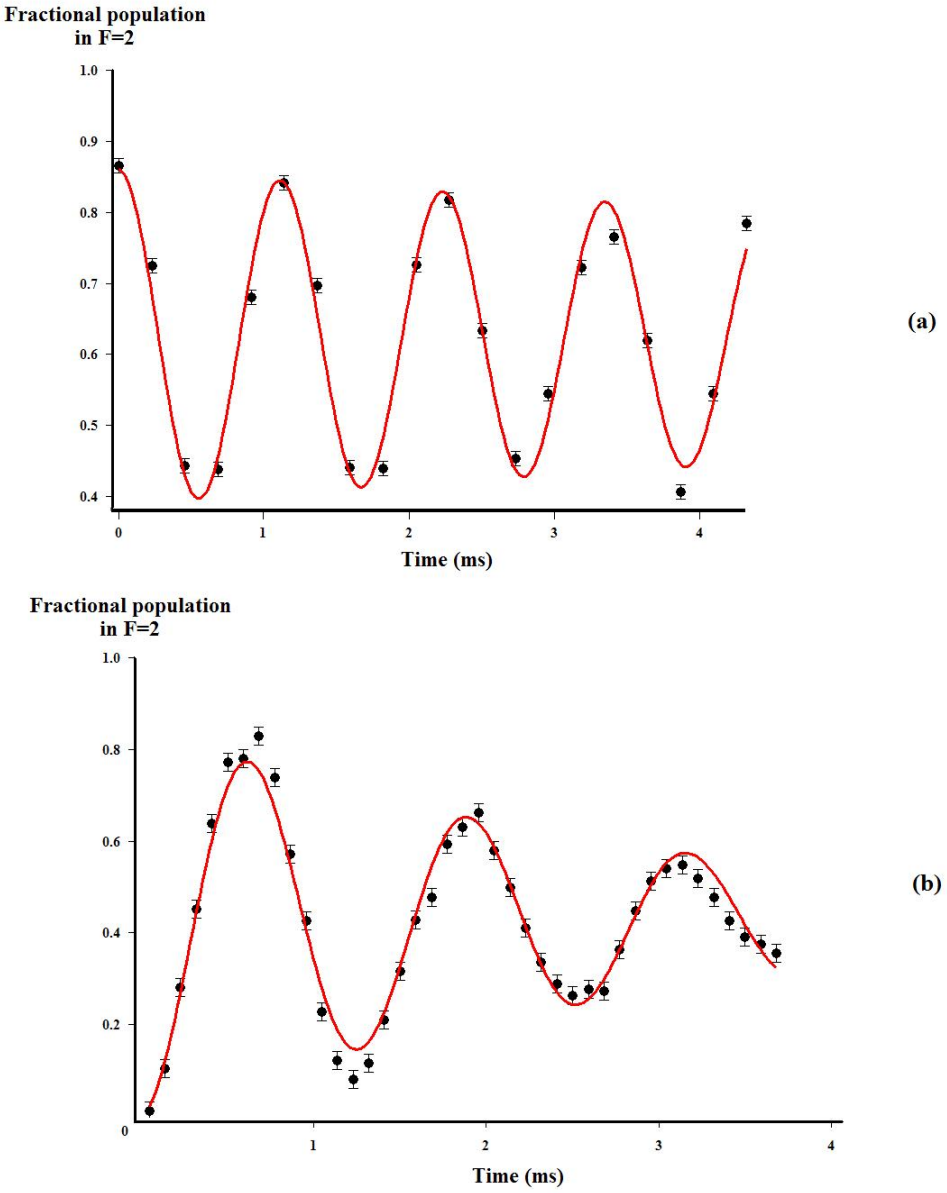

Figure 5.11: Rabi oscillations of (a) the desired two photon transition and (b) the undesired two photon excitation of the clock transition due to presence of atoms in $|l\rangle$ level. The black points are experimental data and solid red curves are fits. The fits give the Rabi frequencies of 900±5 Hz and 785±5 Hz for (a) and (b) respectively.

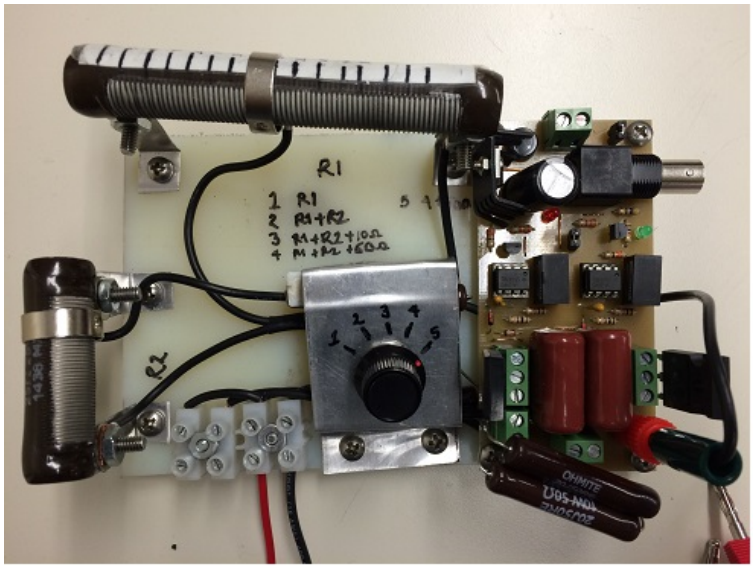

(a)

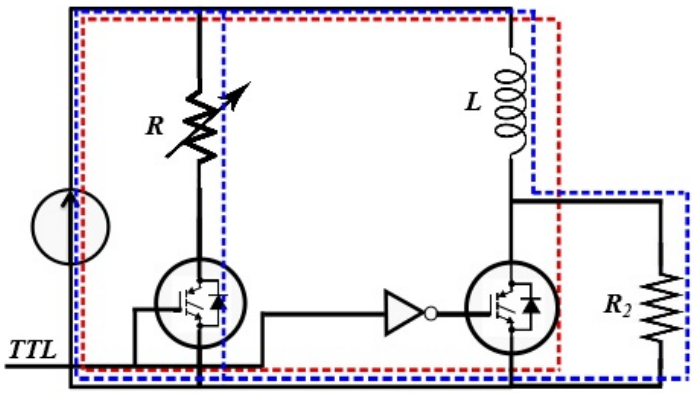

(b)

Figure 5.12: (a) Image of the IGBT circuit. (b) Schematic of the circuit to rapidly switch between the low and high bias magnetic fields. Paths with high (low) TTL are in blue (red).

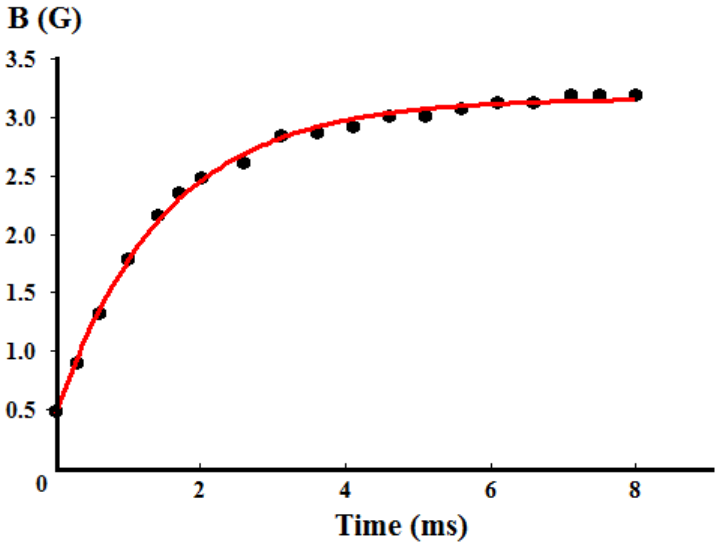

Figure 5.13: Bias magnetic field as a function of time measured with MW spectroscopy on the $|l\rangle$ to $|p\rangle$ transition. In red is an exponential fit to the asymptotic value.

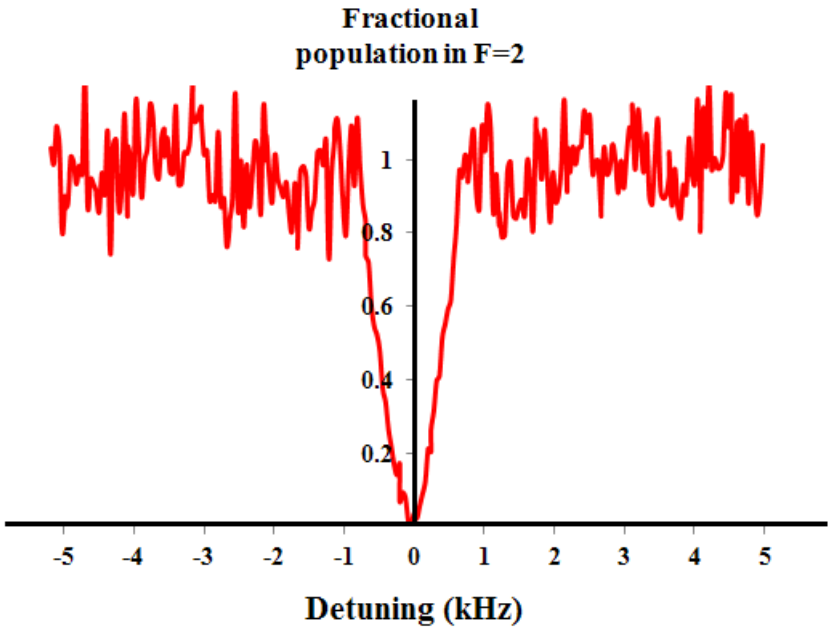

Figure 5.14: MW spectroscopy for two photon transition $|F = 2, m = +1\rangle$ to $|F = 1, m = -1\rangle$ at 3.2 G.

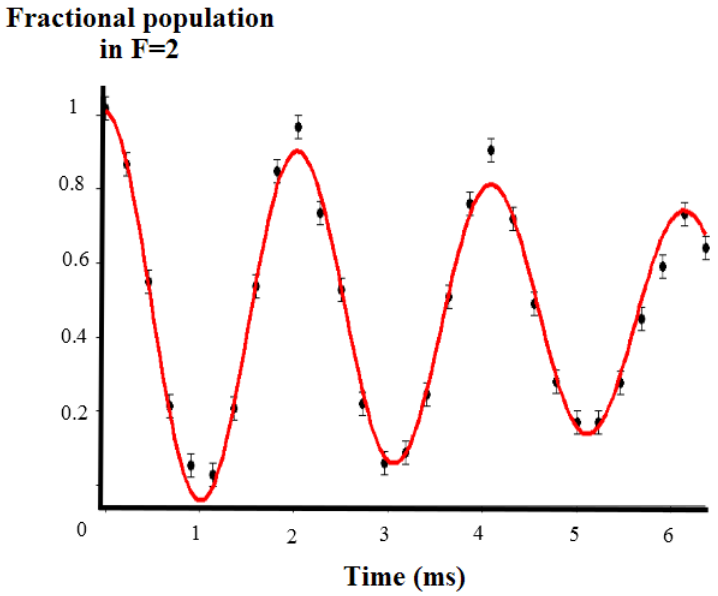

Figure 5.15: Rabi oscillations for the two photon transition at 3.2 G field. Black Points are the experiment and red solid curve is a fit to Eq 4.3.

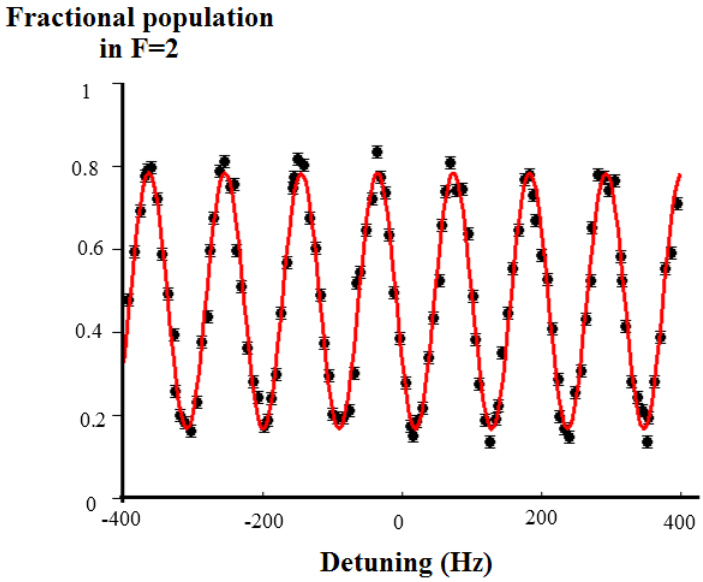

Figure 5.16: Interference fringes for the two photon transition at 3.2 G field. Black Points are the experiment and red solid curve is a fit to a sinusoidal function.

5.4 Conclusion

In this chapter we characterize the two photon transition. We are able to experimentally couple the $|p\rangle \longrightarrow |m\rangle$ transition using simultaneous MW and RF signals. The RF pulse is emitted from the designed RF antenna. This characterization is required to do the dual interferometer that we describe in the next chapter.

Chapter 6

Dual Interferometer

6.1 Introduction

We aim to use two independent Ramsey type interferometers simultaneously. The interferometry based on clock transition $|F = 1, m = 0\rangle$ to $|F = 2, m = 0\rangle$ has an optimum operating point for the magnetic field at $B = 0$. The second interferometer works on the $|F = 1, m = -1\rangle$ to $|F = 2, m = 1\rangle$ transition and the minimum magnetic sensitivity happens at $B = 3.2$ G. In this chapter we demonstrate the experimental setup for the mixture of two interferometers. The dual interferometry gives a minimum of the field fluctuation at the tunable value of the magnetic field between 0 and 3.2 G. We found that the point of minimum sensitivity depends on the fraction of atoms in each interferometer and we vary the population in each interferometer controlled with a microwave preparation pulse.

6.2 Overview

The response of atoms to magnetic fields has been an active topic of research for many years. Atoms can be configured as magnetometers that achieve sensitivity slightly better than other available technologies [66]. These sensors have been used to achieve magnetic noise free regions [67, 68, 69, 70], to study bio-magnetism [71, 72], to generate squeezing in spin systems [73, 74, 75] or to look for physics beyond the Standard Model [76, 77]. The magnetic sensitivity becomes a source of noise in experiments that use atoms as sensors for other quantities. Magnetic fluctuations are a common source of decoherence in quantum information applications [78]. The choice of the proper transition and the use of active feedback or magnetic shielding helps minimizing these effects [70, 79, 80]. Atomic clocks, for example, use the so called clock transition that connects levels with no linear Zeeman effect (see Eq 5.3). In this case coherence times up to 58 s have been achieved thanks to the spin self rephasing mechanism [81]. People tries to keep the coherence of the spin states over long times. The reduction for this dephasing can be achieved by the spin echo technique. For example, by applying a $\pi/2$ pulse in the beginning their Bloch vectors are parallel but the dephasing shows up. With the π resonant pulse, the refocusing of spin vectors prevents the decoherence. For atoms trapped in optical traps,

there is in addition a differential ac Stark shift between the hyperfine levels that can be canceled by having elliptical polarization at a particular magnetic field value [3, 82, 83, 84]. The ac Stark shift is proportional to the wavelength of the light (λ) and polarizabilities of the two atomic level system. Suitable choices for the λ and polarization, the trap becomes insensitive to the light shift. Coherence times of six hours have been obtained using rare earth doped crystals at a Zero First Order Zeeman (ZEFOZ) point [85]. The effect of environmental fluctuations is further reduced by using Dynamical Decoupling (DD) to extend the coherence time [83, 86]. To suppress the decoherence in the quantum memories, DD which is a similar scheme as spin echo has been realized with bunch of resonant pulses to rephase the spin of the system [85]. Other experiments use an extra atomic specie as co-magnetometer to determine the magnetic environment as the measurement takes place [67, 76, 87]. In the search for the electric dipole moment (EDM) of neutron, the people in reference [88] applied the magnetic field to the neutron. The precession of neutron is mostly affected by the surrounding magnetic field fluctuations. For the detection of these fluctuations, they used the mercury (Hg) as a reference to correct the systematic error on the neutron.

To have minimum magnetic sensitivity, the two levels involved in the transition must have the same magnetic response. Besides the clock transition, the other two photon insensitive transition was discussed in previous chapter. The linear Zeeman shift is the same for both levels and cancels, leaving only the quadratic Zeeman effect around a particular magnetic field value. The minimum sensitivity for this two photon transitions is achieved at 3.2 G for the case of rubidium [2] via Eq 5.2. Since atoms in those two levels have a similar magnetic moment at that field, it is possible to overlap them in a magnetic trap [4]. Fermionic alkali atoms do not have a clock transition, but they still have a magnetic insensitive single photon transition at low magnetic field between $|F = 1, m = 1/2\rangle$ and $|F = 2, m = -1/2\rangle$ [89].

It is possible to modify the magnetic response of the atoms using microwave dressing. Applying an off-resonant microwave field shifts the point of minimum magnetic sensitivity and, if properly tuned, it is even possible to cancel the linear and the quadratic Zeeman effect. In the [90] reference, a microwave field with the particular detuning respect to the hyperfine splitting in ^{87}Rb is used to dress the two photon $|F = 1, m = -1\rangle \longrightarrow |F = 2, m = 1\rangle$ transition in a magnetic trap. Thanks to the microwave dressing, they enhance the coherence time between superposition states in the arbitrary magnetic fields. This microwave dressing has been exploited to control the spinor dynamics in Bose Einstein condensates [91], increase the coherence times of Qubits [92] and improve the performance of atomic clocks [93]. Here in this chapter, we discuss the mixture of clock and two photon magnetic insensitive transitions to form a dual interferometer in rubidium. We aim to have minimum magnetic sensitivity at a tunable point between 0 and 3.2 Gauss. The point of minimum sensitivity depends on the fraction of atoms in each interferometer. Both transitions are excited simultaneously and they contribute independently to the total signal. Simultaneous interferometers have been used in gravimetry applications to eliminate common noise coming from vibrations [1, 94, 95] or to determine magnetic field gradients [96, 97]. In reference [94], they use the dual species (^{85}Rb and ^{87}Rb isotopes) Mach Zehnder type atom interferometer which is derived by the Raman transitions. The Raman pulses couple $|F = 2, m = 0\rangle \longrightarrow |F = 3, m = 0\rangle$ for ^{85}Rb

and $|F = 1, m = 0\rangle \longrightarrow |F = 2, m = 0\rangle$ for ^{87}Rb hyperfine levels at the same time. They plot the the interferometric signal (fringes) from ^{85}Rb versus the one from ^{87}Rb and it gives an ellipse. They saw no fringes when they produce the vibration in the retro reflected Raman beam but still the ellipse was visible. The fit on the ellipse gives the differential phase shift and thus the differential acceleration ($\Delta g/g$).
This has been essential for precision measurements such as the determination for the Newtonian gravitational constant [98]. These works obtain the phase of each interferometer independently to eliminate common noise. In our case we excite two transitions on the same atom and we measure directly the combined signal from both interferometers that has the cancellation built in. The technique presented here has the advantage that the atoms evolve in complete darkness, compared with RF dressing techniques [90] that requires maintaining an stable RF field on during the free evolution. The first interferometer works on the clock transition that goes between the hyperfine levels $|l\rangle \leftrightarrow |u\rangle$ (green arrow in Fig 5.5), with an associated Rabi frequency Ω_c. The second interferometer works between the hyperfine levels $|m\rangle \leftrightarrow |p\rangle$ (red arrow in Fig 5.5), with a Rabi frequency Ω_{MW}. According to the previous chapter, we excite this transition by combining a microwave field (Ω_{MW}) and an RF field (Ω_{RF}) detuned by Δ from the intermediate level.

6.3 Principles of Dual Interferometer

We initialize the atoms in $|l\rangle$ and we transfer some of the population to $|p\rangle$ with a microwave pulse of Rabi frequency Ω_p (blue arrow in Fig 5.5). The pulse duration (τ) determines the percentage of atoms in the two photon ($P = \sin^2[\Omega_p\tau/2]$) and clock ($1-P$) interferometers. The state after the preparation pulse is given by

$$|\Psi\rangle = \sqrt{1-P}\,|l\rangle - i\sqrt{P}\,|p\rangle\,. \tag{6.1}$$

We apply a resonant $\pi/2$ pulse on the clock and two photon transitions to initialize the two interferometers. After some evolution time (T) we obtain

$$|\Psi\rangle = \sqrt{(1-P)/2}(|l\rangle - ie^{i\delta_1 T}\,|u\rangle) - i\sqrt{P/2}(|p\rangle - ie^{i\delta_2 T}\,|m\rangle). \tag{6.2}$$

with $\delta_i = \omega_{mi} - \omega_{ai}$ the detuning, ω_{mi} and ω_{ai} the microwave and atomic frequencies of the clock ($i = 1$) and two photon ($i = 2$) transitions.

For small magnetic fields the frequency separation between the levels $|F = 1, m_1\rangle$ and $|F = 2, m_2\rangle$ is given by [105]

$$\begin{aligned}\omega_{ai} &= \omega_{HFS}\left[1 + \left(\frac{m_1+m_2}{4} + \gamma_2(m_2-m_1)\right)aB\right. \\ &\quad \left. + \left(\frac{1}{2} - \frac{m_1^2+m_2^2}{16}\right)a^2B^2\right],\end{aligned} \tag{6.3}$$

where $\omega_{HFS}/2\pi = 6.834$ GHz is the hyperfine splitting, $\gamma_2 = (g_I m_e/m_p)/(g_s + g_I m_e/m_p) = -4.97 \times 10^{-4}$, $a = (g_s\mu_B + g_I\mu_N)/\hbar\omega_{HFS} = 4.1 \times 10^{-4}$ G^{-1}, g_s

and g_I are the electron orbital and nuclear g-factors, μ_B and μ_N are the Bohr magneton for the electron and nucleus, m_e and m_p are the mass of electron and proton, and the values have been evaluated for ^{87}Rb (see Appendix C). For the two transitions that we are exciting we have

$$\begin{aligned}\delta_1 &= (\omega_{m1} - \omega_{HFS} - D_1 B^2) \\ \delta_2 &= (\omega_{m2} - \omega_{HFS} - C_2 B - D_2 B^2),\end{aligned} \tag{6.4}$$

with

$$\begin{aligned}D_1 &= \frac{a^2}{2}\omega_{HFS} = 2\pi\ (575\ \text{Hz/G}^2) \\ D_2 &= \frac{3a^2}{8}\omega_{HFS} = 2\pi\ (431\ \text{Hz/G}^2) \\ C_2 &= (2\gamma_2 a)\omega_{HFS} = 2\pi\ (-2785\ \text{Hz/G}).\end{aligned} \tag{6.5}$$

A second resonant $\pi/2$ pulse completes the interferometer and we measure the fraction of atoms in the upper hyperfine levels. The detection method does not distinguish between Zeeman sublevels in the upper hyperfine level giving a signal equal to

$$S = |c_u|^2 + |c_p|^2 = \frac{1}{2}\left[1 + (1-P)\sin(\delta_1 T) + P\sin(\delta_2' T)\right], \tag{6.6}$$

where we have added an offset on the detuning $\delta_2 = \delta_2' + \pi/2\tau$ to have both fringes in phase. The measured signal does not depend on the relative phase between the two interferometers. This is because both transitions work independently and do not interfere with each other, in other words, there is no pulse that connects both interferometers at the end. The above calculation assumes resonant fields during the excitation and considers the effect of the detuning only during the free evolution time (T). This is a good approximation when the time between pulses is much larger than their duration.

To have magnetic field insensitivity we must have $\partial S/\partial B = 0$. Care must be taken to avoid removing at the same time the sensitivity to the quantity of interest. Consider for example the case where we populate each interferometer equally ($P = 1/2$). Scanning the microwave frequency of only one of the interferometers would give fringes with half the total visibility. If the two interferometers have opposite phase, then the total signal (which is the sum of the two) would give no fringes. Instead we want to have both fringes with the same phase to have complete sensitivity to the quantity of interest (gravity for example), but with an opposite response to magnetic field fluctuations. Here the variation in magnetic field would shift the clock fringes slightly to the left and the two photon fringes to the right in a way to minimize the effect of the magnetic field variation for the sum.

The signal variation $\Delta S = (\partial S/\partial B)\Delta B$ for a small change in the magnetic field ΔB can be calculated from Eq 6.6 for an interferometer operating at the middle of the fringe ($\acute{\delta_1}, \delta_2 \approx 0$) and gives

$$\Delta S = (-2D_1 B_0 + P[2(D_1 - D_0)B_0 - C_2])T\Delta B. \tag{6.7}$$

The minimum magnetic sensitivity ($\Delta S = 0$) is achieved at

$$B_{min} = -\frac{PC_2}{2PD_2 + 2(1-P)D_1}. \tag{6.8}$$

We see from this equation that the magnetic field value of minimum sensitivity can be continuously tuned between 0 and 3.2 Gauss by varying the fraction of atoms in each interferometer. In particular if all the atoms are in the clock interferometer, then $P = 0$ and the minimum sensitivity happens at 0 Gauss as expected. If instead all the atoms are in the two photon interferometer, then $P = 1$ and we get $B_{min} = -C_2/2D_2 = 3.2$ Gauss [2]. In the next sections we provide the experimental demonstration of this dual interferometer with tunable point of minimum magnetic sensitivity.

6.4 Experimental setup

We start with 10^8 atoms captured in a MOT. We apply an optical molasses to the atoms during 3 ms to lower their temperature to 3 μK [106]. To initialize all the atoms in the $5S_{1/2}$, $|l\rangle$ state, the already discussed preparation process in Chapter 4 has been considered. We block the beams with mechanical shutters to ensure that there is no scattered light during the interferometric sequence [50]. The above preparation steps happen at a magnetic field of 380 mG with the magnetic field gradient off, since we get good optical pumping at this value. We quickly change the magnetic field to a particular desired value while the atoms are in free fall. Following the discussion in previous chapter, this is achieved with a circuit using two IGBT's. We allow 7 ms for the magnetic field to stabilize before we apply the interferometer sequences. The magnetic field changes less than 25 mG during the time between the interferometry pulses with a reproducibility better than 1 mG.

The microwave excitation sequence and the system to generate it is depicted in Fig 6.1. The preparation pulse determines the population on each interferometer (blue arrow in Fig 5.5). It occurs during the preparation steps at 380 mG before ramping up the magnetic field. It is generated directly from a synthesizer (Phase Matrix QuickSyn FSW-0010) and the pulse timing is controlled by an internal switch on the synthesizer and an external switch that selects between this and the other microwave signals (blue in Fig 6.1). The clock interferometer pulses (green arrow in Fig 5.5) are generated as discussed in the chapter 4 by combining the microwave and RF signals in a single sideband modulator (green in Fig 6.1). The microwave signal comes from a PLL synthesizer (EVAL-ADF4350EB2Z) that is frequency doubled, filtered and amplified. The microwave field of the two photon interferometer (Ω_{MW}) is generated in a way similar to the clock transition but with an independent RF generator that is selected through a switch (red in Fig 6.1). The RF part of the two photon transition (Ω_{RF}) comes directly from an RF generator that feeds a loop antena that is located near the position of the atoms.

To ensure frequency stability, all the synthesizers are connected to an atomic clock (SRS FS-725). All the microwave signals go through a common amplifier and they are emitted from a horn. The additional frequencies in the single sideband modulator are suppressed by more than 36 dB and have a negligible effect on the atoms since they lie 14 MHz away from the clock transition. We

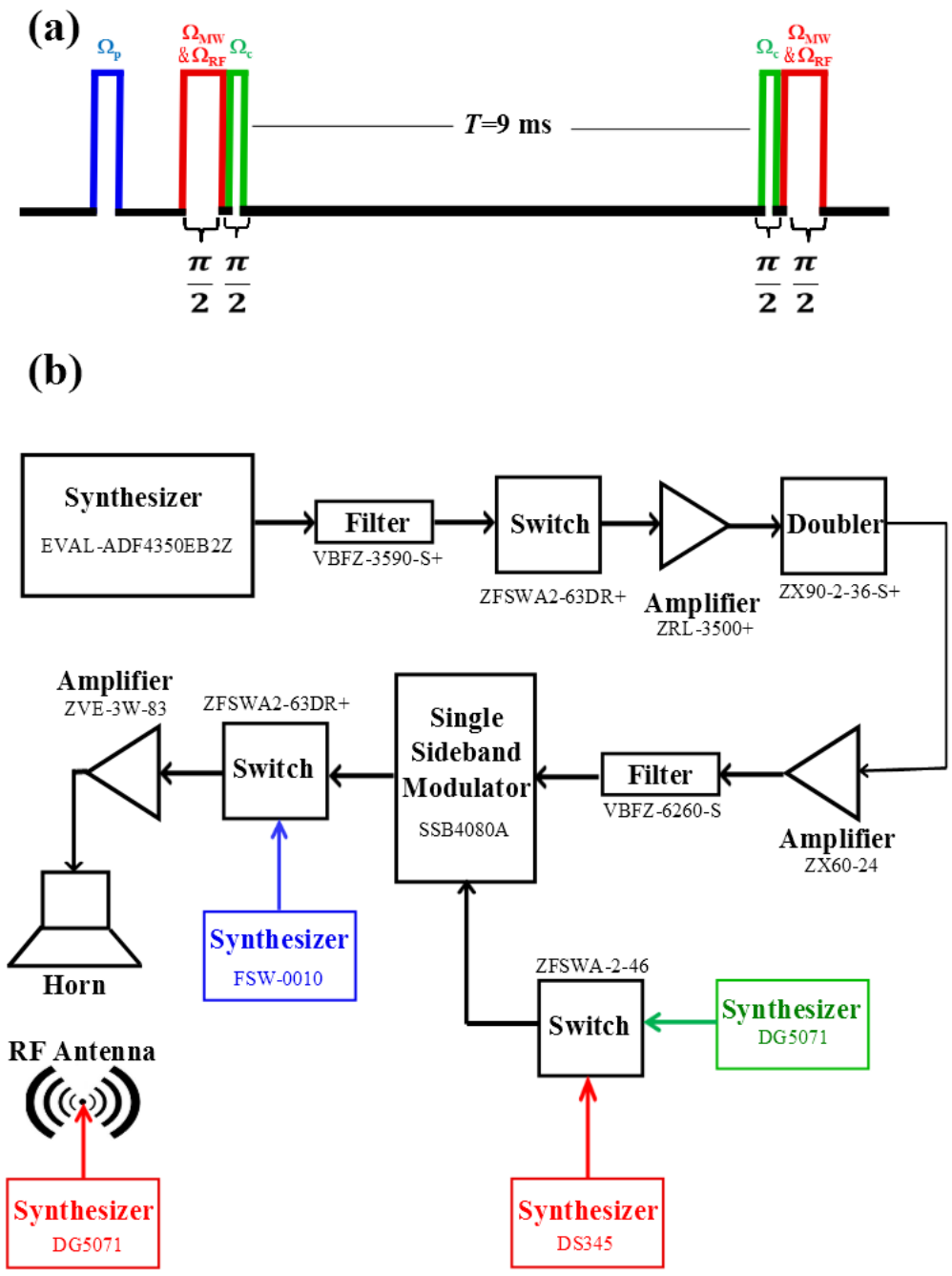

Figure 6.1: Microwave pulse sequence and microwave system.

collect the fluorescence from the atoms in a double relay imaging system with an iris in the middle for background reduction (see Section 2.6) [106]. The light goes to a CCD camera and to a photodiode connected to a DAQ card. After the interferometer sequence we determine the fraction of atoms in the $F = 2$ level by shining a beam resonant with the cycling transition and normalizing it with the signal obtained after repumping all the atoms (see Section 4.6 for the scattered light correction).

6.5 Rabi oscillations in the transitions of interest

We excite Rabi oscillations in the clock transition. Here we did not apply the preparation pulse (Ω_p) so that all the atoms remain in the $|l\rangle$ state. The horn orientation must be selected to be able to drive both the π and σ^+ transitions needed for the clock and two photon transitions. The Rabi frequency is $\Omega_c/2\pi = 4.5$ kHz with a coherence time of 0.5 ms. Figure 6.2 (a) shows Rabi oscillation for the clock transition. We set a 55 μs excitation duration for the $\pi/2$ interferometer pulses and the interferometric fringes for the clock transition are depicted in Fig 6.2 (b). We induced transitions between Zeeman sublevels to characterize the RF part of the two photon transition (Ω_{RF}) as explained in Section 5.2.1. We adjusted the magnitude of the field to have a Rabi frequency of $\Omega_{RF}/2\pi = 6$ kHz, similar to that obtained for Ω_{MW}.

To characterize the two photon transition, we set the preparation field (Ω_p) to a π pulse to have all the atoms available for this transition. The signal shows a dip (Fig 5.14) since the atoms go to the lower hyperfine level when they are excited on resonance. The detuning we use ($\Delta/2\pi = 70$ kHz) is considerably bigger than the individual Rabi frequencies to avoid single photon excitations. The typical two photon Rabi frequency is $\Omega_2/2\pi = 0.5$ kHz with a coherence time of 9 ms, and we set a 500 μs excitation duration for the $\pi/2$ interferometer pulses.

To be able to treat each interferometer independently, it is important to minimize the effect of the clock microwave field on the two photon transition and vise versa. Having the fields for both transitions simultaneously on could potentially drive undesired multi-photon transitions. Instead we shine the two fields sequentially. We leave the clock interferometer inside since it has a shorter pulse (higher Ω_c) and since that field alone cannot drive a two photon transition. In contrast, it is possible to drive the clock transition with a two photon transition. Figure 5.8 shows a two photon spectrum taken with the preparation pulse off so that all the atoms are in the clock transition (lower blue curve), and with a π preparation pulse with all the atoms in the two photon transition (upper red curve). Here we see the desired two photon transition and the unwanted two photon clock transition. We only work at high fields to have these two transitions spectrally resolved thanks to the quadratic Zeeman shift (10.4 kHz at 3.2 G). The separation between peaks is 21 times larger than their width, that is limited by the two photon pulse duration.

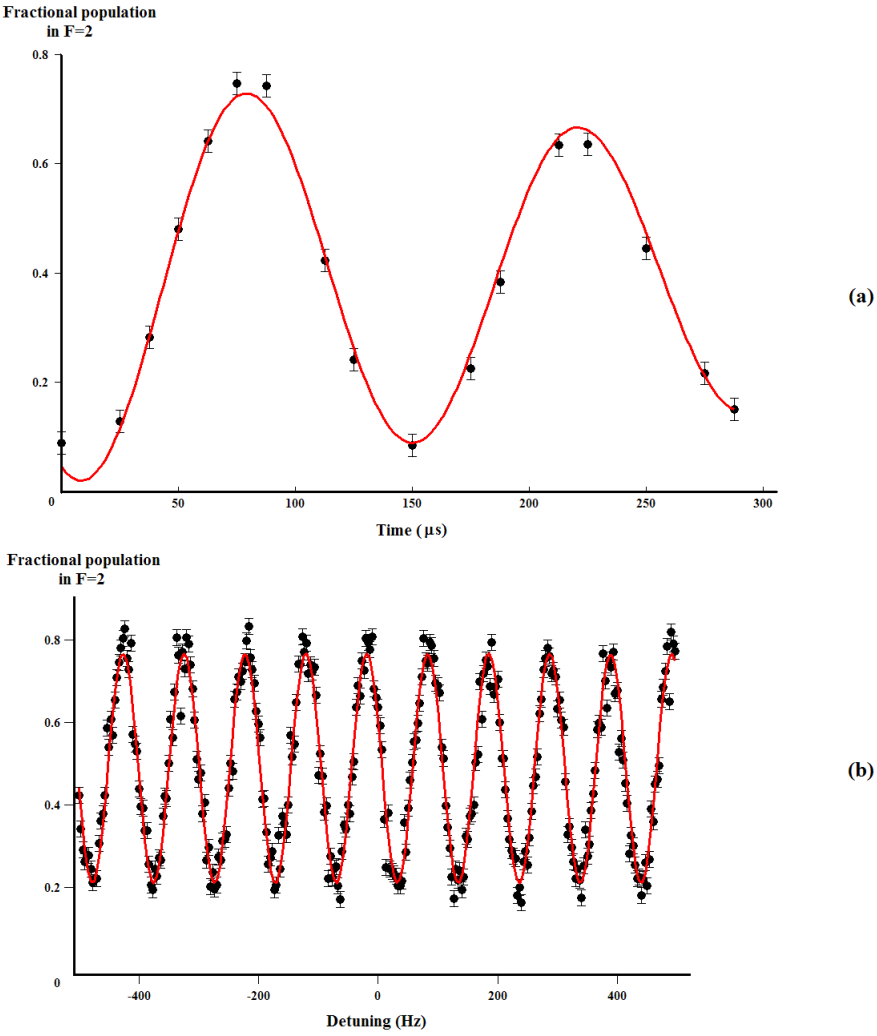

Figure 6.2: (a) Rabi oscillation for clock transition. We get $\Omega_c/2\pi = 4.5$ kHz with a coherence time of 0.5 ms. (b) interference fringes for the clock transition at 3.2 G field. Experimental data points are shown in black and red curve is a fit of a sinusoidal function.

6.6 Dual interferometer

We excite both interferometers simultaneously using the sequence from Fig 6.1 to demonstrate the tunable point of minimum magnetic insensitivity. Using the LabView software in the control system, we do all steps subsequently. Figure 6.3 shows part of the written program in LabView front panel for the dual interferometer experiment. In the image the red rectangular box shows Ramsey $\pi/2$-Time Evolution-$\pi/2$ sequences during the darkness which configured in Fig 6.1.

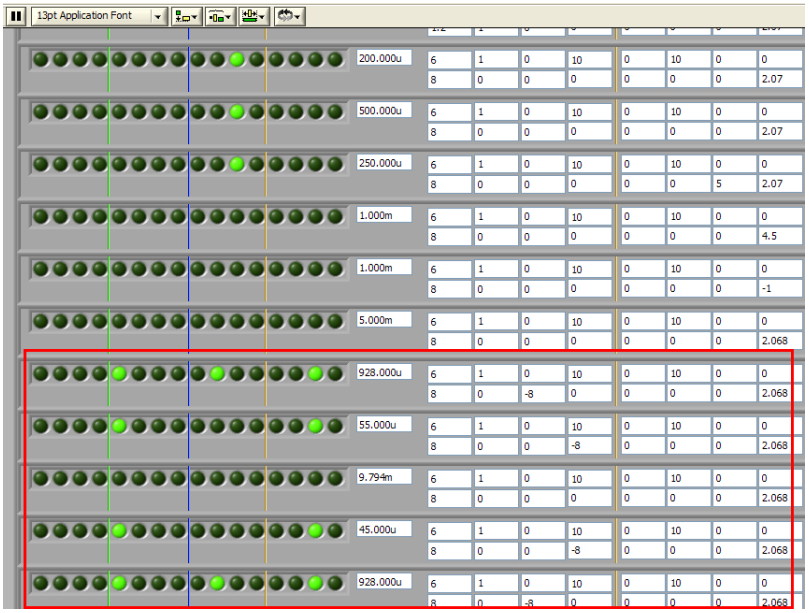

Figure 6.3: Part of the written program in LabView front panel for the dual interferometer project. The red rectangular box shows Ramsey $\pi/2$-Time Evolution-$\pi/2$ sequences.

We scan the frequency of each interferometer independently to obtain fringes and we sit at the middle of the fringe in the rising slope in both of them. To characterize the magnetic sensitivity at a particular magnetic field B_0, we measure the interferometer output (Eq. 6.6) with a magnetic field slightly higher and lower and we take the difference of the two, $\Delta S = S(B_0+\Delta B)-S(B_0-\Delta B)$. The value of the magnetic field is determined by the control system. We keep the B_0 constant and we repeat the measurement as we vary the duration of the preparation pulse (Fig 6.4). This changes the fraction of atoms in the two photon (P) and clock ($1-P$) interferometers (Fig 6.5). Consider for example the case with $B_0 = 2.5$ G shown in Fig 6.5. When all the atoms are in the clock transition ($P = 0$) the fringes shift to lower frequencies and $\Delta S < 0$. On the other hand, if all the atoms are in the two photon transition ($P = 1$) the shift is in the opposite direction and $\Delta S > 0$. As we move continuously from one case to the other we find a position ($P = 0.80(3)$) where there is no shift. This is the point of minimum magnetic sensitivity that moves to the left as we decrease the magnetic field. We repeated this measurements at 2.24 G, 2.5 G, 2.71 G, 2.88

G and 3.2 G fields and in each case we found particular P's for the minimum magnetic sensitivity of our dual interferometer. The horizontal axes in Fig 6.4 is the normalized time for the preparation pulse that it comes from the pulse duration divided by the experimental π pulse. We always define the π pulse by doing Rabi Oscillations in the states of interest. We passed the duration for the π pulse and the signal starts to drop. An absolute fit function can also give the exact duration for a π pulse. The theoretical signal variation (Eq 6.7) is also

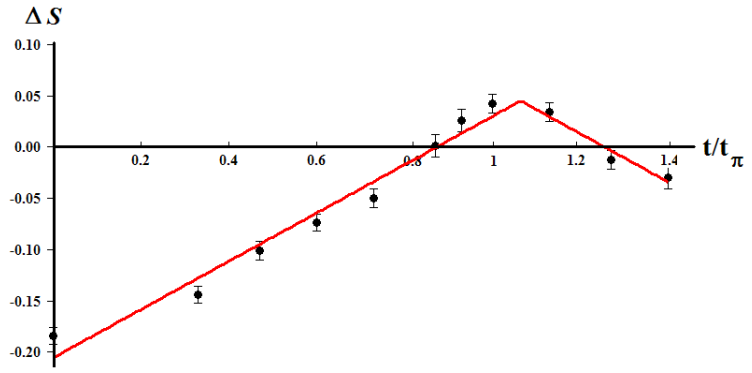

Figure 6.4: Signal variation versus the normalized duration of preparation pulse (t/t_π) at 2.5 G. The solid red line is an absolute fit to the data.

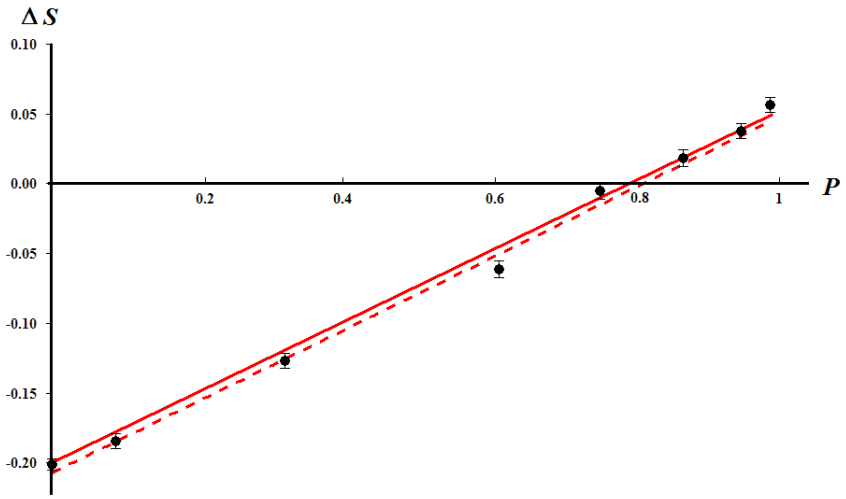

Figure 6.5: Signal variation with magnetic field (ΔS) as a function of the fraction of atoms in the two photon transition (P) at 2.5 G. The solid red line is a fit to the data and the red dashed line gives the theoretical signal (Eq 6.7) for ΔB=1.2 mG.

shown as a red dashed line in Fig 6.5 for ΔB=1.2 mG. This ΔB value gives good agreement with the data and it is similar to that estimated from spectroscopic measurements. The atomic spectroscopy is done to estimate the magnetic field sensed by the atoms. For example we start all the atoms in $|l\rangle$ state and then

we shine the microwave signal while its frequency is swept. This gives the peaks (Fig 4.3) that the separation of these peaks can be translated to the magnetic field. The fringes in the clock (two photon) transitions shift in Hz as $\Delta\nu_c$ ($\Delta\nu_2$) respectively when we change the magnetic field by ΔB in Gauss given by

$$\begin{aligned}\Delta\nu_c &= 2\left(\frac{D_1}{2\pi}\right)B_0\Delta B \\ \Delta\nu_2 &= \left[2\left(\frac{D_2}{2\pi}\right)B_0 + \left(\frac{C_2}{2\pi}\right)\right]\Delta B,\end{aligned} \tag{6.9}$$

where B_0 is the magnetic field and ΔB is the change in the field. It would introduce a shift of 3.1 % (-0.7 %) of a fringe for the clock (two photon) transition. We get these numbers by dividing $\Delta\nu_c$ and $\Delta\nu_2$ to the total fringe ($1/T$) frequency. The visibility remains almost unchanged with this small shift and the interferometer retains full sensitivity to other quantities of interest. In our measurements we work at a particular B_0 and we change P since that is more stable.
Alternatively one can vary the magnetic field (B_0) and keep the fraction of atoms in each interferometer (P) constant. This is somewhat less reproducible than the method above since the middle of the fringe operating point needs to be set at each new magnetic field value and the ΔB is slightly different. Figure 6.6 shows the result obtained by this procedure with $P = 1$ (all the atoms in the two photon transition) that shows a minimum sensitivity at 3.20 $\pm$ 0.02 G as expected.

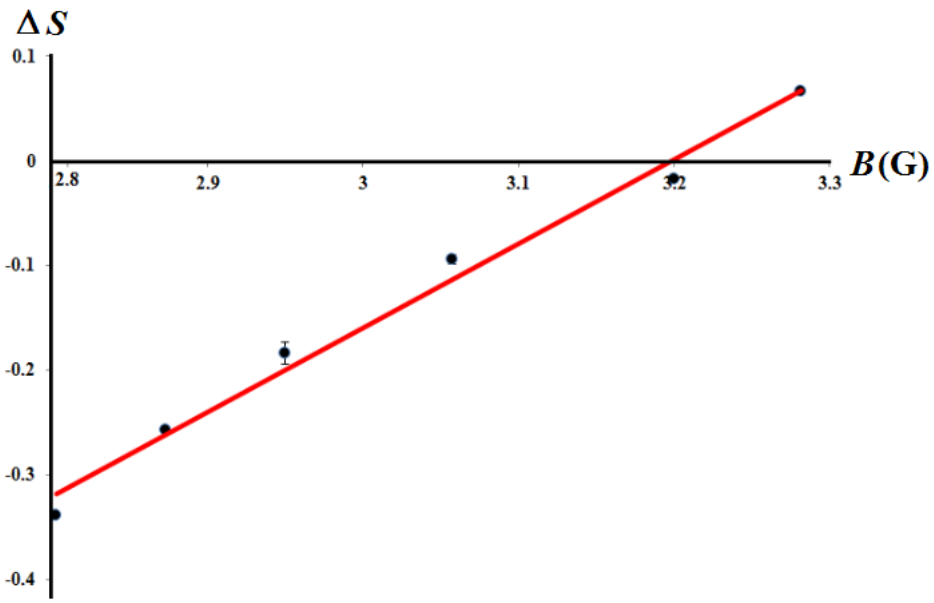

Figure 6.6: Signal variation with magnetic field (ΔS) measured at $P = 1$ at different values of the magnetic field.

Figure 6.7 shows the population fraction (P) needed to have minimum magnetic sensitivity at a particular field ($B_0 = B_{min}$). The solid line corresponds to

the expected dependence from Eq 7.3. The theory works well as long as the two interferometers can be considered independent of each other. As the magnetic field is decreased, the separation between the two peaks in Fig 5.8 decreases and the two transitions start affecting each other. This prevents the extension of the operation of the dual interferometer to lower magnetic fields (Fig 6.7).

Respect to Eq 6.7, the dual interferometer maintains the same quadratic dependence on magnetic field of the independent interferometers since the D_0 and D_1 coefficients are almost the same, but shifts the point of minimum sensitivity to the desired value. The shift is almost linear with the population in each interferometer (see Fig 6.7) as long as the visibility in both interferometers is similar.

We consider the case that the visibility of interferometric fringes are not equal, then according to Eq 6.6 the condition for the magnetic insensitivity is given by

$$V_c(1-P)\frac{\partial \delta_1}{\partial B} = -V_2 P \frac{\partial \delta_2}{\partial B}, \tag{6.10}$$

where V_c and V_2 are the visibilities for the clock and two photon interferometers. We define the ratio of these visibilities by $V_r = V_c/V_2$. By applying this modification, Eq 7.3 becomes

$$B_{min} = -\frac{PC_2}{2PD_2 + 2(1-P)D_1V_r}. \tag{6.11}$$

In the experiment we found almost the same visibilities ($V_r = 1$) for both fringes. The red solid (blue dashed) line in Fig 6.7 shows the case where the ratio of visibilities are $V_r = 1(2)$ respectively.

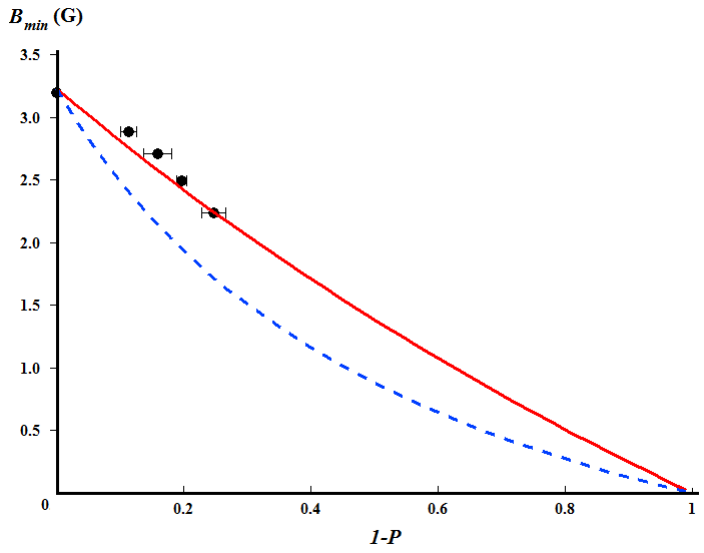

Figure 6.7: Fraction of atoms in each interferometer (P) required to have minimum sensitivity at a particular magnetic field (B_{min}). The red solid (blue dashed) line corresponds to Eq 6.11 with $V_r = 1(2)$.

6.7 Conclusion

In this chapter we discussed about developing a dual interferometer that achieves a minimum magnetic sensitivity at a tunable value of the magnetic field. Combining the clock and the two photon transition between $|m\rangle$ and $|p\rangle$ we are able to tune the point of minimum magnetic sensitivity between 2.2 and 3.2 G by changing the fraction of atoms in each interferometer. In our scheme both interferometers work independently. The dual interferometer may be useful in applications where low magnetic sensitivity is required at a particular magnetic field.

Chapter 7

Conclusion and Outlook

7.1 Conclusion

Methods based on quantum interference using cold atoms, were largely used in recent years for precision measurements. This requires laser cooling techniques for the coherent control of atomic ensemble. One of the systematic error for these interferometers would be magnetic field fluctuation. The aim of this PhD work was developing a dual interferometer based on two magnetic insensitive transitions in ^{87}Rb atoms where each transition has its own minimum sensitivity point. For dual interferometer, we experimentally found out that the minimum sensitivity depends on the fraction of atoms in each interferometer as expected from theory. We excite both transitions simultaneously and they contribute independently to the total signal. The first interferometer works on the clock transition that goes between the hyperfine levels $|F = 1, m = 0\rangle \leftrightarrow |F = 2, m = 0\rangle$. The second interferometer works between the hyperfine levels $|F = 1, m = -1\rangle \leftrightarrow |F = 2, m = 1\rangle$. The second interferometer uses a microwave field (Ω_{MW}) and an RF field (Ω_{RF}) to excite a two photon transition. By changing the population on each transition, we were able to tune the point of minimum magnetic sensitivity between 2.2 and 3.2 G. In the next section we discuss an alternative method to develop the dual interferometer that uses only single photon transitions.

7.2 Outlook

7.2.1 Alternative method for the dual interferometer

Here we discuss about experimental aspects of an alternative method using different microwave pulses to make the two photon transition possible with only single photon transitions. Figure 7.1 (a) shows the four levels system (in black color) of ^{87}Rb used to combine $|l\rangle \leftrightarrow |u\rangle$ and $|m\rangle \leftrightarrow |p\rangle$ interferometers in the presence of external magnetic field. The idea is to prepare the atoms in $|l\rangle$ and add some microwave pulses using a PLL synthesizer (EVAL-AD4350EB2Z) and an arbitrary function generator (Rigol DG5071). Figure 7.2 shows a block diagram of the microwave generation system. The Rigol synthesizer receives its 10 MHz clock signal from a function generator (SRS DS345) that is locked to

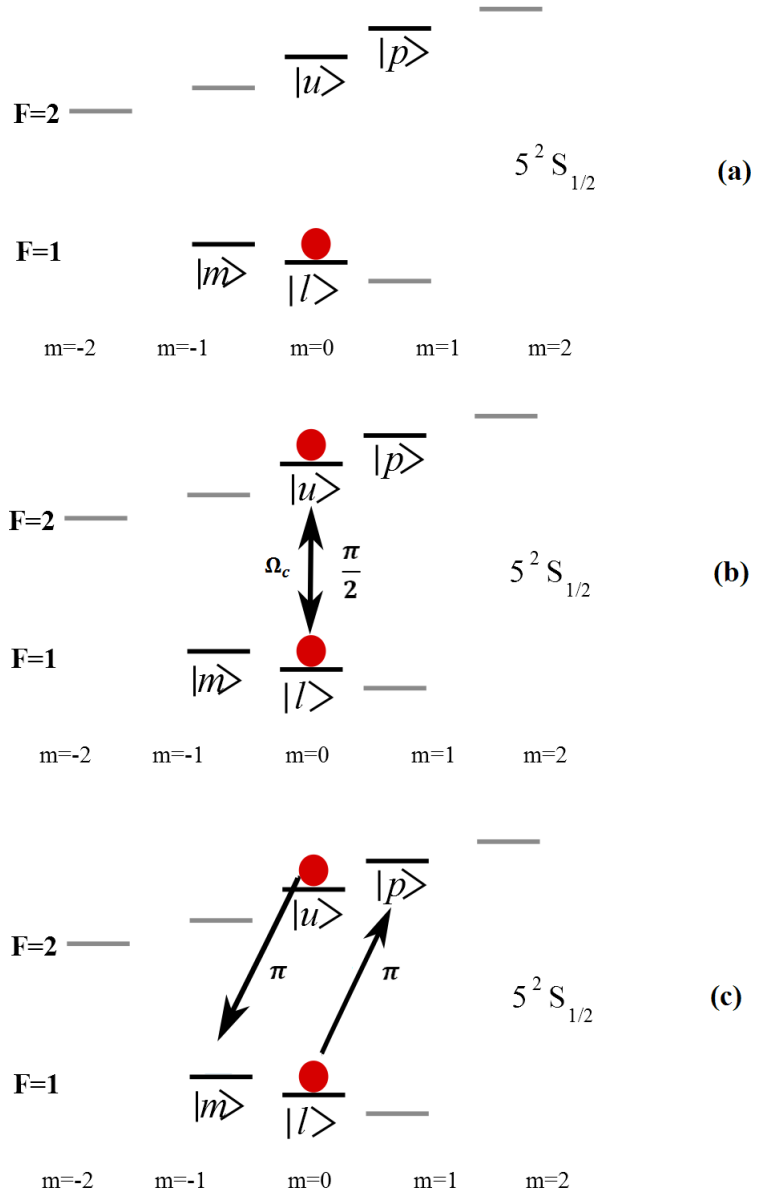

Figure 7.1: Ramsey sequence for two photon transition using alternative method. (a) All the atoms are initialized at $|l\rangle$ sublevel. (b) A $\pi/2$ pulse resonant with $|l\rangle \leftrightarrow |u\rangle$ splits atomic cloud into a 50-50 % superposition. (c) The bursts of π pulses resonant with $|l\rangle \longrightarrow |p\rangle$ and $|u\rangle \longrightarrow |m\rangle$ starts the first $\pi/2$ in Ramsey sequence.

the atomic clock and this lets us sweep the frequency of the synthesizer for the interferometric purposes. It is also possible to load an arbitrary signal through an Excel file via the USB connection of DG5071. After loading the desired signal to the synthesizer we need to adjust the time base of the synthesizer to obtain the desired frequency. We correct the time base by comparing the signal of the arbitrary synthesizer to a fixed frequency synthesizer (DG1022A) with a phase detector (Minicircuits ZRPD-1+). The Intermediate Frequency (IF) output of the phase detector is monitored in the oscilloscope. Once we enter manually the desired signal frequency in DG1022A with 11 digit precision thanks to the atomic clock, we are able to remove residual beat note between two synthesizers by moving the time base (frequency) knob in DG5071. We can unplug the synthesizer DG5071 once we assure that the correct frequency has been achieved. The pulses for the arbitrary function generator can be triggered from the control system.

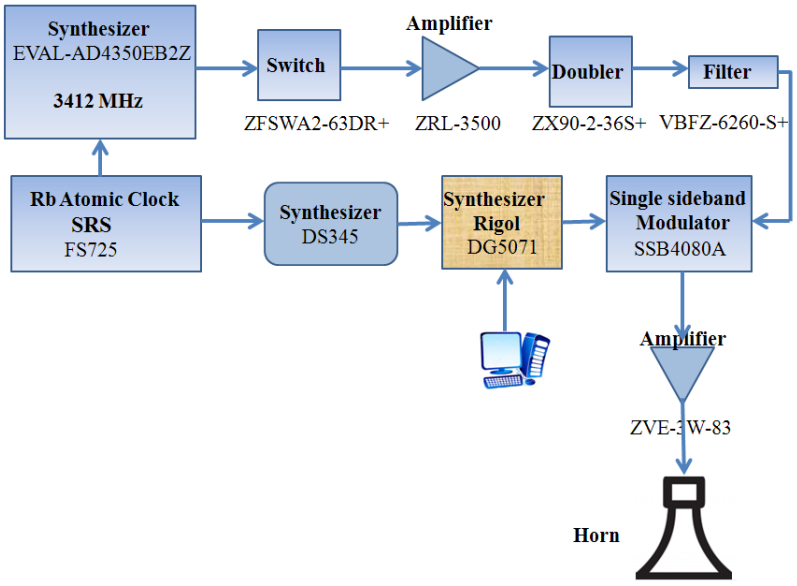

Figure 7.2: Block diagram for the microwave generating system of alternative method for doing interferometry on the two photon transition.

To do the two photon transition, all discussed initialization steps in Chapter 4 like capturing the atoms, optical molasses, optical and Zeeman pumping in the presence of 100 mG magnetic field were applied in order to initiate the atoms in $|l\rangle$ (see Fig 7.1 (a)). To make possible the $|m\rangle$ to $|p\rangle$ transition using single microwave pulses, first we apply a $\pi/2$ on the clock transition, then immediately, we continue the sequence and shine simultaneously the π pulses resonant with $|l\rangle$ to $|p\rangle$ and $|u\rangle$ to $|m\rangle$ (Fig 7.1 (c) and (d)). In this situation we are sure that a coherent 50-50 % superposition of atoms is prepared between the $|p\rangle$ and $|m\rangle$ sublevels. We let the atoms evolve for T'=10 ms in complete darkness. The second $\pi/2$ to complete the interferometer, corresponds to a similar sequence of pulses as described before, but in reverse order. All the transitions are generated with the arbitrary wave synthesizer. The Rabi oscillations for $|l\rangle \leftrightarrow |u\rangle$, $|l\rangle \leftrightarrow |p\rangle$

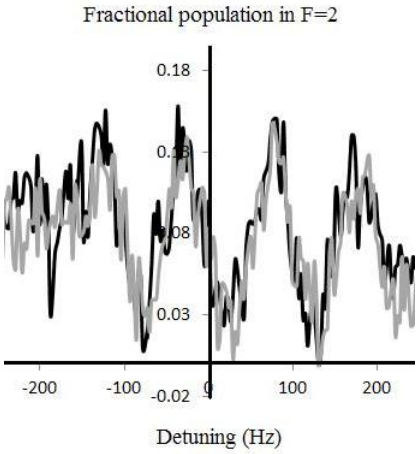

Figure 7.3: Ramsey fringes of $|p\rangle$ to $|m\rangle$ using an alternative method. The width of the peaks is 60 Hz that corresponds to the time between pulses. The experiment is repeated twice shown with the black and gray curves.

and $|l\rangle \leftrightarrow |m\rangle$ gives the duration of $\pi/2$ and π times which are 31 and 63 μs. The Ramsey fringes were observed once we swept the frequency of the DS345 synthesizer (Fig 7.3). We repeat the experiment to be sure that the fringes are not accidental. The width of the fringes are 60 Hz. We consider all Ωs are real. The signal (corresponding to the sum of populations in the upper ground state) that we get from the dual interferometer is

$$\begin{aligned} S = \cos^2(P)\sin^2(\frac{(\omega_{HFS})T}{2} + D_{00}B\Delta BT) + \sin^2(P) \\ \times \sin^2(\frac{(HFS)T}{2} + (C_{01} + C_{-10})\frac{\Delta BT}{2} + (D_{01} + D_{-10} - D_{00})B\Delta BT) \end{aligned} \tag{7.1}$$

where the numerical values for the coefficients are derived in Appendix C. Here we assume sitting at the middle of the fringe. For a small ΔB, we rewrite Eq 7.1 as

$$\begin{aligned} S = \cos^2(P)(\frac{1}{2} + D_{00}B\Delta BT) + \sin^2(P) \\ \times (\frac{1}{2} + (C_{01} + C_{-10})\frac{\Delta BT}{2} + (D_{01} + D_{-10} - D_{00})B\Delta BT) \end{aligned} \tag{7.2}$$

To obtain minimum magnetic sensitivity $\partial S/\partial B = 0$ gives us an expression for the point of minimum sensitivity to B which gives

$$B = \frac{-(C_{01} + C_{-10})P^2/2}{D_{00}(1 - P^2) + P^2(D_{01} + D_{-10} - D_{00})} \tag{7.3}$$

Appendix A

Articles

- **Multiple Isotope Magneto Optical Trap from a Single Diode Laser** V. M. Valenzuela, S. Hamzeloui, M. Gutiérrez and E. Gomez, J. Opt. Soc. Am. B **30**, 1205, (2013).
- **Towards precision measurements at UASLP** S. Hamzeloui, N. Arias, V. Abediyeh, D. Martínez, M. Gutiérrez, E. Uruñuela, E. del Rio, E. Cerda, E. Gomez, V. M. Valenzuela, J. Phys.: Conf. Ser **698**, 012011 (2016).
- **Dual atomic interferometer with a tunable point of minimum magnetic sensitivity** S. Hamzeloui, D. Martínez, V. Abediyeh, N. Arias, E. Gomez, and V.M. Valenzuela , Phys. Rev. A. Submitted.

Appendix B

Derivation of Eqs (3.6) to (3.9)

Here we want to derive Eqs 3.6 to 3.9. We start with an equation for the electric field at the output path of our intensity (amplitude) modulator:

$$E = \frac{1}{2}E_0[\cos(\omega t) + \cos(\omega t + 2bV)], \tag{B.1}$$

where ω is the light frequency and $b = 2\pi/4V_\pi$. V is the applied voltage that changes with the time as $V = V_0 + a\sin(\Omega t)$ where V_0 is the constant voltage, Ω is the modulating frequency and a is the amplitude of modulation. By substituting the V in the above equation we get

$$E = \frac{E_0}{\sqrt{2}}[\cos(\omega t) + \cos(\omega t + 2bV_0 + 2ab\sin(\Omega t))], \tag{B.2}$$

Equation 11.25 in [58] gives

$$\begin{aligned}\cos(x\sin\theta) &= J_0(x) + 2\sum_{n=1}^{\infty} J_{2n}(x)\cos(2n\theta),\\ \sin(x\sin\theta) &= 2\sum_{n=1}^{\infty} J_{2n-1}(x)\sin\left[(2n-1)\theta\right],\end{aligned} \tag{B.3}$$

To calculate the spectrum of first, second and third order sidebands, we use the trigonometric identities and Eq 11.25 in [58]. Therefore, the electric field at the output of the EOM is written by

$$\begin{aligned}E = &\frac{1}{\sqrt{2}}E_0[\cos(\gamma t) + J_0(2\omega a)\cos(\gamma t + 2\omega V_0)]\\ &+ \frac{1}{\sqrt{2}}E_0[-J_1(2\omega a)(\cos(\gamma t + 2\omega V_0 - \Omega t) - \cos(\gamma t + 2\omega V_0 + \Omega t))]\\ &+ \frac{1}{\sqrt{2}}E_0[J_2(2\omega a)(\cos(\gamma t + 2\omega V_0 - 2\Omega t) + \cos(\gamma t + 2\omega V_0 + 2\Omega t))]\\ &+ \frac{1}{\sqrt{2}}E_0[-J_3(2\omega a)(\cos(\gamma t + 2\omega V_0 - 3\Omega t) - \cos(\gamma t + 2\omega V_0 + 3\Omega t))]\\ &+ ...\end{aligned} \tag{B.4}$$

where the term with zero order Bessel function (J_0) belongs to the carrier. The first, second and third order sidebands correspond to first, second and third order of Bessel functions respectively.

Using $\cos(A-B)+\cos(A+B)=2\cos(A)\cos(B)$ and defining $A-B=\omega t$ and $A+B=\omega t+2bV$, we rewrite Eq B.1 as

$$E = E_0\left[\cos(bV)+\cos(\omega t+bV)\right], \tag{B.5}$$

When we modulate the amplitude, we also modulate the phase by bV. To see the signal we need to deal with the intensity ($I \propto E^2$). The locking signal gives

$$S = \frac{1}{T}\int_0^T \cos^2(bV_0+ab\sin(\Omega t))\cos^2(\omega t+bV_0+ab\sin(\Omega t))dt, \tag{B.6}$$

Using Eq B.3, we can express the modulated signal using Bessel functions

$$S = \frac{1}{4}\left[1+\cos\left(\pi\frac{V_0}{V_\pi}\right)J_0\left(\frac{\pi a}{V_\pi}\right)\right], \tag{B.7}$$

To get the visibility of the locking signal in Eq 3.9 we need to calculate V=(S_{max}-S_{min})/(S_{max}+S_{min}) which gives

$$S_L = J_0\left(\frac{\pi a}{V_\pi}\right). \tag{B.8}$$

where a in Eq B.8 is the same as V_m in Eq 3.9. To see the spectrum signal, we need to take the Fourier transform of E and then derive the modulus of that. The spectrum signal for the carrier looks

$$S_c = 1+2J_0(\frac{\pi a}{V_\pi})\cos(\frac{\pi V_0}{V_\pi})+J_0^2(\frac{\pi a}{V_\pi}), \tag{B.9}$$

and for the first order sideband gives

$$S_1 = J_1^2(\frac{\pi a}{V_\pi}), \tag{B.10}$$

and for the second order sideband gives

$$S_2 = J_2^2(\frac{\pi a}{V_\pi}), \tag{B.11}$$

and so on. Equations B.10 and B.11 are the same as Eqs 3.6 and 3.8.

Appendix C

Notations for the energy of levels in the rubidium atom

For the ground state of rubidium atom, it is straightforward to determine the energy of each level using [105]

$$V_{F_{\pm},M_F}(x) = \frac{\hbar(\omega_{HFS})}{2}(-2M_F\gamma_2 x \pm \overbrace{\sqrt{1+2\frac{M_F}{F_+}x+x^2}}^{A(x)}), \tag{C.1}$$

where

$$\begin{aligned} x &= \frac{B}{(\omega_{HFS})}(g_s\frac{\mu_B}{\hbar}+g_I\frac{\mu_N}{\hbar}),\\ \gamma_1 &= \frac{g_s-2Ig_I\frac{m_e}{m_p}}{2(g_s+g_I\frac{m_e}{m_p})},\\ \gamma_2 &= \frac{g_I\frac{m_e}{m_p}}{g_s+g_I\frac{m_e}{m_p}},\\ a &= (g_s\mu_B+g_I\mu_N)/\hbar\omega_{HFS}, \end{aligned} \tag{C.2}$$

where $\omega_{HFS}/2\pi = 6.834$ GHz is the hyperfine splitting, B is the magnetic field, $\gamma_2 = -4.97\times10^{-4}$, $a = 4.1\times10^{-4}$ G^{-1}, g_s and g_I are the electron orbital and nuclear g-factors, μ_B and μ_N are the Bohr magneton for the electron and nucleus, m_e and m_p are the mass of electron and proton, and the values have been evaluated for ^{87}Rb.
Expanding Equation C.1 in a Maclaurin series to the second order gives the difference in energy between two ground state levels $|F=1,m\rangle$ and $|F=2,m'\rangle$ in ^{87}Rb in the form of

$$\Delta V_{m,m'} = \hbar(\omega_{HFS})[1+(\frac{m+m'}{4}+(m'-m)\gamma_2)aB+(\frac{1}{2}-\frac{m^2+m'^2}{16})a^2B^2] \tag{C.3}$$

where $a = x/B$ according to Equation C.2. The energy shift for the clock transition

$$\Delta E = V_+(0)-V_-(0) = \hbar(\omega_{HFS})\sqrt{1+x^2} \approx \hbar(\omega_{HFS})(1+\frac{x^2}{2}), \tag{C.4}$$

In Chapter 7 for the alternative method, the coefficients in Eq 7.3 appear because of phase accumulated due to the detuning in the system which are

$$\begin{aligned}\phi_1 &= \delta_1 T = (F_{00} + D_{00}B^2)T \\ \phi_2 &= \delta_2 T = (F_{01} + C_{01}B + D_{01}B^2)T \\ \phi_3 &= \delta_3 T = (F_{-10} + C_{-10}B + D_{-10}B^2)T\end{aligned} \tag{C.5}$$

where ϕ_1, ϕ_2 and ϕ_3 correspond to the phase accumulated in $|l\rangle \rightarrow |u\rangle$ (clock transition), $|l\rangle \rightarrow |p\rangle$ and $|m\rangle \rightarrow |u\rangle$ transitions respectively and $F_{00} = \omega_{HFS} - \omega_{m_{00}}$, D_{00} is the coefficient of second order Zeeman shift for the clock transition, $F_{01} = \omega_{HFS} - \omega_{m_{01}}$, C_{01} and D_{01} are the coefficients of first and second order Zeeman shift for $|l\rangle \rightarrow |p\rangle$ respectively, $F_{-10} = \omega_{HFS} - \omega_{m_{-10}}$, C_{-10} and D_{-10} are the coefficients of first and second order Zeeman shift for $|m\rangle \rightarrow |u\rangle$ respectively. The coefficients are

$$\begin{aligned}D_{00} &= \frac{\omega_{HFS}}{2}a^2 \\ D_{01} &= \frac{\omega_{HFS}}{2}\frac{9}{16}a^2 \\ D_{-10} &= \frac{\omega_{HFS}}{2}\frac{7}{16}a^2 \\ C_{01} &= \omega_{HFS}(\frac{1}{4} + \gamma_2)a \\ C_{-10} &= -\omega_{HFS}(\frac{1}{4} + \gamma_2)a\end{aligned} \tag{C.6}$$

Using Equation C.2, we get γ_2=0.000496747, the numerical values becomes:

- $D_{00} = 2\pi(575 \quad s^{-1}Gauss^{-2})$
- $D_{01} \approx D_{-10} = 2\pi(501 \quad s^{-1}Gauss^{-2})$
- $C_{01} \approx C_{-10} = 2\pi(1390 \quad s^{-1}Gauss^{-2})$
- $C_{01} + C_{-10} = 2\pi(2780 \quad s^{-1}Gauss^{-2})$
- $D_{01} + D_{-10} - D_{00} = 2\pi(431 \quad s^{-1}Gauss^{-2})$

Bibliography

[1] J. McGuirk, G. Foster, J. Fixler, M. Snadden, and M. Kasevich, *"Sensitive absolute-gravity gradiometry using atom interferometry",* Phys. Rev. A. **65**, 033608 (2002).

[2] D. M. Harber, H. J. Lewandowski, J. M. McGuirk, and E. A. Cornell *"Effect of cold collisions on spin coherence and resonance shifts in a magnetically trapped ultracold gas",* Phys. Rev. A **66**, 053616 (2002).

[3] R. Chicireanu, K. D. Nelson, S. Olmschenk, N. Lundblad, A. Derevianko, and J. V. Porto *"Differential Light-Shift Cancellation in a Magnetic-Field-Insensitive Transition of ^{87}Rb",* Phys. Rev. Lett **106**, 063002 (2011).

[4] M. R. Matthews, E. A. Cornell, *"Dynamical Response of a Bose-Einstein Condensate to a Discontinuous Change in Internal State",* Phys. Rev. Lett **81**, 243 (1998).

[5] M. Ö. Oktel and L. S. Levitov, *"Internal Waves and Synchronized Precession in a Cold Vapor",* Phys. Rev. A **88** 230403, (2002).

[6] P. Treutlein, P. Hommelhoff, T. Steinmetz, T. W. Hänsch, and J. Reichel, *"Coherence in Microchip Traps",* Phys. Rev. Lett **92**, 203005 (2004).

[7] P. Rosenbusch, *"Magnetically trapped atoms for compact atomic clocks",* Appl. Phys. B **95**, 227–235 (2009).

[8] C. Käfer, R. Bourouis, J. Eurisch, A. Tripathi, and H. Helm, *"Ejection of magnetic-field-sensitive atoms from an optical dipole trap* Phys. Rev. A **80**, 023409 (2009).

[9] Hernández, L. (2011). *"Átomos Fríos en Trampas Ópticas",* Ph.D. Thesis, Universidad Autónoma de San Luis Potosí: México.

[10] Valenzuela, V. M. (2012). *"Sistema de Enfriamiento Láser Aplicado a Mezclas Isotópicas de Átomos Fríos* Ph.D. Thesis, Universidad Autónoma de San Luis Potosí: México.

[11] E.A. Cornell, C.E. Wieman, *"Nobel Lecture: Bose-Einstein Condensation in a Dilute Gas, the First 70 Years and Some Recent Experiments",* Rev. Mod. Phys. **74**, 875-893 (2002).

[12] E.A. Cornell *"Bose-Einstein Condensation.* Journal of Research of NIST **101**, 419-618 (1996).

[13] J. L. Martin, C. R. McKenzie, N. R. Thomas, J. C. Sharpe, D. M. Warrington, P. J. Manson, W. J. Sandle and A. C. Wilson, *"Output coupling of a Bose-Einstein condensate formed in a TOP trap.* J. Phys. B: At. Mol. Opt. Phys. **32**, 3065 (1999).

[14] H. Metcalf, P. van der Straten, *"Cooling and trapping of neutral atoms",* Phys. Rep. **244**, 204-286, (1994).

[15] K.B. Mac Adam, A Steinbach, and C. Wiemann, *"A narrowband tunable diode laser system with grating feedback, and a saturated absorption spectrometer for Cs and Rb.* Am. J. Phys. **60**, 1098 (1992).

[16] K. L. Corwin, Z. T. Lu, C. F. Hand, R. J. Epstein and C. E. Wieman, *"Frequency-stabilized diode laser with the Zeeman shift in an atomic vapor",* Appl. Opt. **37**, 3295 (1998).

[17] W. Gawlik, J. Zachorowski, *"Stabilization of diode-laser frequency to atomic transitions",* Optica Applicata. **34**, 607 (2004).

[18] Uruñuela, J. E. (2013). *"Diseño e implementación de una trampa magneto-óptica para átomos neutros",* B. Sc. Thesis, Universidad de Guadalajara: México.

[19] SAES Getters Part No. D 100-5. Datasheet is available from http://www.saesgetters.com/products/nextorr-pumps.

[20] Valenzuela, V. M. (2009). *"Sistema de Control de Laboratorio para Experimentos en Física Átomica",* M.Sc. Thesis, Universidad Autónoma de San Luis Potosí: México.

[21] M. Tablieber, A. Voigt, F. Henkel, S. Fray, T. Hänsch, and K. Dieckmann, *"Simultaneous magneto-optical trapping of three atomic species",* Phys. Rev. A **73**, 011402 (2006).

[22] S. Papp, J. Pino, and C. Wieman, *"Tunable miscibility in a dual-species Bose-Einstein condensate",* Phys. Rev. Lett. **101** 040402 (2008).

[23] N. Nemitz, F. Baumer, F. Münchow, S. Tassy, and A. Görlitz, *"Production of heteronuclear molecules in an electronically excited state by photoassociation in a mixture of ultracold Yb and Rb",* Phys. Rev. A **79**, 061403 (2009).

[24] A. Gorges, N.Bingham, M.DeAngelo, M.Hamilton,and J. Roberts, *"Light-assisted collisional loss in a* $^{85/87}$*Rb ultracold optical trap",* Phys. Rev. A **78**, 033420 (2008).

[25] S. Papp and C. Wiemann, *"Observation of heteronuclear Feshbach molecules from a* ^{85}*Rb-*^{87}*Rb gas",* Phys. Rev. Lett. **97**, 180404 (2006).

[26] I. Bloch, M. Greiner, O. Mandel, T. Hänsh, and T. Esslinger, *"Sympathetic cooling of ^{85}Rb and ^{87}Rb",* Phys. Rev. A **64**, 021402 (2001).

[27] I. Chan, B. Barrett, and A. Kumarakrishnan, *"Precise determination of atomic g-factor ratios from a dual isotope magneto optical trap",* Phys. Rev. A **84**, 032509 (2011).

[28] V. Valenzuela, S. Hamzeloui, M. Gutiérrez and E. Gomez, *"Multiple isotope magneto-optical trap from a single diode laser",* J. Opt. Soc. Am. B **30**, 1205, (2013).

[29] K. Koo, J. Sudbery, D. Segal, and R. Thompson, *"Doppler cooling of Ca^+ ions in a Penning trap,"* Phys. Rev. A **69**, 043402 (2004).

[30] E. Shuman, J. Barry, and D. DeMille, *"Laser cooling of a diatomic molecule",* Nature **467**, 820–823 (2010).

[31] M. Zhu, C. Oates, and J. Hall, *"Continuous high-flux monovelocity atomic beam based on a broadband laser-cooling technique",* Phys. Rev. Lett. **67**, 46–49 (1991).

[32] M. S. Hamilton, A. R. Gorges, and J. L. Roberts, *"Inter-isotope effects in optimal dual-isotope loading into a shallow optical trap,"* J. Phys. B **45**, 095302 (2012).

[33] J. Booth, J. Dongen, P. Lebel, B. Klappauf, and K. Madison, *"Dual-channel amplification in a single-mode diode laser for multi-isotope laser cooling",* J. Opt. Soc. Am. B **24**, 2914–2920 (2007).

[34] S. Crane, X. Zhao, W. Taylor, and D. Vieira, *"Trapping an isotopic mixture of fermionic ^{84}Rb and bosonic ^{87}Rb atoms,"* Phys. Rev. A **62**, 011402 (2000).

[35] W. Süptitz, G. Wokurka, F. Strauch, P. Kohns, and W. Ertmer, *"Simultaneous cooling and trapping of ^{85}Rb and ^{87}Rb in a magneto-optical trap",* Opt. Lett. **19**, 1571–1573 (1994).

[36] V. Gokhroo, G. Rajalakshmi, R. K. Easwaran, and C. S. Unnikrishnan, *"Sub-Doppler deep-cooled bosonic and fermionic isotopes of potassium in a compact 2D3D MOT set-up,"* J. Phys. B **44**, 115307 (2011).

[37] M. Prevedelli, F. Cataliotti, E. Cornell, J. Ensher, C. Fort, L. Ricci, G. Tino, and M. Inguscio, *"Trapping and cooling of potassium isotopes in a double-magneto-optical-trap apparatus",* Phys. Rev. A **59**, 886–888 (1999).

[38] T. Loftus, J. Bochinsky, and T. Mossberg, *"Simultaneous multi-isotope trapping of ytterbium,"* Phys. Rev. A **63**, 053401 (2001).

[39] R. Stas, J. McNamara, W. Hogervorst, and W. Vassen, *"Simultaneous magneto-optical trapping of a boson-fermion mixture of metastable helium atoms",* Phys. Rev. Lett. **93**, 053001 (2004).

[40] A. Truscott, K. Strecker, W. McAlexander, G. Partridge, and R. Hulet, *"Observation of Fermi pressure in a gas of trapped atoms,"* Science **291**, 2570–2572 (2001).

[41] M. Mewes, G. Ferrari, F. Schreck, A. Sinatra, and C. Salomon, *"Simultaneous magneto-optical trapping of two lithium isotopes",* Phys. Rev. A **61**, 011403 (1999).

[42] X. Xu, T. Loftus, J. Hall, A. Gallagher, and J. Ye, *"Cooling and trapping of atomic strontium",* J. Opt. Soc. Am. B **20**, 968–976 (2003).

[43] N. Poli, R. Drullinger, G. Ferrari, J. Léonard, F. Sorrentino, and G. Tino, *"Cooling and trapping of ultracold strontium isotopic mixtures",* Phys. Rev. A **71**, 061403 (2005).

[44] R. Chicireanu, A. Pouderous, R. Barbé, B. Laburthe-Tolra, E. Maréchal, L. Vernac, J. C. Keller, and O. Gorceix, *"Simultaneous magneto-optical trapping of bosonic and fermionic chromium atoms,"* Phys. Rev. A **73**, 053406 (2006).

[45] J. Goldwin, S. Papp, B. DeMarco, and D. Jin, *"Two-species magneto-optical trap with ^{40}K and ^{87}Rb,"* Phys. Rev. A **65**, 021402 (2002).

[46] J. Weiner, V. S. Bagnato, S. Zilio, and P. S. Julienne, *"Experiments and theory in cold and ultracold collisions",* Rev. Mod. Phys. **71**, 1–85 (1999).

[47] A. Deb, A. Rakonjac, and N. Kjærgaard, *"Versatile laser system for experiments with cold atomic gases",* J. Opt. Soc. Am. B **29**, 3109–3113 (2012).

[48] V. Valenzuela, L. Hernández, and E. Gomez, *"High power rapidly tunable system for laser cooling",* Rev. Sci. Instrum. **83**, 015111 (2012).

[49] V. Bolpasi and W. von Klitzing, *"Double-pass tapered amplifier diode laser with an output power of 1 W for an injection power of only 200 W,"* Rev. Sci. Instrum. **81**, 113108 (2010).

[50] S. Martinez, L. Hernández, D. Reyes, E. Gomez, M. Ivory, C. Davison, and S. Aubin, *"Fast, small, and low vibration mechanical laser shutters",* Rev. Sci. Instrum. **82**, 046102 (2011).

[51] B. E. A. Saleh and M. C. Teich (2007). *"Fundamental of photonics",* 2nd Edition, Wiley, Boston.

[52] $http://www.nobelprize.org/nobel_prizes/physics/laureates/1944/$.

[53] Marlan O. Scully and M. Suhail Zubairy (1997). *"Quantum Optics",* Cambridge University Press, Pag. 160-163.

[54] S. Hamzeloui, D. Martínez, V. Abediyeh, N. Arias, E. Gomez, and V. Valenzuela, *"Dual atomic interferometer with a tunable point of minimum magnetic sensitivity",* Phys. Rev. A. **to be published**, (2016).

[55] http://www.steck.us/alkalidata.

[56] E. Gomez, L. Orozco, A. P. Galvan, and G. Sprouse, *"Lifetime measurement of the 8 s level in francium",* Phys. Rev. A **71**, 062504 (2005).

[57] N. F. Ramsey , *"A Molecular Beam Resonance Method with Separated Oscillating Fields",* Phys. Rev **78**, 695 (1950).

[58] G. B. Arfken and H. J. Weber (1995). *"MATHEMATICAL METHODS FOR PHYSICISTS",* 4th Edition, Academic Press.

[59] G. Ferrari, M. Mewes, F. Schreck, and C. Salomon, *"High-power multiple-frequency narrow-linewidth laser source based on a semiconductor tapered amplifier",* Opt. Lett. **24**, 151–153 (1999).

[60] K. Moler, D. Weiss, M. Kasevich, and S. Chu, *"Theoretical analysis of velocity-selective Raman transitions",* Phys. Rev. A **45**, 342 (1992).

[61] S. Chu, L. Hollberg, J. E. Bjorkholm, A. Cable, and A. Ashkin, *"Three-dimensional viscous confinement and cooling of atoms by resonance radiation pressure,"* Phys. Rev. A **55**, 48 (1985).

[62] E. Hecht (2002). *"OPTICS",* 4th Edition, Addison Weley.

[63] M. Fox (2006). *"Quantum Optics: An Introduction",* 6th Edition, Oxford Master Series in Physics Pag.181.

[64] P. Cladé (2005). *"Bloch oscillation of ultracold atoms and measurement of the fine structure constant",* PhD Thesis, Pierre and Marie Curie University: France.

[65] Martínez Hernández, D. (2015). *"Interferometría de Ramsey en una transición de dos fotones en ^{87}Rb",* MCs. Thesis, Universidad Autónoma de San Luis Potosí: México.

[66] D. Sheng, S. Li, N. Dural, and M. Romalis, *"Subfemtotesla Scalar Atomic Magnetometry Using Multipass Cells",* Phys. Rev. Lett. **110**, 160802 (2013).

[67] C. Baker, D. Doyle, P. Geltenbort, K. Green, M. van der Griten, P. Harris, P. Iaydjiev, S. ivanov, D. May, J. Pendlebury, et al., *"Improved Experimental Limit on the Electric Dipole Moment of the Neutron",* Phys. Rev. Lett. **97**, 131801 (2006).

[68] H. Koch, G. Bison, Z. Grujić, W. Heil, M. Kasprzak, P. Knowles, A. Kraft, A. Pazgalev, A. Schnabel, J. Voigt, et al., *"Design and performance of an absolute ^{3}He/Cs magnetometer",* Eur. Phys. J. D. **69**, 202 (2015).

[69] J. Belfi, G. Bevilacqua, V. Biancalana, R. Cecchi, Y. Dancheva, and L. Moi, *"Stray magnetic field compensation with a scalar atomic magnetometer",* Rev. Sci. Instrum. **81**, 065103 (2010).

[70] S. Afach, G. Bison, K. Bodek, F. Burri, Z. Chowdhuri, M. Daum, M. Fertl, B. Franke, Z. Grujic, V. Hélaine, et al., *"Dynamic stabilization of the magnetic field surrounding the neutron electric dipole moment spectrometer at the Paul Scherrer Institute",* J. Appl. Phys. **116**, 084510 (2014).

[71] H. Xia, A. Baranga, D. Hoffman, and M. Romalis, *"Magnetoencephalography with an atomic magnetometer",* Appl. Phys. Lett. **89**, 211104 (2006).

[72] M Hämäläinen, R Hari, RJ Ilmoniemi, J Knuutila and O. Lounasmaa, *"Magnetoencephalography—theory, instrumentation, and applications to noninvasive studies of the working human brain",* Rev. Mod. Phys. **65**, 413 (1993).

[73] M. Schleier-Smith, I. Leroux, and V. Vuletić, *"States of an Ensemble of Two-Level Atoms with Reduced Quantum Uncertainty",* Phys. Rev. Lett. **104**, 073604 (2010).

[74] A. Kuzmich, L. Mandel, and N. Bigelow, *"Generation of Spin Squeezing via Continuous Quantum Nondemolition Measurement",* Phys. Rev. Lett. **85**, 1594 (2000).

[75] R. Sewell, M. Koschorreck, M. Napolitano, B. Dubost, N. Behbood, and M. Mitchell, *"Magnetic Sensitivity Beyond the Projection Noise Limit by Spin Squeezing",* Phys. Rev. Lett. **109**, 253605 (2012).

[76] M. Smiciklas, J. Brown, L. Cheuk, S. Smullin, and M. Romalis, *"New Test of Local Lorentz Invariance Using a ^{21}NeRbK Comagnetometer",* Phys. Rev. Lett. **107**, 171604 (2011).

[77] J. Baron, W. Campbell, D. DeMille, J. Doyle, G. Gabrielse, Y. Gurevich, P. Hess, N. Hutzler, E. Kirilov, I. Kozyryev, et al., *"Order of magnitude smaller limit on the electric dipole moment of the electron",* Science **343**, 269 (2014).

[78] P. Treutlein, T. Steinmetz, Y. Colombe, B. Lev, P. Hommelhoff, J. Reichel, M. Greiner, O. Mandel, A. Widera, T. Rom, et al., *"Quantum information processing in optical lattices and magnetic microtraps",* Fortschr. Phys. **54**, 702 (2006).

[79] J. Ringot, P. Szriftgiser, and J. Garreau, *"Subrecoil Raman spectroscopy of cold cesium atoms",* Phys. Rev. A. **65**, 013403 (2001).

[80] C. Dedman, R. Dall, L. Byron, and A. Truscott, *"Active cancellation of stray magnetic fields in a Bose-Einstein condensation experiment",* Rev. Sci. Instrum. **78**, 024703 (2007).

[81] C. Deutsch, F. Ramirez-Martinez, C. Lacroûte, F. Reinhard, T. Schneider, J. Fuchs, F. Piéchon, F. Laloë, J. Reichel, and P. Rosenbusch, *"Spin self-rephasing and very long coherence times in a trapped atomic ensemble",* Phys. Rev. Lett. **105**, 020401 (2010).

[82] N. Lundblad, M. Schlosser, and J. Porto, *"Experimental observation of magic-wavelength behavior of ^{87}Rb atoms in an optical lattice",* Phys. Rev. A. **81**, 031611 (2010).

[83] Y. Dudin, R. Zhao, T. Kennedy, and A. Kuzmich, *"Light storage in a magnetically dressed optical lattice",* Phys. Rev. Lett. **81**, 041805 (2010).

[84] A. Derevianko, *"Doubly Magic" Conditions in Magic-Wavelength Trapping of Ultracold Alkali-Metal Atoms",* Phys. Rev. Lett. **105**, 033002 (2010).

[85] M. Zhong, M. Hedges, R. Ahlefeldt, J. Bartholomew, S. Beavan, S. Wittig, J. Longdell, and M. Sellars, *"Optically addressable nuclear spins in a solid with a six-hour coherence time",* Nature **517**, 177 (2015).

[86] G. Heinze, C. Hubrich, and T. Halfmann, *"Stopped light and image storage by electromagnetically induced transparency up to the regime of one minute",* Phys. Rev. Lett. **111**, 033601 (2013).

[87] P. Harris, C. Baker, K. Green, P. Iaydjiev, S. Ivanov, D. May, J. Pendlebury, D. Shiers, K. Smith, M. van der Grinten, et al., *"New experimental limit on the electric dipole moment of the neutron",* Phys. Rev. Lett. **82**, 904 (1999).

[88] C. A. Baker, D. D. Doyle, P. Geltenbort, K. Green, M. G. D. van der Grinten, P. G. Harris, P. Iaydjiev, S. N. Ivanov, D. J. R. May, J. M. Pendlebury, J. D. Richardson, D. Shiers, and K. F. Smith, *"Improved Experimental Limit on the Electric Dipole Moment of the Neutron",* Phys. Rev. Lett. **97**, 131801 (2006).

[89] D. Sheng, L. Orozco, and E. Gomez, *"Preliminary studies for anapole moment measurements in rubidium and francium",* J. Phys. B: At. Mol. Opt. Phys. **43**, 074004 (2010).

[90] L. Sárkány, P. Weiss, H. Hattermann, and J. Fortágh, *"Controlling the magnetic-field sensitivity of atomic-clock states by microwave dressing,"* Phys. Rev. A **90**, 053416 (2014).

[91] F. Gerbier, A. Widera, S. Fölling, O. Mandel, and I. Bloch, *"Resonant control of spin dynamics in ultracold quantum gases by microwave dressing",* Phys. Rev. A. **73**, 041602 (2006).

[92] N. Timoney, I. Baumgart, M. Johanning, A. Varón, M. Plenio, A. Retzker, and C. Wunderlich, *"Quantum gates and memory using microwave-dressed states",* Nature **476**, 185 (2011).

[93] T. Zanon-Willette, E. de Clercq, and E. Arimondo, *"Magic radio-frequency dressing of nuclear spins in high-accuracy optical clocks",* Phys. Rev. Lett. **109** 223003, (2012).

[94] A. Bonnin, N. Zahzam, Y. Bidel, and A. Bresson, *"Simultaneous dual-species matter-wave accelerometer",* Phys. Rev. A. **88**, 043615 (2013).

[95] M. Meunier, I. Dutta, R. Geiger, C. Guerlin, C. Alzar, and A. Landragin, *"Stability enhancement by joint phase measurements in a single cold atomic fountain",* Phys. Rev. A. **90**, 063633 (2014).

[96] Z. Hu, X. Duan, M. Zhou, B. Sun, J. Zhao, M. Huang, and J. Luo, *"Simultaneous differential measurement of a magnetic-field gradient by atom interferometry using double fountains",* Phys. Rev. A. **84**, 013620 (2011).

[97] A. Wood, L. Bennie, A. Duong, M. Jasperse, L. Turner, and R. Anderson, *"Magnetic tensor gradiometry using Ramsey interferometry of spinor condensates",* Phys. Rev. A. **92**, 053604 (2015).

[98] G. Rosi, R. Sorrentino, L. Cacciapuoti, M. Prevedelli, and G. Tino, *"Precision measurement of the Newtonian gravitational constant using cold atoms",* Nature **510**, 518 (2014).

[99] P. D. Stern, *"The Atomic Nucleus and Bohr's Early Model of the Atom",* NASAGoddard Space Flight Center. (2005).

[100] E. L. Raab, M. Prentiss, Alex Cable, Steven Chu and D. E. Pritchard *"Trapping of Neutral Sodium Atoms with Radiation Pressure",* Phys. Rev. Lett. **59**, 2631–2634 (1987).

[101] H. F. Hess, G. P. Kochanski, J. M. Doyle, N. Masuhara, D. Kleppner and T. J. Greytak *"Magnetic trapping of spin-polarized atomic hydrogen",* Phys. Rev. Lett. **59**, 672 (1987).

[102] J. P. Burke, J. L. Bohn, B. D. Esry, and C. H. Greene , *"Impact of the ^{87}Rb singlet scattering length on suppressing inelastic collisions",* Phys. Rev. A **55**, R2511(R) (1997).

[103] C. Chuu, T. Strassel, B. Zhao, M. Koch, Y. Chen, S. Chen, Z. Yuan, J. Schmiedmayer, and J. Pan, *Quantum Memory with Optically Trapped Atoms",* Phys. Rev. Lett **101**, 120501 (2008).

[104] *"Bose-Einstein Condensation in a Gas of Sodium Atoms* Phys. Rev. Lett. **75**, 3969–3973 (1995).

[105] L.O. Castaños and E. Gomez, *"Model for a phase-space selector using microwave transitions",* Phys. Rev. A. **89**, 013406 (2014).

[106] S. Hamzeloui, N. Arias, V. Abediyeh, D. Martínez, M. Gutiérrez, E. Uruñuela, E. del Rio, E. Cerda-Méndez, E. Gomez, and V. Valenzuela, *"Toward precision measurement at UASLP",* J. Phys.: Conf. Ser. **698**, 012011 (2016).